Next Generation Ultrashort-Pulse Retrieval Algorithm for Frequency-Resolved Optical Gating: The Inclusion of Random (Noise) and Nonrandom (Spatio-Temporal Pulse Distortions) Error

A Dissertation
Presented to
The Academic Faculty

by

Ziyang Wang

In Partial Fulfillment
of the Requirements for the Degree
Doctor of Philosophy

School of Physics
Georgia Institute of Technology
May 2005

Next Generation Ultrashort-Pulse Retrieval Algorithm for Frequency-Resolved Optical Gating: The Inclusion of Random (Noise) and Nonrandom (Spatio-Temporal Pulse Distortions) Error

Approved by:

Dr. Rick Trebino, Advisor
School of Physics
Georgia Institute of Technology

Dr. Paul Kvam
School of Industrial & System Engineering
Georgia Institute of Technology

Dr. T.A.B. Kennedy
School of Physics
Georgia Institute of Technology

Dr. John Buck
School of Electrical & Computer Engineering
Georgia Institute of Technology

Dr. Li You
School of Physics
Georgia Institute of Technology

Date Approved: March 31, 2005

To my lovely wife, Zhi Li, without her love and support this work cannot be done.

ACKNOWLEDGEMENTS

No project is produced in a vacuum, this work is done with helps from many people. First of all, I would like to thanks my advisor, Dr. Rick Trebino. Without his wise guidance through my graduate research, it is no possible to get this work done. I would especially thank Dr. Paul Kvam, who greatly help me with the first part of the work in the thesis. I would also like to thank fellow graduate students and postdocs in the lab: Erik, Xun, Selcuk, Qiang, Xuan, Aparana, Pablo and rest of the group. Finally, special thanks to my wife, Zhi Li, for her constant supports and loves.

TABLE OF CONTENTS

LIST OF FIGURES

SUMMARY

The **f**requency-**r**esolved **o**ptical **g**ating (FROG) technique is an important ultrashort-pulse measurement technique, approaching its maturity after a decade of developments and innovations. A new variation of the FROG, called **gr**ating-**e**liminated **n**o-nonsense **o**bservation of **u**ltrafast **l**aser-**l**ight **e**-fields (GRENOUILLE), is known for its low cost, compact size, and user-friendly operation. As a 2003 R&D 100 award winner, GRENOUILLE has taken the FROG technique into the commercial realm. With the rapid improvement of the hardware, new capabilities are possible, but sophisticated software is required in order to achieve them. In this project, I have developed new pulse-retrieval software which automatically computes, for the first time, error bars on the retrieved pulse intensity and phase. I also included the effects of nonrandom errors—spatio-temporal pulse distortions—in the spectrograms measured by the FROG and GRENOUILLE techniques. These nonrandom errors, primarily introduced by the spatio-temporal pulse distortions, severely crippled previous algorithms, which ignored such effects. In order to retrieve the pulse in the presence of the nonrandom errors, a new ultrashort pulse field model, including both the spatial and temporal information of pulses, was proposed. A new GRENOUILLE trace-generation model based on this new pulse model was also developed. Finally a new algorithm was created. The core of the optimization method was upgraded from the steepest descent method to Newton's method. Numerical simulations indicate that this new algorithm can retrieve the temporal characteristics of pulse even when its FROG trace is contaminated with significant nonrandom errors in the form of spatio-temporal distortions—spatial chirps and pulse-front tilts. Furthermore, the values of these distortions can also be computed by the new algorithm. For random errors, no rigorous mathematical model can be constructed, so a statistical treatment was necessary. The implementation of a well known statistical method, the bootstrap method, proved ideal. By using the bootstrap method, we can now retrieve not only the pulse intensity and phase, but also error bars on these values from a

single FROG trace measurement in the presence of arbitrary random errors. The results show that the bootstrap method not only attains error bars from noisy FROG traces, but that it is also an excellent approach for detecting ambiguities in FROG pulse retrieval.

CHAPTER I

INTRODUCTION—FROG TECHNIQUE

1.1 Introduction

In the Ultrafast community, 'Ultrashort Laser Pulse' is the name used to describe a very short burst of electro-magnetic energy. The time durations of these bursts are usually in the order of femtoseconds. Because of their high instant intensities and short time durations, ultrashort laser pulses are widely used in the fields of physics, chemistry and biology. Accurate measurement of these ultrashort laser pulses is very important.

Measuring the pulses in femtoseconds is not easy because ultrashort pulses are the shortest events ever created by mankind. Normally a shorter event is required to measure the unknown event. Intensity autocorrelation was one of the first techniques used to solve this optical measurement problem. Intensity autocorrelation is based on an idea that an ultrashort laser pulse can be measured by itself. This same idea was implemented in the later, more advanced techniques, such as frequency-resolved optical gating(FROG).[53] Although autocorrelator originates from a revolutionary idea, it can only poorly measure the duration of the pulse and nothing else. More detailed information about pulses (intensity profile, phase profile) is required in advanced research. The techniques that can measure full intensity and phase characteristic of an ultrashort pulse were invented in the early 1990's. FROG and spectral phase interferometry for direct electric-field reconstruction(SPIDER) stand out as two most well-known and reliable techniques.

FROG capitalizes the idea of autocorrelator—measuring the pulse by itself. But unlike autocorrelator which measures the total energy of the gated piece of the pulse, FROG spectrally resolves the gated piece of the pulse. What FROG measured is a 2D spectrogram of the ultrashort pulse. This is what is referred to as FROG trace in the following description. FROG trace contains complete information about the intensity and phase of a complex pulse, except for a few trivial ambiguities that can be ignored in most ultrashort pulse

implementations. After encoding the pulse information in the FROG trace, a numerical program is used to retrieve the pulse information (intensity and phase) from the measured FROG trace. Retrieval of the pulse intensity and phase relies on an iterative algorithm. Because of the huge information redundancy in the FROG trace and the iterative nature of the algorithm, the pulse retrieval of the FROG technique is extremely robust.

After about ten years of development, the FROG technique is approaching its maturity. The appearance of the new version of FROG called grating-eliminated no-nonsense observation of ultrafast laser-light e-fields (GRENOUILLE) finally commercialized this technique. GRENOUILLE is known for its low cost, simple structure, compact size and alignment free operation. Also, recent research has shown that in addition to measuring temporal pulse characteristics, GRENOUILLE has the capacity of measuring spatial chirps and pulse-front tilts in an ultrashort pulse without a single modification in its hardware. As a result, the FROG pulse retrieval algorithm needed to be improved to cope with these new features in GRENOUILLE.

This chapter will cover the basics of the FROG technique from a perspective of a theorist, specifically focusing on the FROG apparatus, FROG trace and details of the FROG algorithm. Interested readers may refer to the FROG book authored by Dr. Rick Trebino.[53] Finally some new achievements in the FROG pulse retrieval algorithm will be addressed, which focus on determining the uncertainty in the retrieved pulse intensity and phase for all FROG pulse retrievals as well as retrieving spatial temporal parameters from distorted GRENOUILLE traces.

1.2 What the FROG Measures

FROG is the first technique to fully determine the intensity and phase of ultrashort pulses.

The apparatus of FROG is only an autocorrelator followed by a spectrometer, as shown in Fig. 1.

From this point of view, it is easy to ignore the significant difference between FROG and previous techniques. In the early techniques, such as spectrometer, autocorrelator, the ultrashort laser pulse is measured purely in the frequency domain (spectrometer), or in the

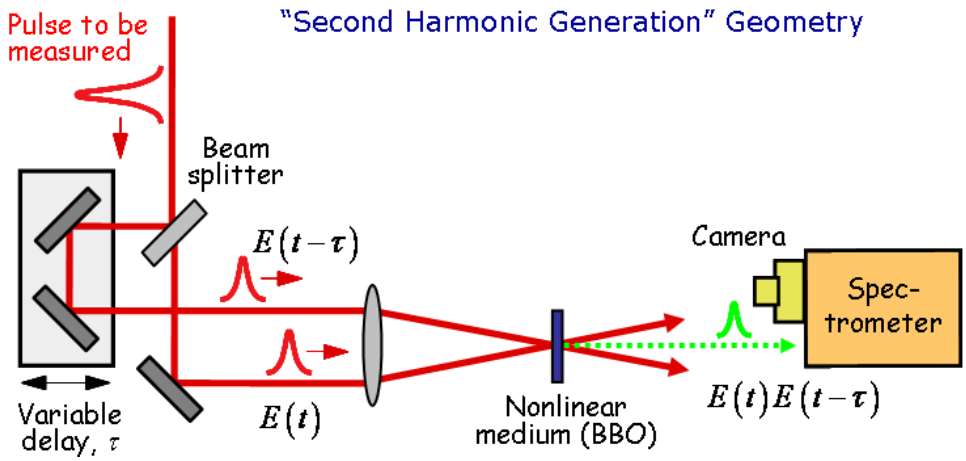

Figure 1: Apparatus of SHG FROG

time domain (autocorrelator). In all these measurements, detectors can only measure the intensity of the signal. As a result, it is inevitable to lose the phase information, if the measurement is taken only in one domain. The measurement of FROG trace is taken in a hybrid domain: *time-frequency domain*. This intermediate domain measurement gives FROG trace abundant information about the pulse intensity and phase. As time and frequency are two reciprocal domains connected by Fourier transform, phase information in time domain is encoded in intensity in frequency domain, and vise versa. So FROG trace obtains information of both intensity and phase of ultrashort laser pulse by doing only intensity measurement in time-frequency domain.

The mathematically rigorous view of FROG trace is spectrogram.$\Sigma_g^E(\omega,\tau)$ [4]:

$$\Sigma_g^E(\omega,\tau) \equiv \left| \int_{-\infty}^{-\infty} E(t) g(t-\tau) \exp(-i\omega t)\, dt \right|^2 \tag{1}$$

Where $g(t-\tau)$ is a variable delay gate function. In FROG trace, $g(t-\tau)$ is determined by the nonlinear-optical process chosen by different implementations. For example, it could be $E(t-\tau)$ in SHG FROG, $E^2(t-\tau)$ in THG FROG, $|E(t-\tau)|^2$ in polarization-gate FROG, etc.

In brief, what FROG measured is the spectrogram of the ultrashort laser pulse, in which the information of the pulse intensity and phase is encoded.

1.3 Why the FROG Trace Contains Complete Information of Ultrashort Pulse

As discussed in previous sections, FROG traces are measured in a hybrid time-frequency domain. Therefore FROG traces contain information of both intensities and phases of ultrashort pulses. But there are still two questions need be asked. First, is the information contained in FROG trace COMPLETE to determine the ultrashort pulse field? Second, can FROG trace UNIQUELY determine the pulse field? In this section, these questions will be answered.

To prove that FROG trace contains complete information of the ultrashort pulse, the mathematical form of the FROG trace need to be revisited. SHG FROG trace is used as an example to discuss the problem. For SHG FROG trace, $I_{FROG}^{SHG}(\omega,\tau)$

$$I_{FROG}^{SHG}(\omega,\tau)=\left|\int_{-\infty}^{-\infty}E(t)E(t-\tau)\exp(-i\omega t)\,dt\right|^2 \tag{2}$$

Eq. 2 can be rewritten as

$$I_{FROG}^{SHG}(\omega,\tau)=\left|\int_{-\infty}^{-\infty}E_{sig}(t,\Omega)\exp\left(-i(\omega t-\Omega\tau)\right)\,dt\,d\Omega\right|^2 \tag{3}$$

where

$$E_{sig}(t,\Omega)=\int_{-\infty}^{-\infty}E(t)E(t-\tau)\exp(-i\Omega\tau)\,d\tau \tag{4}$$

Eq. 3 shows that $I_{FROG}^{SHG}(\omega,\tau)$ is the intensity of 2D Fourier transform of field $E_{sig}(t,\Omega)$. Retrieving the field $E_{sig}(t,\Omega)$(intensity and phase) from measured $I_{FROG}^{SHG}(\omega,\tau)$ is the well known two-dimensional phase-retrieval problem which is solved in image recovery community. [51, 21, 48, 43, 20, 24, 22, 23] Henry Stark wrote an excellent book on this subject, *Image Recovery.*[51] Once $E_{sig}(t,\Omega)$ is retrieved from $I_{FROG}^{SHG}(\omega,\tau)$, to find out $E(t)$ is a trivial effort. Simply by inverse Fourier transforming $E_{sig}(t,\Omega)$ respect to Ω, the field $E(t)E(t-\tau)$ is provided. Then by substituting $\tau=t$, we can get $E\left(t\right)E\left(t-\tau\right)|_{t=\tau}=E\left(t\right)E\left(0\right)$. Since $E(0)$ just a constant, $E(t)E(0)$ is the desired pulse filed. Therefore the FROG trace does contain all the information needed to retrieve the ultrashort pulse field.

The question remaining is: Can the FROG trace UNIQUELY determine the pulse field? The answer came from the *Fundamental Theorem of Algebra*. Let's start from the two-dimensional discrete Fourier transform:

$$F_{k,h} = \sum_{m,n=1}^{N} f_{m,n} e^{-2\pi i(mk+nh)/N} \tag{5}$$

Or

$$F_{k,h} = \sum_{m,n=1}^{N} f_{m,n} z^m y^n \tag{6}$$

Where $y = e^{-2\pi ih/N}$ and $y = e^{-2\pi ik/N}$.

Eq. 3 can be written in its discrete form as,

$$I_{FROG}^{SHG}(\omega_k, \tau_h) = \left| \sum_{m,n=1}^{N} E_{sig}(t_m, \Omega_n) z^m y^n \right|^2 \tag{7}$$

So the uniqueness of the solutions is turned into a question: Can multiple sets of $E_{sig}(t_m, \Omega_n)$ give the same set of $I_{FROG}^{SHG}(\omega_k, \tau_h)$? The answer is NO in most cases. Because the Fundamental Theorem of Algebra fails for polynomials of two variables, the polynomial $\sum_{m,n=1}^{N} E_{sig}(t_m, \Omega_n) z^m y^n$ can't be factored in most cases. As a result, the solution of $E_{sig}(t_m, \Omega_n)$, thereafter the $E(t)$, is unique in a common case.

Occasionally the polynomial of two variables can be factored, then the ambiguity of solution is resulted. But as N increases, such cases become increasingly rare. The ambiguity in FROG pulse retrieval will be discussed in details in Chapter 3.

1.4 The FROG Algorithm

As shown in last section, FROG trace contains complete information of the ultrashort pulses, and can uniquely determine the pulse field. But how exactly is the pulse field retrieved from the measured trace? What is the algorithm used to do the retrieval? What is concerned in algorithm design? All these questions will be discussed in this section.

1.4.1 Algorithm Design

The task of FROG algorithm is to retrieve the complex electric field $E(t)$ from the measured FROG trace $I_{FROG}(\omega, \tau)$.

The specific mathematical form of $I_{FROG}(\omega, \tau)$ can be different depending on the type of the nonlinear optical process chosen in the experiment. But every one of them has a similar structure. The SHG FROG trace will be used to continue the discussion without losing generality. The other reason to choose the SHG FROG trace is that the SHG is the most popular non-linear optical interaction employed in the current FROG pulse measurement, and it is the non-linear process used by the commercial FROG device, GRENOUILLE. SHG FROG trace $I^{SHG}_{FROG}(\omega, \tau)$:

$$I^{SHG}_{FROG}(\omega, \tau) = \left| \int_{-\infty}^{-\infty} E(t)E(t-\tau)\exp(-i\omega t)\, dt \right|^2 \tag{8}$$

Eq. 8 reveals a very complicated relation between the pulse field, $E(t)$, and the FROG trace $I^{SHG}_{FROG}(\omega, \tau)$. The relation involves a Fourier transform integral and a magnitude squaring operation, which is irreversible. As a result, there is no direct inverse algorithm to calculate $E(t)$ from I^{SHG}_{FROG}. There is just a one way calculation from $E(t)$ to I^{SHG}_{FROG}. This fact implies that the algorithm for FROG pulse retrieval is essentially an iterative algorithm.

For an iterative algorithm, the algorithm starts from an initial guess of the solution, then the guessed solution is improved in every iteration, finally when the uncertainty in the guessed solution is smaller than certain predefined condition, the algorithm will claim to reach the final solution. So there are three important factors in an iterative algorithm: initial guess, iteratively improvement of the guessed solution, predefined termination condition.

In case of FROG algorithm, a random guess is used as the initial guess of the ultrashort pulse field. For the termination condition, the FROG error in the k-th iteration is defined as:

$$G^{(k)} = \sqrt{\frac{1}{N^2} \sum_{i,j=1}^{N} \left| I_{FROG}(\omega_i, \tau_j) - I^{(k)}_{FROG}(\omega_i, \tau_j) \right|^2} \tag{9}$$

Where $I^{(k)}_{FROG}(\omega_i, \tau_j)$ is the FROG trace calculated from k-th iteration's pulse field $E^{(k)}(t)$. In case of SHG FROG $I^{(k)}_{FROG}(\omega, \tau)$ is:

$$I^{(k)}_{FROG}(\omega, \tau) = \left| \int_{-\infty}^{-\infty} E^{(k)}(t) E^{(k)}(t-\tau) \exp(-i\omega t)\, dt \right|^2 \tag{10}$$

So basically $G^{(k)}$ defines the normalized difference between measured FROG trace I_{FROG} and calculated FROG trace $I^{(k)}_{FROG}$. In practice, a constant G_0 is chosen empirically, when $G^{(k)} < G_0$the algorithm will be terminated.

How to improve the guessed pulse field in each iteration of FROG algorithm still has a big space of choice. The goal of FROG algorithm is to find a $E^{(k)}(t)$ which minimizes the value of $G^{(k)}$. Therefore it can choose to directly minimize on the $G^{(k)}$, the objective function of minimization for this approach is $G\left(E(t)\right)$:

$$G\left(E(t)\right) = \sqrt{\frac{1}{N^2} \sum_{i,j=1}^{N} \left| I_{FROG}(\omega_i, \tau_j) - \left| \int_{-\infty}^{-\infty} E^{(k)}(t) E^{(k)}(t-\tau) \exp(-i\omega t)\, dt \right|^2 \right|^2} \tag{11}$$

The speed of an iteration program is directly related to the complexity of the objective function, the evaluation time of the objective function and the calculation time of the derivatives(if available). Eq. 11 shows two level integral in the objective function, which indicates a slow and most probably bad converged iteration program of it.

On the other hand, instead of doing minimization directly in the hybrid time-frequency domain it can be minimized in the time domain(or frequency domain, as shown latter). In this case, the objective function of minimization is,

$$Z = \sum_{i,j=1}^{N} \left| E\left(t_i\right) E\left(t_i - \tau_j\right) - E'_{sig}\left(t_i, \tau_j\right) \right|^2 \tag{12}$$

This approach is based on the iterative-Fourier-transform algorithm, which is commonly used in phase retrieval.[4, 15, 16, 45] In this case, the objective function is much simpler. The only cost is a one dimensional Fourier transforming between the time and the hybrid domain. Details about the iterative-Fourier-transform algorithm will be stated in next part.

In this part, with a close examination on the mathematical form of FROG trace, we

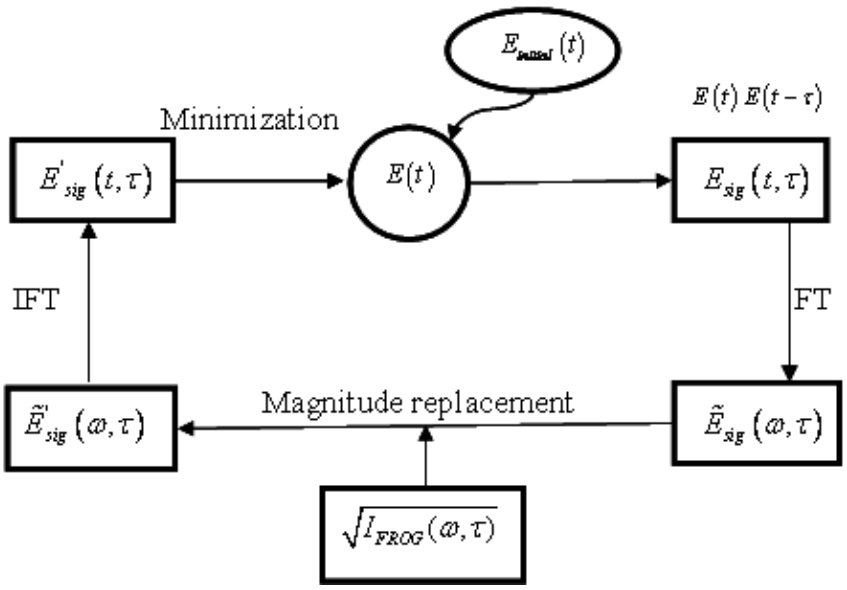

Figure 2: Schematic of a generic FROG algorithm

conclude that an iterative algorithm is required to conduct the pulse field retrieval and the minimization of algorithm need to be done on the time domain(or frequency domain).

1.4.2 The Iterative-Fourier-Transform Algorithm—Generalized projection

Following the conclusions drawn in the last part, a generic FROG algorithm is designed as shown in Fig. 2. It works in this way:

Step 1, Starting with an initial guessed field $E_{initial}(t)$, random guess is used in our program.

Step 2, Calculating the nonlinear signal field, $E_{sig}(t,\tau)$, in case of SHG is $E(t)E(t-\tau)$

Step 3, Fourier transforming $E_{sig}(t,\tau)$ respect to t, to get the signal field in frequency domain, $\widetilde{E}_{sig}(\omega,\tau)$

Step 4, Replacing the amplitude of $\widetilde{E}_{sig}(\omega,\tau)$ by the square root of the measured FROG trace, $I_{FROG}(\omega,\tau)$, to get an improved $\widetilde{E'}_{sig}(\omega,\tau)$,

Step 5, Inverse Fourier transforming $\widetilde{E'}_{sig}(\omega,\tau)$ back to time domain,$E'_{sig}(t,\tau)$

Step 6, Minimizing on $E'_{sig}(t,\tau)$ to find out a better guess of $E(t)$ for next iteration.

Step 7, Calculating the termination condition, if the condition is satisfied, algorithm returned, else go back to step 2 and continue.

In the iteration loop, two constraints are applied in the FROG pulse retrieval algorithm.

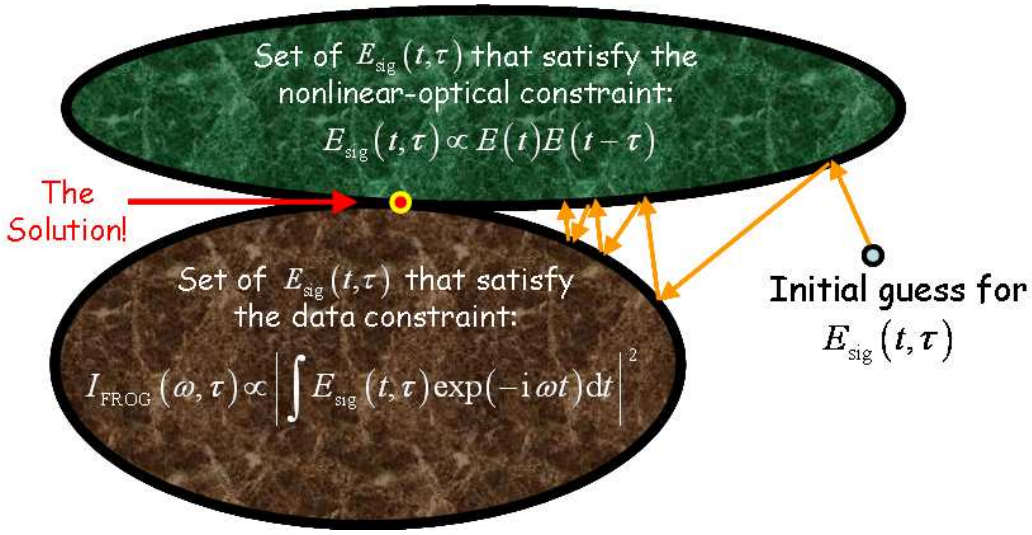

Figure 3: Solution space view of generalized projection.

The first constraint is the *data constraint*. This constraint indicates that the squared magnitude of $\widetilde{E'}_{sig}(\omega,\tau)$ should be equal to the measured FROG trace $I_{FROG}(\omega,\tau)$. This constraint is enforced with the magnitude replacement in step 4. The second constraint is the *mathematical-form constraint* or *nonlinear constraint*. This constraint requires the desired pulse field must obey the mathematical form with the nonlinear signal field, such as $E(t)E(t-\tau)$ in the SHG FROG. The mathematical form constraint is applied when doing minimization in step 6. To clearly understand the two constraints scheme in the FROG algorithm, the concept of generalized projection will be introduced. The idea of generalized projection is shown in Fig 3.

The lower elliptical region represents all the signal fields satisfying the data constraint. The upper elliptical region indicates set of signal fields satisfying the mathematical-form constraint. The overlapping point of two regions is the pulse field satisfying both constraints, therefore the solution pulse field we are looking for. In the FROG algorithm, two constraints are applied to the target field alternatively. Therefore the guessed solution is projected between two constraint sets back and forth while approaching the real solution. The technique is so-called generalized projection.

In practice, the generalized projection algorithm works very efficiently in FROG pulse retrieval. But in the work done in this thesis you will find cases, in which generalized

projection cannot be applied or cannot be directly applied to the FROG pulse retrieval.

1.4.3 Multidimensional Minimization in FROG

On step 6 of the FROG algorithm, the minimization on $E'_{sig}(t,\tau)$ is conducted to find out $E(t)$ for next iteration. This is the step in which the solution is actually improved in very iteration, so it is the most important step in algorithm. It turns out to be the hardest step too. Therefore the following section will discuss this step in detail.

Step 6 is a multidimensional minimization procedure. The objective function of minimization is,

$$Z = \sum_{i,j=1}^{N} \left| E\left(t_i\right) E\left(t_i - \tau_j\right) - E'_{sig}\left(t_i, \tau_j\right) \right|^2 \tag{13}$$

where $E'_{sig}\left(t_i, \tau_j\right)$ is the improved field generated in step 5.

In the function Z, every component of pulse field $E(t)$, $E(t_i)$, contains two independent variables, $\mathrm{Re}\left\{E\left(t_i\right)\right\}$, $\mathrm{Im}\left\{E\left(t_i\right)\right\}$. So it is a multidimensional minimization problem in complex space with 2N variables.

As discussed in Appendix A, there are two important factors in the unconstrained multidimensional minimization. The first is the minimization direction in the multidimensional space. The second is a one dimensional minimization procedure along the chosen direction.

In current FROG algorithm, Steepest descent method is used to determine the direction in every stage of the minimization. So the negative gradient of Z is calculated as the minimization direction.

$$\vec{g} = \frac{\partial Z}{\partial E\left(t\right)} \tag{14}$$

by component, $g(t_k)$ is,

$$\begin{aligned} &\mathrm{Re}\left\{g\left(t_k\right)\right\} = \tfrac{\partial Z}{\partial \mathrm{Re}\{E(t_k)\}} \\ &= 2\mathrm{Re}\left\{ \sum_{j=1}^{N} \begin{array}{l} E^*\left(t_k\right)\left|E\left(t_k - \tau_j\right)\right|^2 - E^*_{sig}\left(t_k, \tau_j\right) E\left(t_k - \tau_j\right) + \\ E^*\left(t_k\right)\left|E\left(t_k + \tau_j\right)\right|^2 - E^*_{sig}\left(t_k + \tau_j, \tau_j\right) E\left(t_k + \tau_j\right) \end{array} \right\} \end{aligned} \tag{15}$$

$$\begin{aligned}
&\mathrm{Im}\left\{g\left(t_k\right)\right\} = \frac{\partial Z}{\partial \mathrm{Im}\{E(t_k)\}} \\
&= -2\mathrm{Im}\left\{ \begin{array}{ll} \sum\limits_{j=1}^{N} & E^*\left(t_k\right)\left|E\left(t_k-\tau_j\right)\right|^2 - E^*_{sig}\left(t_k,\tau_j\right)E\left(t_k-\tau_j\right) + \\ & E^*\left(t_k\right)\left|E\left(t_k+\tau_j\right)\right|^2 - E^*_{sig}\left(t_k+\tau_j,\tau_j\right)E\left(t_k+\tau_j\right) \end{array} \right\}
\end{aligned} \tag{16}$$

So the $g(t_k)$ can be written as,

$$g\left(t_k\right) = \frac{2\partial Z}{\partial E^*\left(t_k\right)} \tag{17}$$

For the one dimensional minimization on the chosen direction, the objective function, Z, has very good property. Along any minimization direction, objective function Z is a polynomial. For example, Z is a polynomial of degree four in SHG FROG, or a polynomial of degree six in PG FROG. Suppose start from a random place in solution space, E_{in}, and move towards a random direction dE with a step length of λ. Then the new E field can be written as,

$$E(t) = E_{in}(t) + \lambda dE(t) \tag{18}$$

where

λ is the step length along the direction dE

By substituting Eq. 18 into Eq.13,

$$Z = \sum_{i,j=1}^{N} \left| \left[E_{in}\left(t_i\right) + \lambda dE\left(t_i\right)\right]\left[E_{in}\left(t_i-\tau_j\right) + \lambda dE\left(t_i-\tau_j\right)\right] - E'_{sig}\left(t_i,\tau_j\right)\right|^2 \tag{19}$$

Eq. 19 can be expanded into a polynomial of λ,

$$Z = C_0 + C_1\lambda + C_2\lambda^2 + C_3\lambda^3 + C_4\lambda^4 \tag{20}$$

where

$$C_0 = \sum_{i,j=1}^{N} \left| E_{in}\left(t_i\right)E_{in}\left(t_i-\tau_j\right) - E'_{sig}\left(t_i,\tau_j\right)\right|^2$$

$$C_1 = \sum_{i,j=1}^{N} 2\mathrm{Re}\left\{ \begin{array}{l} \left[E_{in}\left(t_i\right)E_{in}\left(t_i-\tau_j\right) - E'_{sig}\left(t_i,\tau_j\right)\right]^* \\ \times\left[dE\left(t_i\right)E_{in}\left(t_i-\tau_j\right) + E_{in}\left(t_i\right)dE\left(t_i-\tau_j\right)\right] \end{array} \right\}$$

$$C_2 = \sum_{i,j=1}^{N} \begin{array}{l} \left|dE\left(t_i\right)E_{in}\left(t_i-\tau_j\right) + E_{in}\left(t_i\right)dE\left(t_i-\tau_j\right)\right|^2 + \\ 2\mathrm{Re}\left\{\left[E_{in}\left(t_i\right)E_{in}\left(t_i-\tau_j\right) - E'_{sig}\left(t_i,\tau_j\right)\right]^* dE\left(t_i\right)dE\left(t_i-\tau_j\right)\right\} \end{array}$$

$$C_3 = \sum_{i,j=1}^{N} 2\mathrm{Re}\left\{\left[dE\left(t_i\right) E_{in}\left(t_i - \tau_j\right) + E_{in}\left(t_i\right) dE\left(t_i - \tau_j\right)\right]\left[dE\left(t_i\right) dE\left(t_i - \tau_j\right)\right]^*\right\}$$

$$C_4 = \sum_{i,j=1}^{N} \left|dE\left(t_i\right) dE\left(t_i - \tau_j\right)\right|^2$$

As discussed in appendix A, the global minimum can be calculated directly in the one dimensional minimization of a polynomial. In SHG FROG, the Z function is defined by polynomial $\vec{C} = \{C_0, C_1, C_2, C_3, C_4\}$ along any minimizing direction. The first order derivative of it is defined by polynomial $\vec{C}' = \{C_1, 2C_2, 3C_3, 4C_4\}$. Then the root of $\vec{C}'$, $X = \{x_1, x_2, x_3\}$, can be calculated. Finally the real root with the minimum evaluation of polynomial $\vec{C}$ is the desired solution.

In summary, FROG algorithm chose the gradient of the objective function as the minimization direction and used one dimensional polynomial minimization as the line minimization procedure.

1.5 Next Generation of the FROG Algorithm

Although FROG technique is highly developed, there are still problems remained to be solved. Such as, how accurate the FROG pulse measurement is, or what is the uncertainty of the retrieved pulse field? This question is concerned by researchers using the technique. The answer is unknown until the publication of the work in this thesis. Also, as discussed in section 1.3, ambiguity is possible in the FROG pulse retrieval, whether the ambiguity of the solution could be detected by FROG algorithm is a interesting problem to be solved.

On the other hand, the new variation of FROG, GRENOUILLE, is capable of measuring spatio-temporal distortions in the ultrashort pulses. FROG algorithm should also be developed to cope with these new features of technique.

In this work, several new aspects of FROG algorithm will be explored. Development of the algorithm includes not only solving the remaining problems in the FROG technique, but also modifications for new features in GRENOUILLE.

Chapter 2 will discuss how to implement a statistic method—bootstrap, in the FROG pulse retrieval to determine the uncertainty in the FROG pulse measurement.[56]

In chapter 3, 'bootstrap' method is revisited, the extension of the algorithm includes how bootstrap method is capable of finding new ambiguities (if they exist). [55]

In chapter 4, FROG algorithm is modified in the core part to retrieve both the temporal field and the spatio-temporal parameters from the distorted GRENOUILLE trace.

In chapter 5, a practical model for removing the spatial profile influence of the input beam on the GRENOUILLE trace is proposed.

CHAPTER II

ERROR BARS IN FROG

This chapter originally appeared as a paper by the author:

Ziyang Wang, Erik Zeek, Rick Trebino and Paul Kvam, "Determining error bars in measurements of ultrashort laser pulses", *JOSA B* vol. 20, no. 11, pp. 2400-2405, 2003.

2.1 Introduction

The results from the mathematical calculations can be clearly separated into two groups, the 'correct' results and the 'wrong' results. But for the results from the physical measurements, the border line between the 'correct' and 'wrong' is usually blurred. All the results from physical measurements come with uncertainty. When uncertainty is 'small', then the results can be considered as accurate or 'correct'. Oppositely, the results will be judged as 'wrong'. So determining the uncertainty of the measurement is as important as the measurement itself. A measurement without determined uncertainty just like a person without legal identification, which is unacceptable in the scientific world.

Determining the uncertainty in the measurement of an ultrashort laser pulse is a long concerned but unsolved problem.

Back to the date, when autocorrelation was the only available method of measuring an ultrashort pulse, the uncertainty is inherently undeterminable. Because an autocorrelation trace is essentially lack of information to completely determine the pulse field, even only the intensity part. One autocorrelation trace typically corresponds to many different intensities of pulses, and gives no information of the phase. Even when an autocorrelation trace is combined with a spectrum, one measurement still corresponds to many different intensities and phases.[13] With such kind of *internal* uncertainty, even a flawless autocorrelation trace will generate unpredictable uncertainty in measured pulse field. Therefore it makes no sense to attempt to place error bars on the pulse field measured by the autocorrelation technique.

Fortunately, now techniques can essentially uniquely determine the intensity and phase of the ultrashort pulse fields, therefore without the internal uncertainty as mentioned above.

FROG, as discussed in chapter 1, is one of most commonly used methods to measure the ultrashort pulse filed. FROG can retrieve the complete pulse intensity and phase without any assumptions about the pulse. Furthermore, FROG technique makes great improvement on device and capabilities. FROG's cousin XFROG is now being used to measure extremely complex pulses such as ultrabroadband continuum originating from a microstructured fiber, which can have a time-bandwidth product in excess of 1000. [29, 18] A new version of FROG, GRENOUILLE, has extremely simple beam geometries that make it simplest pulse-measurement technique available. GENOUILLE is also capable to measure the spatial temporal distortions in ultrashort pulses. In addition, GENOUILLE is proved to be the most sensitive device in measuring pulse front tilt.[2] On the other hand, with new nonlinearities, FROG is able to measure ultraweak pulses with <100 photons each.[58]

Since FROG technique plays such an important role in the ultrashort pulse measurement and is so widely used, it is more crucial to determine the uncertainty in the FROG measurement to make the technique 'legal'. Actually, FROG does have some indication of the accuracy of the measured pulses. "FROG error", the rms difference between the measured and retrieved FROG traces, is defined for this purpose. However, FROG error only indicates the mismatching between the measured and retrieved FROG traces, which tell us little about error in the intensity and phase of the pulse field on each of the retrieved points. Even worse, its indication of the measurement error depends on the trace size, so FROG errors from different measurements are incomparable to each other. On the other hand, singular value decomposition can detect systematic error in the FROG measurement, but it can only give an *indirect* estimation of the uncertainty. [34]

To give FROG technique a full 'certification', a method is required for determining *the uncertainty in each of the retrieved intensity and phase points, that is, error bars.*

Unfortunately, it is almost impossible to get error bars of FROG measurement in a common manner. To compute error bars using regular error analysis method, first need to identify all the known sources of errors, then need to track all the error sources down to the

final result to determine the uncertainty. But in case of FROG technique, to identify all the sources of errors will be a tedious task. In addition, because an iterative algorithm is used to retrieve the pulse field, it is impossible to propagate the error in the sources to the final result. As a result, error bars are often not reported in measurements and are never reported in pulse measurements. In this work, a simple, robust, and general technique is presented for placing error bars on the intensity and phase retrieved in a FROG measurement. It operates automatically, requiring no extra measurements or analysis, instead operating with only a single measured trace.

Another issue in the measurement of ultrashort pulses (and measurements of phase, in general) is when intensity goes to zero, the phase will become meaningless. This is obvious in theory, but it causes a practical problem: At what point should the phase be stopped plotting? Omitting phase points for which the intensity is below some threshold is often called "phase-blanking." Usually, it need decide the threshold for phase-blanking, the decision is often made based on aesthetics rather than science.

Here an automated method makes this decision objectively and appropriately. Once error bars are determined, the problem of phase-blanking is quite simple: when the phase error exceeds or equals 2π , then the phase is clearly undetermined, and phase-blanking is appropriate. Note that, once the technique for the determination of error bars is automated, the phase-blanking is also. Moreover, it requires no arbitrary judgments on the part of the user.

2.2 The Bootstrap Method

The technique that solves both of these problems is the "bootstrap" method, a well-established statistical method.[49, 19, 17]

2.2.1 Overview of the Bootstrap Method

First appearance of Bootstrap method is in the publication of Bradley Efron's article in 1979. It turned out to be a major event in Statistics. The method synthesized the earlier resampling ideas and established a new framework for simulation-based statistical analysis.

The bootstrap method is a computer-based method of statistical inference that can answer many real statistical questions without formulas. In bootstrap method, computer simulations replaced complicated and often inaccurate approximations to biases, variances, and other measures of uncertainty. This feature attracted theoreticians and researchers. The method has been widely used in many fields, such as: curve fitting, permutation tests, regression analysis,etc. Mass of empirical evidence shows that the bootstrap method often works better than traditional methods. [26, 27, 30, 28]

In this work, another implementation of bootstrap method in the scientific research is presented: the implementation of bootstrap method in the FROG pulse retrieval.

2.2.2 How the Bootstrap Works

Here, as users of the statistical method, we will not give a rigorous theoretical treatment of the bootstrap method. The discussion will concentrate on the ideas rather than their mathematical justification.

Bootstrap method works in following way. Suppose there is a set of data from experiment, $X = (x_1, x_2, \cdots, x_n)$, from which curtain parameter $s(X)$ is determined. $s(X)$ could be anything interested by the researchers, such as the mean value of the data set, the curve which can be fitted out from the data set, etc. Bootstrap method can find out the standard error of the $s(X)$. Bootstrap process is shown in figure 4.[19]

First step of the process is generating M (M usually be a very large number) independent *bootstrap samples* $X^{*1}, X^{*2}, \cdots, X^{*M}$. Each bootstrap sample $X^{*m} = (x_1^*, x_2^*, \cdots, x_n^*)$, is generated by randomly sampling with replacement n times from the original data set $X = (x_1, x_2, \cdots, x_n)$,(resulting in some points possibly occurring more than once and others not at all). Then from each bootstrap sample, calculate a *bootstrap replication* of $s(X)$, denoted by $s(X^{*m})$. $s(X^{*m})$ is calculated in the same way as calculate the $s(X)$ from original data set X. Finally the bootstrap estimation of standard error is the standard deviation of the bootstrap replications.[19]

$$\widehat{se}_{boot} = \left\{ \sum_{m=1}^{M} \left[s\left(X^{*m}\right) - \overline{s} \right]^2 / (M-1) \right\}^{\frac{1}{2}} \tag{21}$$

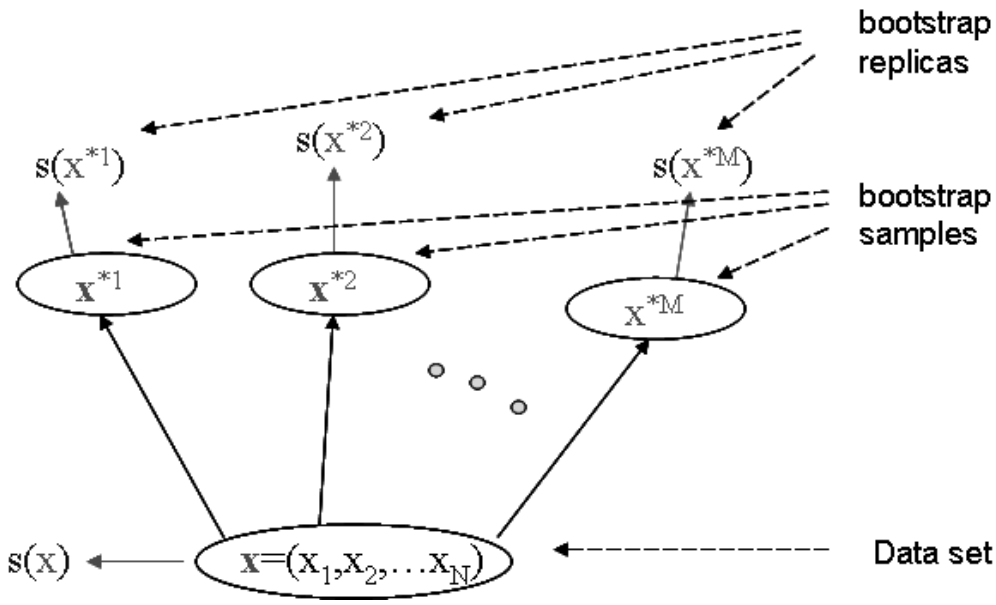

Figure 4: Schematic of the bootstrap process for estimating the standard error of a statistic $s(X)$

where

$\overline{s} = \sum_{m=1}^{M} s\left(X^{*m}\right)/M.$

Yes, that is how simple the bootstrap method works. As shown in the process described above, the basic idea of bootstrap method is: the method treats the computer simulations, bootstrap samples, just like the data obtained from experiments, then finds out the standard error in the same way as in multiple experiments. The reason behinds it is: the empirical distribution of a big data set,X, is very close to its real or theoretical distribution(it is statistically true when you have a huge independent and identically distributed data set). So sampling with replacement from the original data set X, is statistically equivalent to reproducing the data from experiments.

So bootstrap method works in a simple manner and only requirement to apply the method is *a huge independent and identically distributed data set(iid).*[49]

2.3 Implementation of the Bootstrap Method in FROG Pulse Retrievals

In this section, first the validity of the implementation of bootstrap method will be discussed in the FROG pulse retrieval, followed by the details about how exactly the method is applied to pulse retrieval algorithm. Finally some subtleties in the implementation will be mentioned.

2.3.1 Validity

As discussed in last section, the only requirement for the bootstrap method to work is to have *a huge independent and identically distributed data set.* In practice, bootstrap method are used in many fancy ways, in which the condition above is not always hold.[17] But this research still legitimately check the condition for integrity of the work. In case of FROG technique, what is measured is a N by N FROG trace, the parameters we want to determine from it is the pulse field, which have 2N variables(considering both the real and the imaginary parts of it). So one FROG trace can be treated as huge data set for the pulse field. On the other hand, the final goal of FROG algorithm is to minimize the FROG error,$G\left(E(t)\right)$:

$$G\left(E(t)\right) = \sqrt{\frac{1}{N^2}\sum_{i,j=1}^{N}\left|I_{FROG}(\omega_i,\tau_j) - \left|\int_{-\infty}^{-\infty} E(t)E(t-\tau)\exp(-i\omega t)\,dt\right|^2\right|^2} \tag{22}$$

This minimization is a *least square problem.* In least square problem, every point is equally treated.

So one FROG trace can be considered as *a huge independent and identically distributed data set.* Therefore it is valid to apply bootstrap method in the FROG pulse retrieval algorithm.

2.3.2 Implementation & Details

Applying this approach to ultrashort-pulse measurement simply involves running the FROG retrieval algorithm on the order of 10 to 100 times on the measured FROG trace, but each time with only a subset of points, chosen at random as described above, and tabulating the

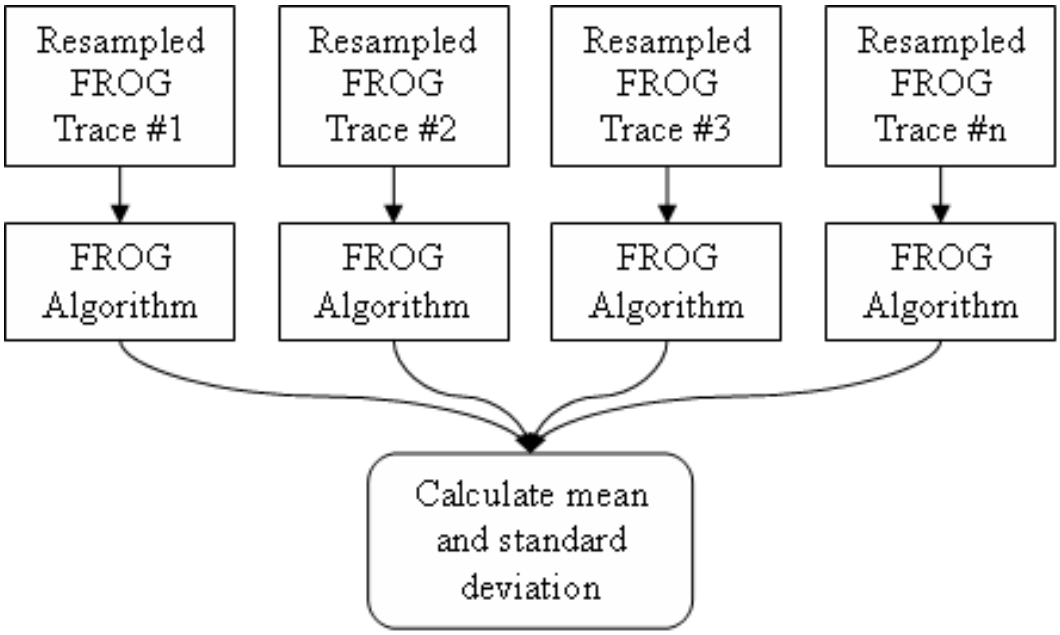

Figure 5: A Schematic of the bootstrap process. Each of the resampled traces is run through the FROG algorithm and the mean and standard deviation of the retrievals is calculated.

statistics of the retrieved intensity and phase values obtained during these runs (Figure 5). The mean intensity and phase values for each time and frequency are then the measured values, and the standard deviations yield the error bars.

The ideal number of runs in bootstrap method is infinite, because it can give us the most accurate estimation of error bars. But in practice, the number of runs is directly related to the time consumed by the algorithm, so use the least runs to get the relatively accurate error bars is the goal. Therefore in the algorithm, the number of runs is empirically determined from the numerical simulation. The simulation is designed to find out the particular number of runs, beyond which the change of error bars is ignorable. This point is searched by doubling the number of runs after each computation of the error bars. The reason to double the running times(exponentially increase) in stead of to linearly increase the number of runs is to involve an equal size new bootstrap replications every time when calculate the error bars. Therefore the change of the error bars will not be influenced by the unequal weight between old bootstrap replications and new bootstrap replications. The results show that for most traces, the length of resulting error bars will be stable in range of 10-100 runs.

To choose the subset of points according to the bootstrap procedure, we take the original, measured FROG trace and select, at random, but with replacement, a number of points equal to the original number. This allows data points to be selected more than once, and yielding about 2/3 of the points represented in this new trace. Data points not selected are simply ignored in the FROG algorithm (in the magnitude replacement step). Running the algorithm with only a fraction of the points does not harm its accuracy. Indeed, the degree to which the solution varies when points are removed is the desired measure of the error. And, as mentioned above, it has been shown that, in general, using this procedure, the statistics of the retrieved values accurately approximate the actual statistics of the derived parameters, in this case, the intensity and phase values at the various times (and frequencies). We then take the resulting mean intensity (or phase) for each time as the actual intensity (or phase), and the standard deviation at each point yields the uncertainty.

2.3.3 Dealing with Ambiguity

The implementation of Bootstrap method in the FROG algorithm is not a simple extension of the general Bootstrap method. When we come to the point of processing the bootstrap replications of the pulse field, the process involves some subtleties in its application to FROG, however, because FROG does not actually determine all pulse parameters. In particular, FROG does not measure the pulse peak intensity, I_0, the absolute phase, ϕ_0 (the $zero^{th}$-order phase in the time and frequency domains), and the pulse arrival time, t_0 (which is also the first-order term in the spectral phase Taylor expansion). For experimentalist, usually non-measurement of the absolute phase and the arrival time is advantageous, eliminating the need for tedious stabilization of irrelevant path lengths. But for Bootstrap method, these undetermined parameter will artificially introduce huge unwanted error bars. For example, if the absolute phase is allowed to float, the phase vs.time (and frequency) curve will float randomly over the full 2π range in the retrievals required for application of the bootstrap procedure, yielding phase errors of $\pm\pi/3$, even in the absence of noise in the trace! Similarly, non-measurement of the peak intensity and arrival time will cause excessive errors in the pulse intensity. Fortunately, all these parameters only have trivial

physical importance, and most researchers don't care about their values. So they can be set with any values without hurt the physical importance of the retrieved results. Thus, these parameters can be carefully fixed at the same (arbitrary) constants in each retrieval in order to properly apply the bootstrap method.

Here we only consider polarization gate FROG (PG FROG) in order to limit the number of ambiguities. In general, FROG has more ambiguities to consider; for example, second harmonic FROG (SHG FROG) has a well known direction of time ambiguity. Extra steps must be taken in these cases to eliminate the ambiguities. In the case of SHG FROG, each of the pulses must have its direction of time fixed. While this ambiguity is relatively easy to remove by inspection, others are not so easy. In fact, there is a method for removing this ambiguity from SHG FROG by placing an etalon in the beam.[12] There is also a relative-phase ambiguity in SHG FROG for well-separated pulses. This ambiguity can also be removed easily. However, this section will restrict the attention to the case of PG FROG and the three undetermined parameters mentioned above, which appear in all FROG variations. a future chapter will treat the case of a technique with potentially unknown ambiguities; the method will be a generalization of this approach.

Fortunately, it is simple to remove these ambiguities prior to performing bootstrap computations. In order to fix the delay of the pulse's arrival time, simply center the pulse, which means to shift the pulse field by moving certain *special* time on the pulse to the center of the time axis. Picking the *special* time on the pulse is the key point here. The first thought came to our mind is using the maximum intensity time(the time at which pulse field has maximum intensity). But because the pulse field in the algorithm is in a discrete form, a complex vector with N points. The point with maximum intensity is determined by how the field is sampled. So the real maximum intensity time may fall between two consecutive sampling time of the points in the pulse vector. Because in different retrievals, the points of pulse field are sampled differently, so the point with maximum intensity in the pulse field vector from different retrievals may correspond to different time. So simply fixing maximum intensity time to the center could cause an uncertainty about one unit sampling time along the time axis, even in noise free retrievals. If we take into account the

uncertainty on each retrieved intensity, using this method to center the pulse may introduce even bigger uncertainty on time axis. As a result, first moment of intensity, t0, is defined,

$$t_0 = \frac{\sum_i t_i I(t_i)}{\sum_i I(t_i)} \tag{23}$$

in which $I(t_i)$ is the intensity of the pulse at time t_i. Therefore, the shape of the pulse determines t_0. t_0 is unique to all retrievals and independents to the sampling of points. Furthermore, by integrating over whole pulse field, it minimizes the influence of the uncertainty on the intensity of the pulse field to the value of t_0.

We then *shift* the pulse so that its first moment is at $t_0 = 0$. Because t_0 define in this way will generally result a fraction number instead of a integer, the shift cannot be done by a simple permutation of the pulse vector. In order to make a fractional shift, the shift theorem of Fourier transform is utilized.[49]

$$E(t - t_0) \Longleftrightarrow E(\omega)e^{2\pi i\omega t_0} \tag{24}$$

By adding linear phase on the spectral field of the pulse, an arbitrary amount of shift can be made in time domain.

To account for the non-measurement of both I_0 and ϕ_0, simply use:

$$\hat{E}(t) = \frac{E(t)}{E(t_0)} \tag{25}$$

where the electric field of the pulse is $E(t)$ and $E(t_0)$ is the electric field at the time t_0. In a single step, it not only normalizes the intensity at t_0 to unit intensity, but it also sets the phase at t_0 to 0. It is important to note that this (artificially) removes all uncertainty in the pulse retrieval for the point at t_0. (One could estimate the uncertainty in this point by averaging that of its neighboring points.)

2.4 Testing the Bootstrap Implementation

The previous sections discussed how to implement the bootstrap method in FROG pulse retrieval. In this section, the proposed algorithm will be tested to see if it can result

reasonable error bars.

First of all, the bootstrap method is supported by a vast array of theoretical statistical analysis.[19, 49] Nevertheless, it does fail occasionally, so it is important to check that its results are reasonable in this application. This is a bit tricky because there is not currently an established method for the determination of error bars for any pulse-measurement technique! So there is no way to do independent cross check on our results.

However, there are still some sanity test cases. First, when input a theoretical trace into bootstrap algorithm, the output should be error bars of zero length. Second, the length of error bars should correspond to the amount of noise in traces.

2.4.1 Testing the Bootstrap Procedure in the Absence of Noise

In case of inputting an incomplete trace, does FROG algorithm itself introduce any uncertainty other than the trivial ambiguity mentioned above? Do we completely remove the nontrivial ambiguities by the normalization procedure discussed above? All these questions can be answered by a simple test. The test is whether error bars of zero length is obtained in the absence of noise.

In order to quantitatively control the amount of the noise in the trace, in the test, a simulated trace calculated from a theoretical pulse field is used. To challenge the capacity of the algorithm a complex triple pulse with phase jump is generated for the test, which is hardly to have in practise.

Figure 6 shows the retrieval of this pulse for a noise-free, polarization-gate (PG) FROG (the version of the FROG method that uses the polarization-gate beam geometry [53]) trace including error bars (The PG FROG trace is shown in Figure 7).

In order to quantitatively measure the uncertainty of the pulse, we defined the integrated intensity error as simply the integrated error of the intensity over the pulse:

$$S_I = \frac{\sum_{i=1}^{n} \sigma_i^I}{nI_{\max}} \tag{26}$$

S_I indicates the ratio between average intensity uncertainty and maximum intensity. Correspondingly, we define the intensity weighted phase error as:

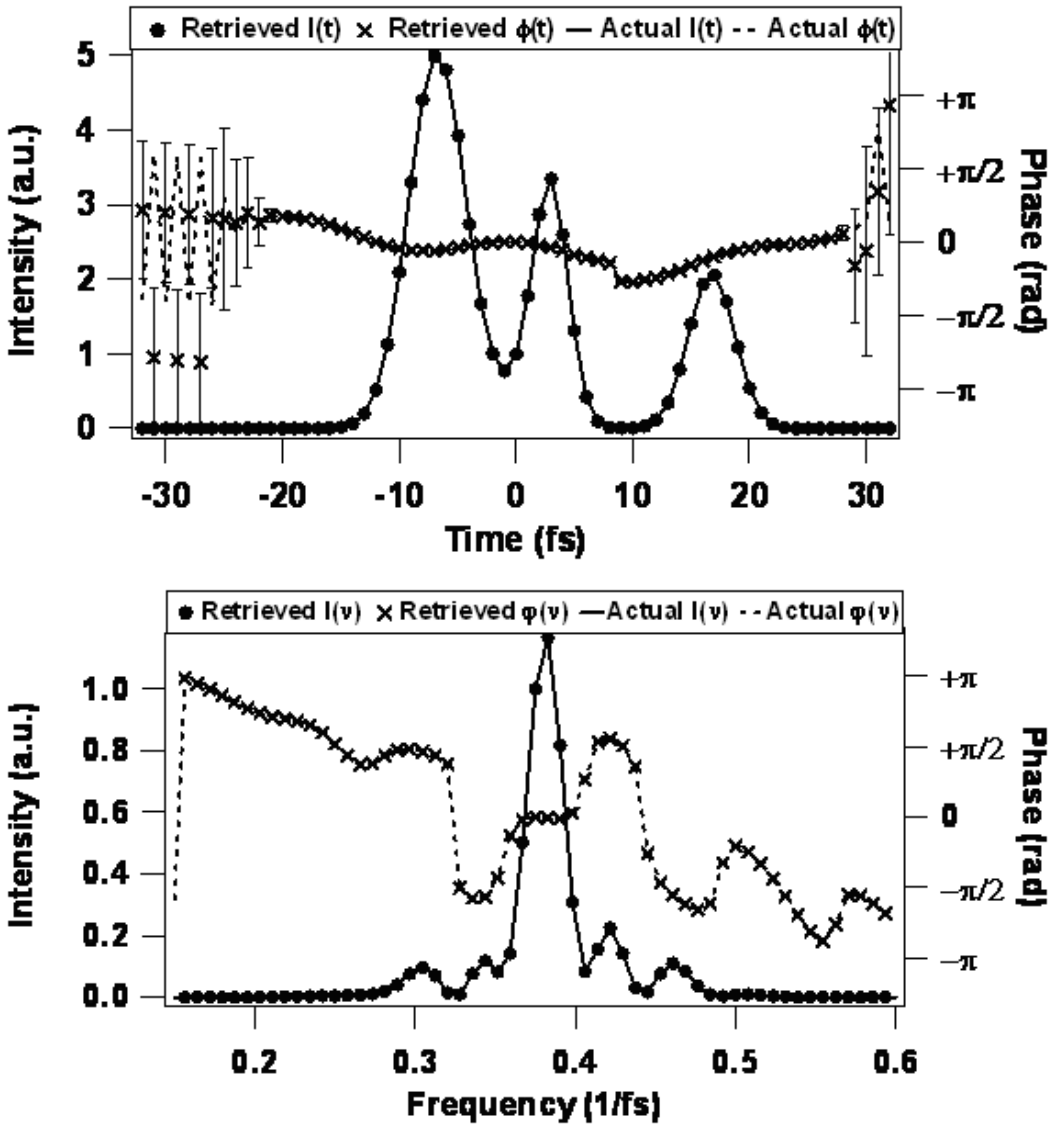

Figure 6: Retrievals from a noise-free FROG trace. Error bars have been computed using the bootstrap method as described in the text. Solid curves are the actual intensity and phase. In time, the intensity error was 1.8×10^{-6} and the intensity weighted phase error was 2.6×10^{-6}, and in frequency, the errors were 5.7×10^{-6} and 8.7×10^{-8} respectively.

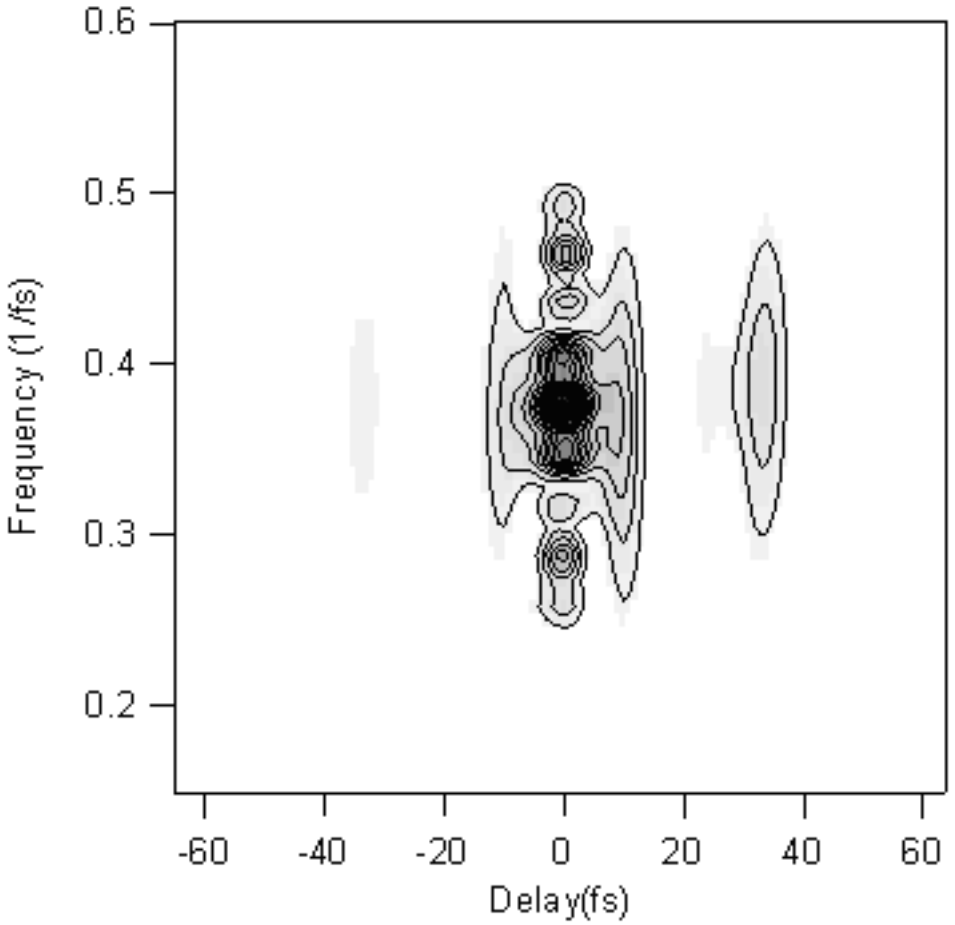

Figure 7: The PG FROG trace of the pulse used in these simulations. We designed it to be complex to challenge the proposed procedure.

$$S_\phi = \frac{\sum_{i=1}^{n} \sigma_i^\phi I_i}{n I_{\max}} \tag{27}$$

where σ_i^I and σ_i^ϕ are the mean intensity and phase standard deviations at the i^{th} time or frequency, I_i is the intensity at the i^{th} time or frequency, and I_{max} is the maximum intensity vs. time or frequency. The phase uncertainty is weighted by the intensity because the phase and its uncertainty are meaningless when the intensity is zero. Using these definitions, the integrated intensity error for this noise-free retrieval was 1.8×10^{-6}, and the intensity weighted phase error was 2.7×10^{-6} (5.7×10^{-6} and 8.7×10^{-8} respectively in frequency domain). These error values for this complex pulse and trace are measures of, not just the error due to the bootstrap method, but are in fact the sum of the errors due to the normalization procedure, the numerical round-off error of our personal computer, and the FROG algorithm itself. The low values achieved above show that all of these processes work very well.

2.4.2 Testing the Bootstrap Procedure in the Presence of Noise

After test with the noise free trace, we excluded the possibility that error bars can be generated from sources other than the noise in the FROG trace. Although it is known now that the error bars output from the bootstrap method can show the presentation of the noise in the trace, it still need to check weather the error bars can properly represent the amount of noises in traces. So the test with noisy trace is the task of this section.

The noisy traces used in the test have the additive type of noise, which is generated by adding random noise onto the noise free theoretical trace. For example, if a trace with 1% additive noise is needed. First, find out the maximum intensity of the theoretical trace $I_{trace-max}$, then use 1% of $I_{trace-max}$ as magnitude to generate the random noise for each point of the FROG trace. Finally add the noise onto the theoretical trace to get a noisy trace.

To test the performance of the algorithm on the noisy trace, first generated a 1% additive noise trace based on the theoretical trace used above. Then ran the commercial Femtosoft FROG code (modified to resample the trace as described above) on the trace.

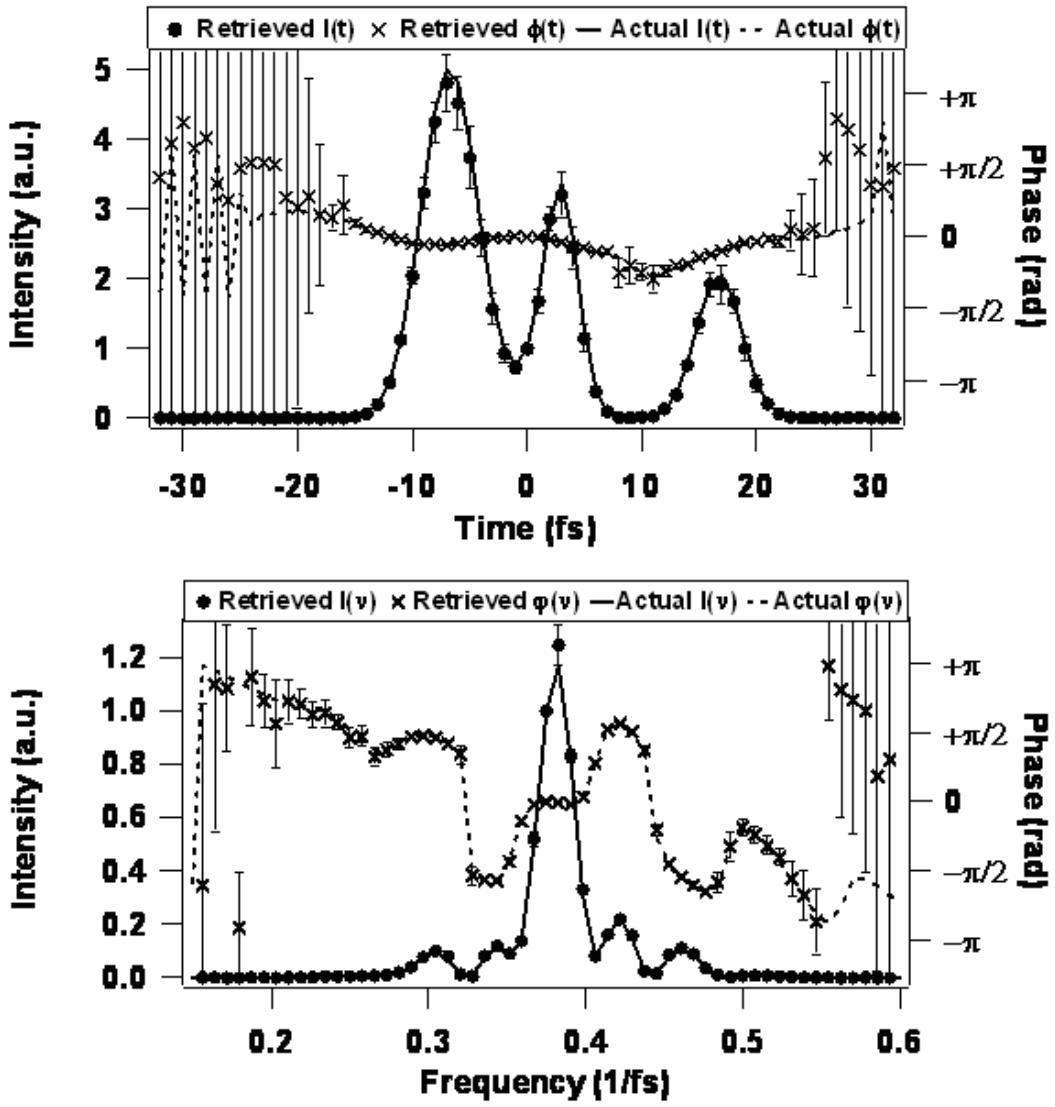

Figure 8: Retrieved intensity and phase of a theoretical pulse with 1% additive noise introduced numerically to the FROG trace. The intensity error was 9.3×10^{-3} and the phase error was 1.2×10^{-2}, and in frequency, the errors were 2.5×10^{-3} and 3.3×10^{-3}.

Fig. 8 shows the retrieved intensity and phase of the same theoretical pulse-but now with error bars determined using the bootstrap method. The error bars represent the ± 1 standard deviation points about the mean value of each retrieved intensity or phase value for each time. Note that the resulting intensity errors are on the order of 1%, but vary with intensity. The phase noise is large in the pulse wings, as expected, because the intensity goes to zero, and thus the phase there is meaningless. Note also that about 60% of the actual points fall within the error range, which indicates that this procedure is reasonable. Although the results looks reasonable, how to know these error bars are correct? Therefore, more tests are taken.

One test is to generate additional traces using the same average noise but with a different realization of the noise (a different set of random numbers). Then we can retrieve pulses from these new traces and check whether the distribution of retrieved pulses in this simulation matches those retrieved from the first set.

Figure 8 and Figure 9 show examples of two such retrievals. Both use the same FROG trace as their base, and each had the same level of noise added to them. However, the random number generator used a different seed for each trace. This gives different "noise", but with the same magnitude, for each trace. If the bootstrap method works, the retrievals are expected to give nearly identical results, which is the case. If it had not worked, the results should be different for each realization of the noise.

A second test is to show an increasing uncertainty when more noise is added to the trace. There should be a simple monotonic relationship between the computed error bars and the error added to the FROG trace.

As can be seen from Figure 10, there is a simple relationship between the amount of error in the FROG trace and the error bars calculated by the bootstrap method. The error bars in the retrieval are appropriately longer than those in the 1% cases.

This procedure has also been run for other noise levels and types and for a variety of pulses and FROG variations, and it is found to yield reasonable results in all cases.

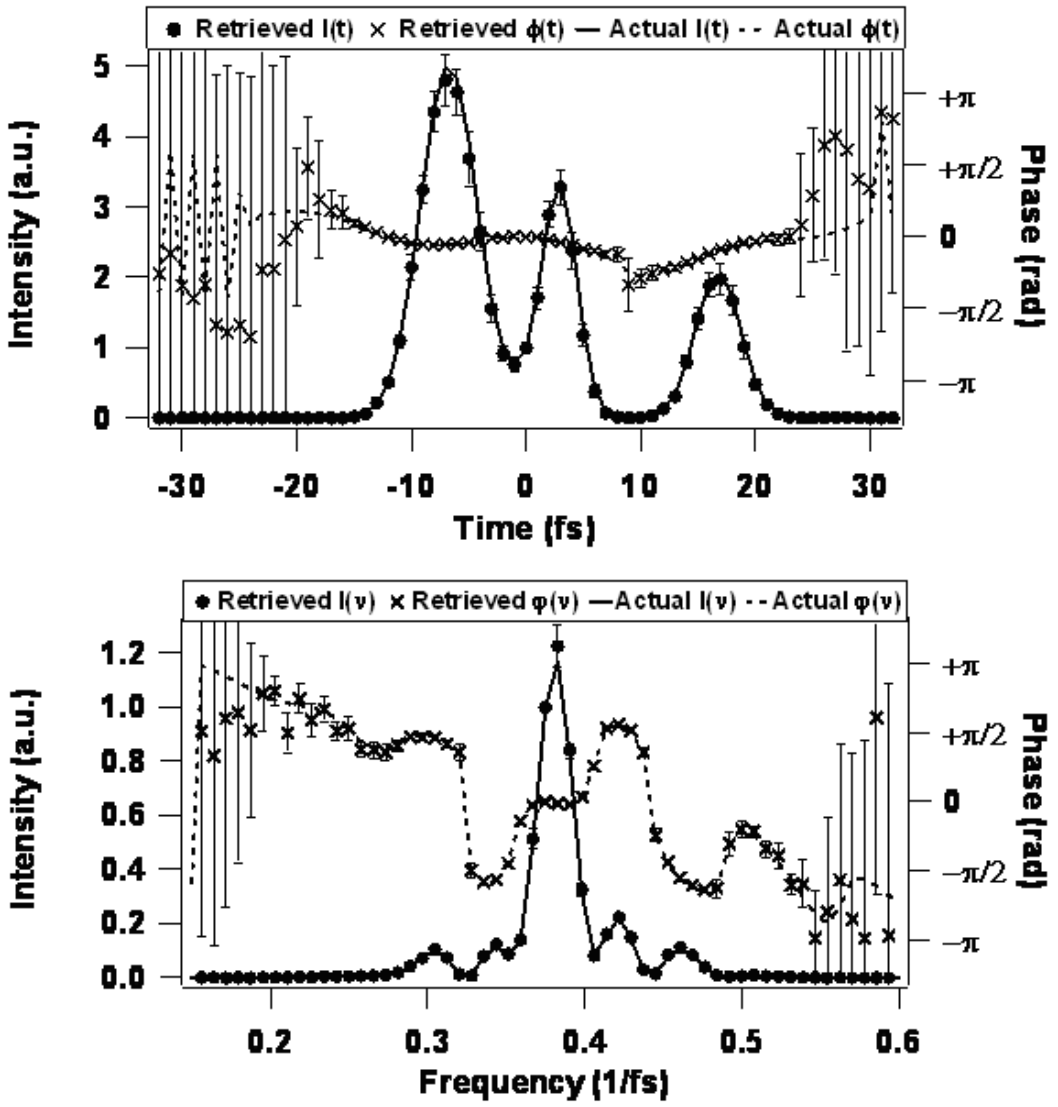

Figure 9: Retrieved intensity and phase of a theoretical pulse with different realization of 1% additive noise. Here the intensity error was 9.8×10^{-3} and the phase error was 1.1×10^{-3} (2.3×10^{-3} and 3.6×10^{-3} in frequency), essentially identical to the retrieval in Figure 8

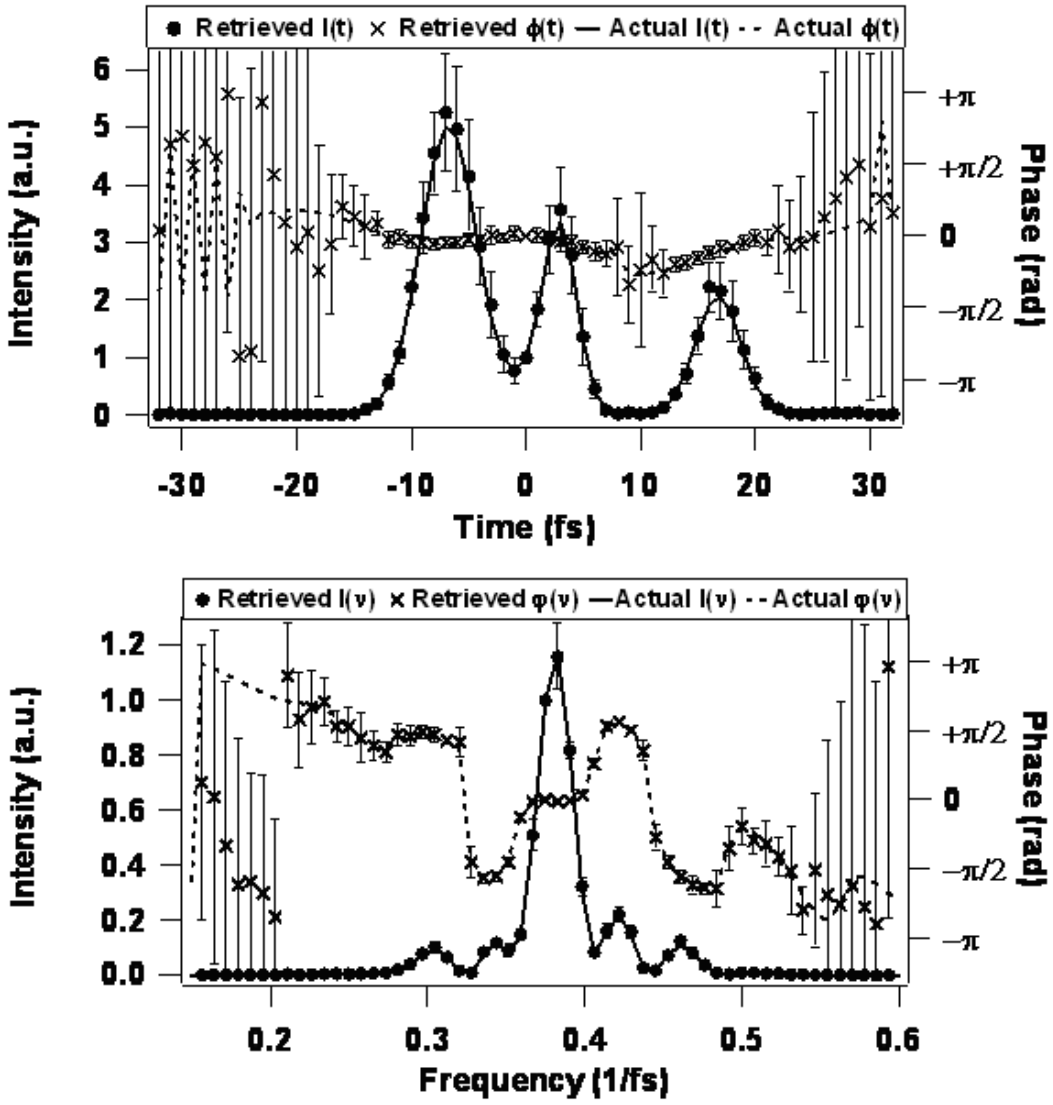

Figure 10: The pulse retrieved from the same FROG trace, but now with 10% additive noise. The error bars are about an order of magnitude larger, and the integrated errors were also larger, in time, 2.2×10^{-2} for intensity and 4.5×10^{-2} for phase (in frequency, the numbers were 5.9×10^{-3} and 1.6×10^{-2}). This confirms that the bootstrap method is working reasonably.

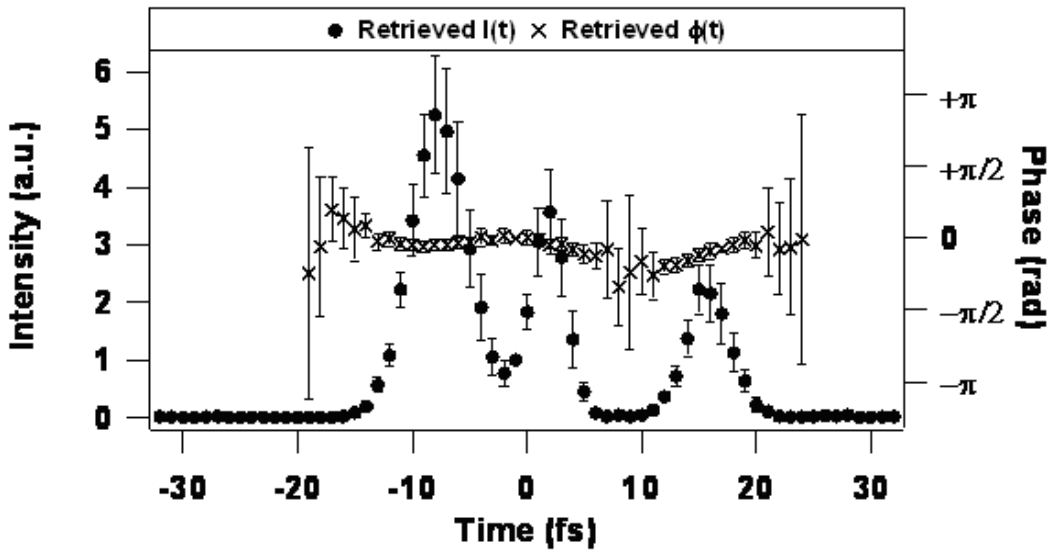

Figure 11: The pulse from Figure 10, but with phase-blanking applied. Note how the removal of the extra (meaningless) phase points simplifies the plot.

2.5 Phase-Blanking

The bootstrap method also allows us to objectively phase-blank. Figure 11 shows the advantages of phase-blanking.

Here we have taken the pulse from Figure 10 and applied our phase-blanking technique, which, as mentioned previously, involves omitting the phase when its error bar exceeds 2π in length. The result is much easier to view, without all the phase jumps in the original. The only subtlety remaining to resolve is when (and whether) to phase-unwrap (forcing the phase to be continuous by adding the appropriate multiple of 2π) and when not to. We find that phase-unwrapping during the bootstrap procedure is required, or else the phase error approaches $\pi/3$, and never exceeds 2π. After the bootstrap procedure, one can phase-unwrap or not, according to taste. Phase-blanking is especially useful when phase-unwrapping. In this case, the phase can cover a very large range even though it is only significant over a small range. This range can be arbitrarily limited, but phase-blanking provides a quantitative method for determining the limits of the phase.

2.6 Conclusions

Overall, the bootstrap method is easy to implement. It may seem that, because it requires about ten or more runs of the FROG algorithm, it could be quite slow. However, the FROG code typically requires from 0.1 s to a few seconds (rarely more than a minute, even for complex pulses) on a PC or Mac to converge. Finally, this process is convenient: it is completely automated and easily implemented, especially within the FROG code, and, unlike other error analysis, does not require a careful analysis of the experimental apparatus. Indeed, it requires only the measured trace and no additional measurements.

CHAPTER III

AMBIGUITY IN FROG

This chapter originally appeared as a paper by the author:

Ziyang Wang, Erik Zeek, Rick Trebino, and Paul Kvam, "Beyond error bars: Understanding uncertainty in ultrashort-pulse frequency-resolved-optical-gating measurements in the presence of ambiguity", *OPT EXPRESS*, vol. 11, no. 26), pp. 3518-3527, 2003.

3.1 Introduction

Ambiguity is an important topic starting from the very beginning of ultrashort pulse measurement. Because ultrashort pulses are the shortest events ever been generated by mankind, the time scale of ultrashort pulses are much shorter than that of the 'slow' electronic detectors, it is impossible to directly resolve the temporal shapes of ultrashort pulses. As a result, all the ultrashort pulse measurement techniques are based on an indirect measurement of the pulse and a pulse reconstruction procedure. During the pulse reconstruction procedure, the ambiguity of reconstructed pulses is one of the most concerned problems.

For many years, the only available measure of an ultrashort laser pulse was the autocorrelation. Unfortunately, an autocorrelation trace typically corresponds to many-often quite different-intensities, so even a perfect noise-free measurement of the autocorrelation results in a large and unknown uncertainty in the pulse's intensity vs. time. This ambiguity originates from the shortage of pulse information in the one dimension autocorrelation trace. To involve more information into measurements, some researches[44, 7, 6] took the approaches to combine several one dimensional measurements together to retrieve the pulse field, such as combining intensity autocorrelation, second harmonic field autocorrelation and power spectrum[39], then using Gerchberg-Saxton algorithm to reconstruct pulse field. But all these approaches will result undetectable nontrivial ambiguities in intensity and phase. As a result, it is not possible to determine a pulse intensity (or phase) from the autocorrelation

trace, or the combination of the autocorrelation trace with other one dimensional pulse measurement trace.

Now, methods such as FROG [53] retrieve a pulse's full intensity and phase vs. time without any assumption. FROG technique as discussed in Chapter 1, measures the two dimensional spectrograms of the ultrashort pulses. A two dimensional FROG trace is usually fully determined a one dimensional pulse field, except for a few trivial parameters, which are usually referred to as "trivial ambiguities,". Most researchers can live with them, but the trivial ambiguities nevertheless pose problems in implementing the bootstrap method as discussed in Chapter 2. Fortunately, these trivial parameters can be fixed to arbitrary constant values, therefore the bootstrap method can be successfully implemented in FROG pulse retrieval. But in some special cases, FROG technique can also involve nontrivial ambiguities, such as an ambiguity in the direction of time in the second-harmonic-generation (SHG) version of FROG, which cannot be simply set to an arbitrary constant value. How to implement bootstrap method in the presence of nontrivial ambiguities is the problem to be solved in this Chapter.

This chapter presents a method that can effectively detect the nontrivial ambiguities in FROG pulse retrieval by extending the bootstrap method implemented in Chapter 2. A way to intuitively show the ambiguity is also proposed.

3.2 Ambiguity in FROG Pulse Retrieval

In Chapter 2, several trivial ambiguities in the FROG pulse measurement were mentioned and the method to fix them for the bootstrap implementation was proposed. This chapter will revisit these ambiguities in detail, furthermore it will go through a few known nontrivial ambiguities in the FROG pulse measurement.

3.2.1 Trivial Ambiguity in FROG

As is the case for all ultrashort-pulse measurement techniques, however, there are a few ambiguities in FROG measurements. FROG does not determine the pulse height I_0, absolute phase ϕ_0, and arrival time t_0. While these ambiguities are often actually desirable (for example, it is rarely of interest to measure the distance from the laser to the measurement

device, and stabilizing it would be quite inconvenient), and they are usually referred to as "trivial ambiguities,"[53, 42, 54, 51] as most researchers can live with them.

Among the three "trivial ambiguities," I_0 actually can be determined by knowing the total pulse energy from a power meter. But because of its trivial physical importance, people rarely do that. The ambiguity ϕ_0, t_0 are rooted in the mathematical form of the FROG trace.

$$\Sigma_g^E(\omega,\tau) \equiv \left| \int_{-\infty}^{-\infty} E(t)g(t-\tau)\exp(-i\omega t)\,dt \right|^2 \tag{28}$$

The equation above shows that any constant phase $e^{i\phi_0}$ will be eliminated by the absolute square operation. Arrival time t_0 just a shift of the whole expression on the time axis. This shift will take no effect on the final FROG trace, because the integral limit is from negative infinite to infinite.

3.2.2 Nontrivial Ambiguity

There are, however, also *nontrivial* ambiguities in FROG (and all other pulse-measurement methods). These ambiguities are caused by certain special profiles of the pulses or special FROG geometries.

There are a set of special pulses, which have well-separated components in time or frequency. These pulses will cause nontrivial ambiguity in some versions of FROG. For example, in SHG FROG, well-separated pulse in time domain, when the relative phase between two components changes from ϕ_0 to $\phi_0 + \pi$, the FROG trace will make no change. Also, pulses with well-separated frequency components have undetermined relative phases (in FROG and all other pulse-measurement techniques used today, except for XFROG with an appropriately chosen reference pulse).[37]

On the other hand, the speciality of FROG geometries, which determine the mathematical forms of the FROG trace, may introduce nontrivial ambiguities too. One case of them is the ambiguity in the direction of time in the second-harmonic-generation (SHG) version of FROG, whose traces are necessarily symmetrical in delay and hence cannot distinguish a pulse from its time-reversed replica. In terms of the complex amplitudes, this means that

$E(t)$ and $E^*(-t)$ are both possible phases. This ambiguity is a nontrivial ambiguity and cannot be reliably removed using a normalization procedure, as described in Chapter 2.

3.3 Implementation of the Bootstrap Method on FROG trace with Nontrivial Ambiguity

Chapter 2 discussed the implementation of the bootstrap method in the FROG pulse retrieval to determine the uncertainty on the retrieved pulse filed. But in the discussion, the FROG traces were limited to those only have trivial ambiguities. This chapter will discuss how to determine uncertainty on retrieve pulses when nontrivial ambiguities present in FROG traces.

3.3.1 Problems in Implementation

In order to apply the bootstrap method on the FROG pulse retrieval, it has to eliminate trivial ambiguities by using a normalization procedure. The normalization procedure fixed each of the random parameters I_0, ϕ_0 and t_0 to a constant value, because leaving these parameters free, will cause unwanted arbitrary error bars on output. But for the nontrivial ambiguity, as it named, it cannot be simply fixed to certain constant value as people want, because that will most probably change the physical meaning of the retrieved pulse field. While, an unfixed nontrivial ambiguity will yield inappropriate error bars, for example, the presence of the direction-of-time ambiguity in SHG FROG. Figure 12 shows that, for a given SHG FROG trace, the parabolic phase could have a positive or negative leading coefficient (that is, the parabola could "hold" or "spill" water). In the presence of this ambiguity, the bootstrap method, as previously described, would yield a nearly flat phase with increasingly large error bars as time (or frequency) approaches the plot edges. This is in strong contrast to our knowledge of the pulse phase from the measurement, which is quite accurately either one parabola or the other, and definitely not flat.

While it is conceivable that the direction-of-time ambiguity and other nontrivial ambiguities can be removed as the trivial ambiguities, technically, a *general* method for dealing with ambiguities would be preferable. Indeed, it is possible that there are other, as yet undiscovered, ambiguities, and it's better to account for them in advance even if they are

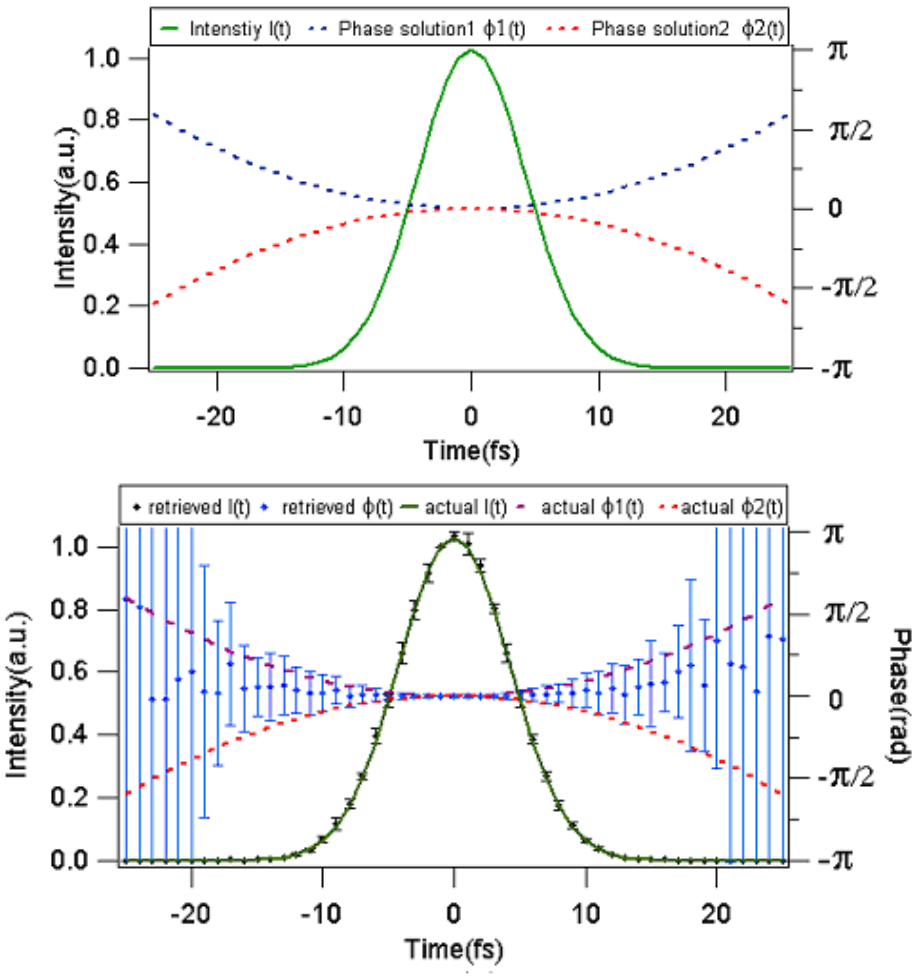

Figure 12: a. The intensity (green curve) and the two possible phase solutions (red and blue dashed curves) in an SHG FROG measurement of a linearly chirped pulse. Even in the absence of noise in the trace, half the bootstrap retrieved pulses would yield one phase solution and half would yield the other. Of course, only one is correct. b. The retrieved intensity and phase using the bootstrap method for the same pulse (in the presence of 1% additive noise, although this is not important). Note that both the retrieved phase and its error bars are unacceptable, giving the impression that the most likely phase is approximately flat with increasingly large errors near the plot edges, rather than the correct result that the phase is quite accurately one parabola or the other.

still unknown.

In one word, direct implementation of bootstrap method as in Chapter 2 in presence of nontrivial ambiguity will cause unreasonable error bars.

3.3.2 Analysis of the Problems

Before start to solve the problem, it need full understanding of the problem. To understand where the problem came from, let's first go through the bootstrap method again. Bootstrap method in the FROG pulse retrieval can be separated into two major steps. Step one, calculating the bootstrap replications by the computer simulation. Step two, collecting bootstrap replications and calculating error bars. From the example in section 3.3.1, it is still successful in first step of the procedure, because two groups of solutions with expected phases were accurately retrieved. The problem appeared when the error bars were calculated. As discussed in Chapter 2, error bars are estimated by the calculation of the standard deviation. Standard deviation is a statistic that tells you how tightly all the various examples are clustered around the mean in a set of data. This definition of standard deviation is based on an assumption that the set of data are in normal distribution, or at least in uni-modal. In the presence of the ambiguity, however, the distribution of values will no longer be near-normal, and usually are bi- or multi-modal (or flat in the case of a completely undetermined parameter). As a result, the standard-deviation estimation of the error bars is failed inevitably.

So the problem is standard-deviation estimation of the error bars is not suitable for the bi- or multi-modal distributions. Therefore it need figure out a new way to present distributions which is not uni-modal.

3.3.3 Solving the Problems

Fortunately, as mentioned, the bootstrap method yields the full probability distribution of retrieved values and clearly reveals the bi-modal distribution of phase values in, for example, the direction-of-time ambiguity in SHG FROG. So the problem now is how to display the distribution which is not uni-modal properly.

First thought is to plot all the bootstrap replications together to show the distribution

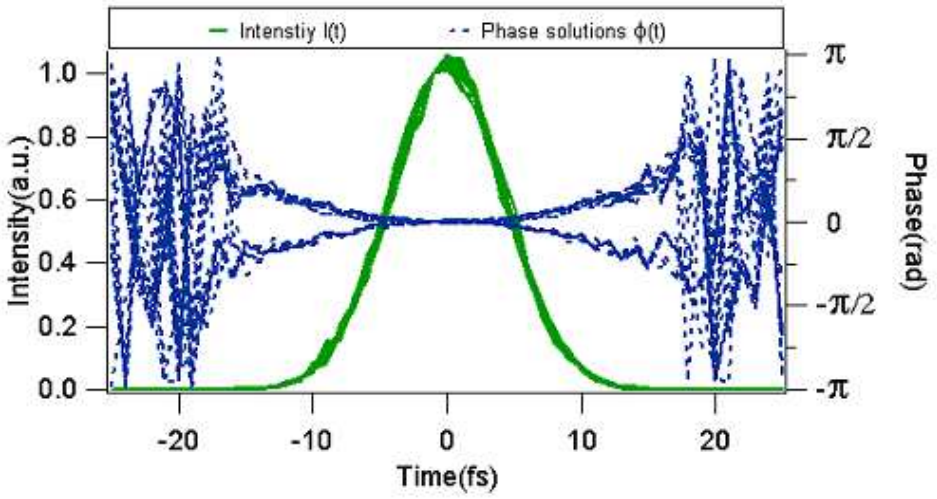

Figure 13: The entire set of bootstrap solutions for the linearly chirped pulse in Fig. 12. Note that this display much better reveals the true uncertainty in the measured intensity and phase.

of the retrieved values.

Figure 13 shows a plot of several of the bootstrap solutions obtained for the pulse in Fig. 12. Note that the two possible phase parabolas emerge, with essentially no values in between. (Do not be distracted by another effect: the fact that the phase becomes random in the wings of the pulse when the intensity goes to zero, reflecting the phase's fundamental indeterminacy for near-zero intensities.) This plot much more accurately reveals the distribution of retrieved values and the error distribution. Thus, when ambiguity is present, it is important to show, not just error bars, but the complete distribution of retrieved values, that is, the complete set of bootstrap solutions. Plotting all bootstrap solutions reveals the true distribution of values and yields a far superior picture of the information in the measurement. (It also nicely reveals the phase indeterminacy when the intensity is zero.)

But this solution has its major disadvantage. We know every bootstrap solution contains a set of points of intensity and phase. When plot all the bootstrap solutions together, it clearly shows the distribution on certain time or frequency point, but the coupling between different time or frequency points is blurred. In another word, it is unable to tell which set of points of intensity and phase are belonged to the same bootstrap solution. In some special cases, this decoupling may cause major understanding problem of the solution. When such

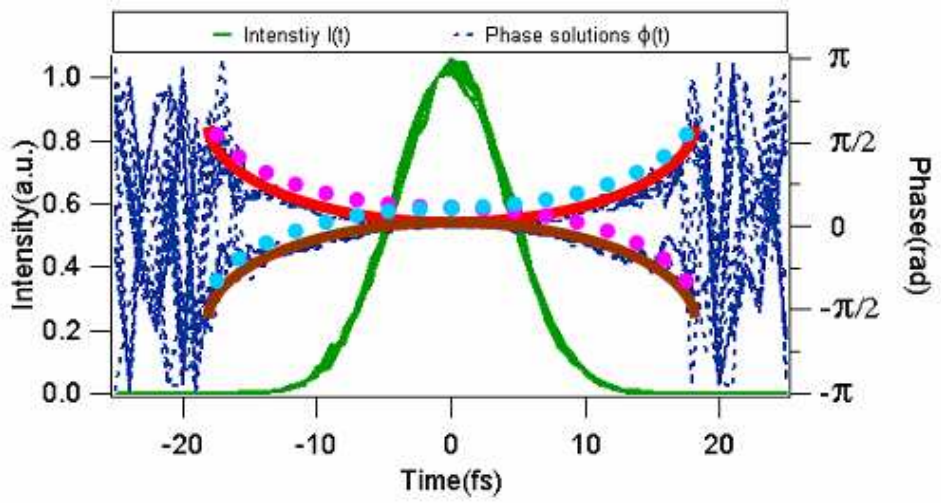

Figure 14: Two incorrect saddle-shaped phase curves that could be mistaken for the actual parabolic phase in Fig. 13(shown as blue and purple dots in the plot). Such confusion occurs any ambiguous curves intersect.

ambiguous solutions overlap at a point, however, simply plotting all solutions may not remove all sources of confusion. For example, for the above linearly chirped pulse, a source of confusion remains. The ambiguous solutions cross at $t = 0$, and it is not clear, simply by looking at Fig. 13, whether the negative-going solution at negative times continues to be negative-going for positive values of time or whether it becomes positive-going. In other words, the plot could be consistent with saddle-shaped curves in addition to parabolas (see Fig. 14.). Thus, in order to maintain the relation of those points belong to same solution, it is helpful to use different colors or a movie of the various bootstrap solutions to portray the bootstrap solutions(In this thesis just use different colors to display the solutions. Interested readers can refer to reference paper 47 for the movies). Fig. 15. shows the various solutions for the linearly chirped pulse, much better revealing both the ambiguity and noise.

3.4 Extension of the Bootstrap Technique in FROG pulse retrieval

One important observation in the implementation of bootstrap method in presence of non-trivial ambiguities, is there is no special treatment on the trace or algorithm to cope with the ambiguous trace, while the algorithm *automatically* tells us *correct* multiple solutions. It looks like the bootstrap method thoroughly scans over the whole solution space to find

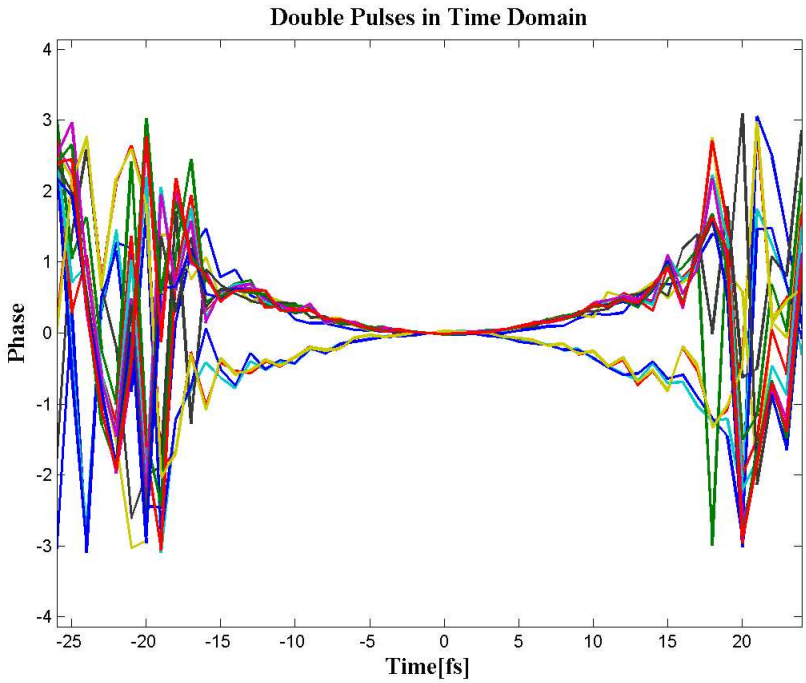

Figure 15: Distribution of bootstrap solutions of linear chirped pulse from SHG FROG trace. It clearly reveals the ambiguity and noise of the result.

all possible solutions. So an idea hit us: Can bootstrap method automatically detect the unknown ambiguity in FROG pulse retrieval? To prove this idea, it is tried to test this approach by all the known nontrivial ambiguities. If it can correctly find all of the ambiguities, then the approach can be claimed as an effective way to detect the unknown ambiguity in the FROG pulse retrieval.

Therefore some additional cases of the nontrivial ambiguities are considered.

First, we consider the case of well-separated pulses in time, whose relative phase is ϕ_0, but which, in SHG FROG, cannot be distinguished from another relative-phase value, $\phi_0 + \pi$. Figure 16 shows the SHG FROG trace for such a pulse, and Fig. 17. shows the various bootstrap solutions obtained in this case. In addition, well-separated frequency components have undetermined relative phases. Fig. 18. shows the bootstrap solutions for polarization-gate (PG) version of FROG trace in this case.

After all these tests, the bootstrap method successfully identified the ambiguities as we expected. Especially, in case of undetermined relative-phases in well-separated frequency

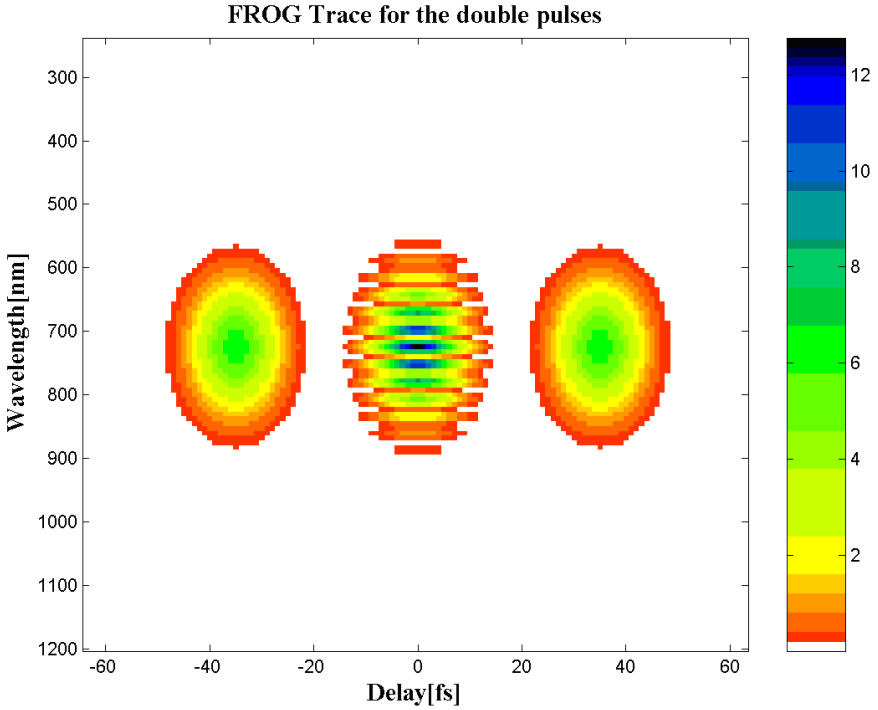

Figure 16: SHG FROG trace for a double-peaked pulse with a relative phase of between two peaks.

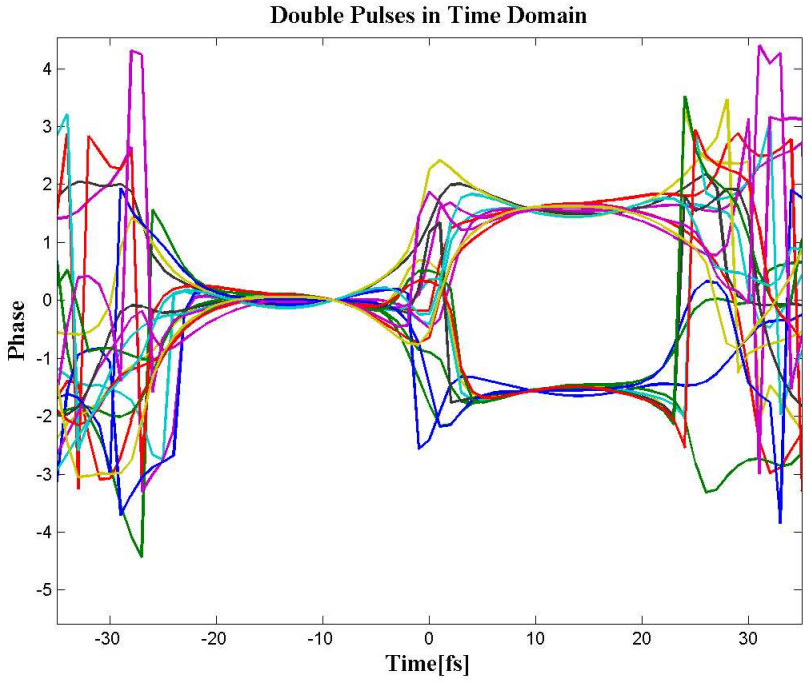

Figure 17: Distribution of bootstrap solutions for the well-separated doubled-peaked pulse in time. In the plot, the first pulse's phase is set to zero for all pulses.

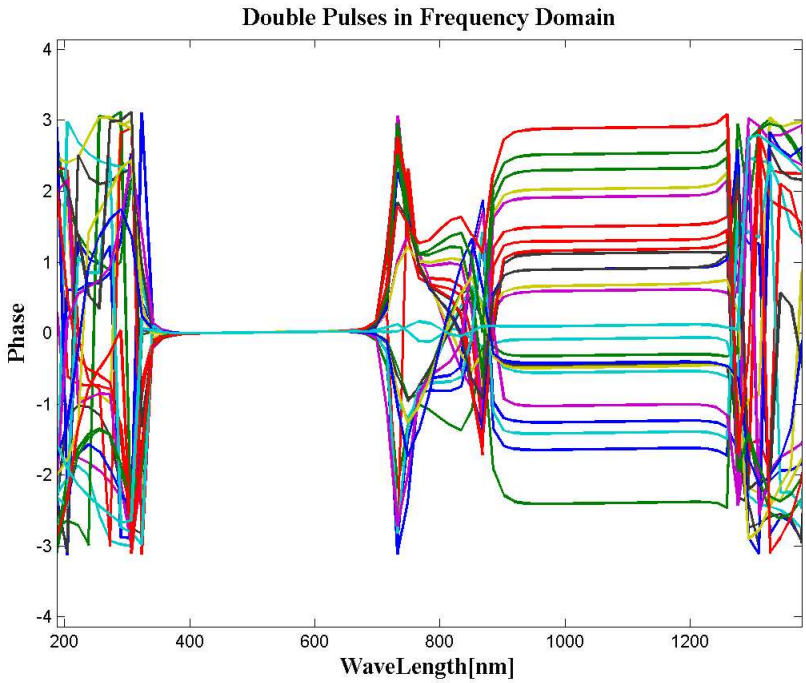

Figure 18: Distribution of the bootstrap solutions of a pulse with well-separated frequency components. In this plot the phase of the first spectral component was set to zero for all retrieved pulses.

components, the bootstrap method actually gives out uniformed distribution on the unfixed side. It attests the guess that bootstrap method can scan through the whole solution space. Now bootstrap method can be claimed as an effective way to detect ambiguities in the FROG pulse retrieval. On the other hand, if bootstrap method shows no ambiguities in a FROG pulse retrieval, it can empirically say there is no ambiguity in the retrieval even without rigorous prove.

3.4.1 Approximate Ambiguities

Another interesting case is the possibility of "approximate ambiguities." Approximate ambiguities have not previously been discussed in the literature, but we define them to be additional, qualitatively different solutions that are consistent with the data in the presence of noise, but which are easily ruled out in the absence of noise.

Approximate ambiguities will also reveal themselves by a double-peaked distribution in the bootstrap solution set in the presence of noise. Here we show that an approximate

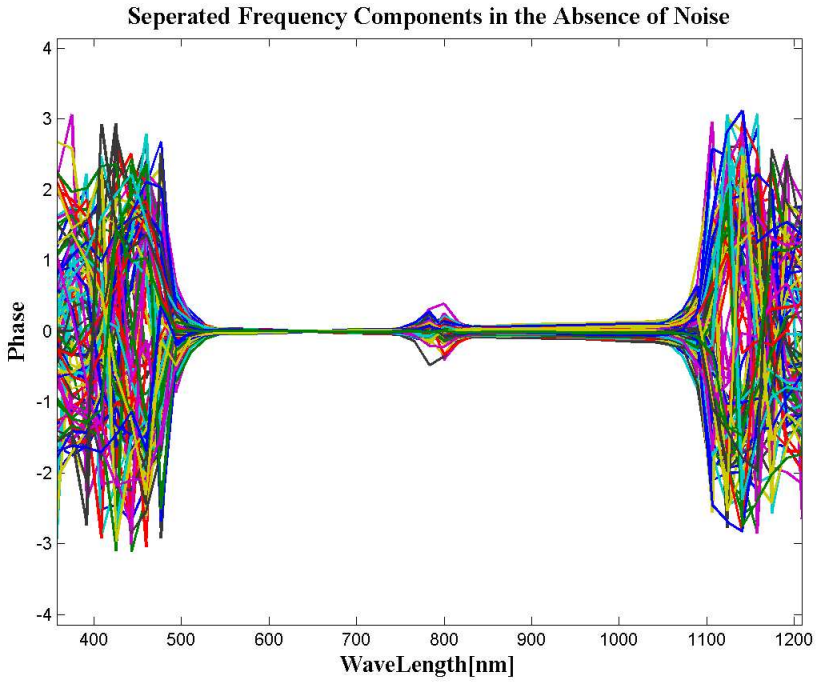

Figure 19: Bootstrap solutions for a noise-free FROG trace for a pulse with somewhat separated spectral components. Note that the solutions accurately determine the relative phase of the frequency components (although some uncertainty is beginning to appear in the phase of the second component).

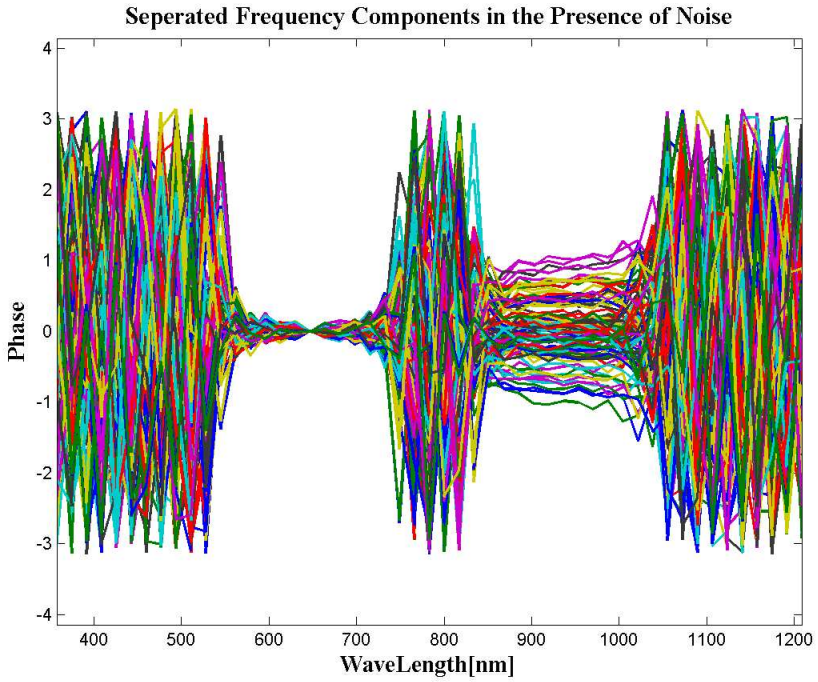

Figure 20: Bootstrap solutions for a FROG trace for a pulse with somewhat separated spectral components, here with 1% additive noise added to the trace. Note that the solutions no longer accurately determine the relative phase of the frequency components (although the uncertainty is not yet 2π).

ambiguity is represented by the case of two "somewhat separated" frequency components, whose intensities overlap enough to prevent ambiguity in their relative phase in the absence of noise. But when some (here 1% additive) noise is added to the FROG trace, the well-separated frequency-component-phase ambiguity appears. Figure 19, 20 shows the bootstrap solutions for the noise-free and noisy traces.

3.5 Conclusions

The bootstrap method allows us to characterize the uncertainty in the measured pulse intensity and phase in the presence of noise-and ambiguity-by generating a complete distribution of possible values for the desired parameters. By plotting, not simply traditional error bars, but instead all the bootstrap solutions, we can see the entire distribution of solutions in the absence of, or in the presence of, ambiguities. This is very useful and can be used for all measurements with FROG or any other method that involves more data points than are absolutely required to determine the desired pulse parameters. It will also be useful for finding new ambiguities (if they exist) and for finding "approximate ambiguities," that is, very different pulses that do not have identical traces, but traces that differ by less than the noise present in a particular measured trace. In short, the bootstrap method is a simple, powerful, and general method that is ideal for determining the uncertainty in ultrashort pulse measurement whether in the presence of ambiguities or not.

CHAPTER IV

SPATIO-TEMPORAL DISTORTIONS

4.1 Introduction

For decades, ultrashort-pulse-measurement community has used an often oversimplified model for an ultrashort laser pulse, in which the space and time field dependences are assumed to be separable. In reality, coupling may occur between the electric field's space and time dependence, which is referred to as a spatio-temporal distortion. Two of the most common such distortions are spatial chirp (in which the average wavelength of the pulse varies spatially across the beam) and pulse-front tilt (in which the pulse intensity front is not perpendicular to the propagation direction). These distortions are very common in ultrafast optics, because the generation, amplification, and manipulation of ultrashort pulses all involve the deliberate introduction (and hopefully the subsequent removal) of massive spatio-temporal distortions. Researchers have struggled to make resulting pulse 'clean' (free of such distortions), but minor misalignments are common in these operations, and as a result, ultrashort pulses are often contaminated with spatio-temporal distortions. Indeed, the broadband nature of ultrashort pulses makes them particularly vulnerable to these distortions.

FROG as discussed in previous chapters, is one of the most popular and effective ways to measure the temporal evolution of the intensity and phase of ultrashort laser pulses.[53] A new variation of FROG, called grating-eliminated no-nonsense observation of ultrafast laser-light e-fields (GRENOUILLE) [47], is known for its low cost, compact size and user-friendly operation. We have recently shown that in addition to measuring temporal pulse characteristics, GRENOUILLE is able to reveal spatial chirp and pulse-front tilt [2, 3], without a single modification in its hardware. Specifically, spatial chirp causes a shear, and pulse-front tilt causes a delay shift to a FROG or GRENOUILLE trace, which is otherwise symmetrical with respect to delay. However, such intuitive descriptions are only valid for

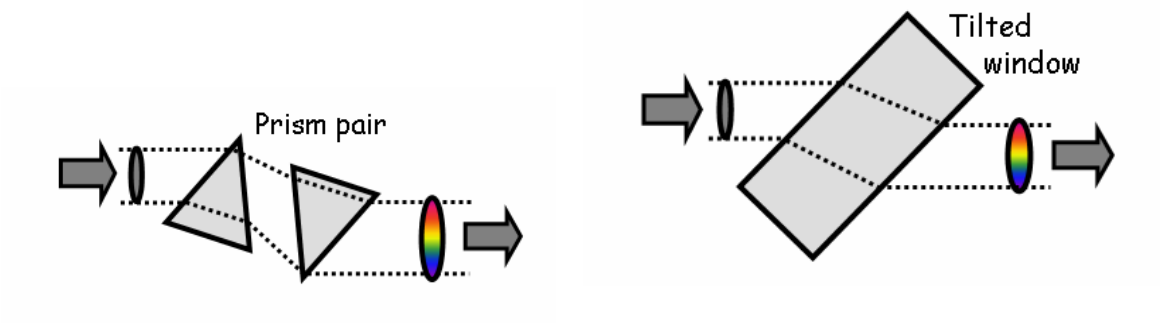

Figure 21: Prism pairs and simple tilted windows cause "spatial chirp."

pulses having a simple form of spatial chirp, called frequency gradient. For more realistic pulses, which are usually contaminated with a type of spatial chirp, called spatial dispersion, the distortion to the FROG or GRENOUILLE trace is more complicated, which not only prevents one from retrieving spatio-temporal distortions in a simple manner, but also affects the accurate measurement of the pulse's temporal characteristics.

In this work, a rigorous GRENOUILLE model with spatio-temporal distortions was established. By using this model, the GRENOUILLE trace of an arbitrary input spatiotemporal field can be calculated. Then a new FROG retrieval algorithm is demonstrated, which is capable of accurately retrieving both the pulse temporal characteristics and spatio-temporal distortion parameters from the distorted GRENOUILLE trace. Such an algorithm is a major modification of the current commercial FROG retrieval programs.

4.2 Spatio-temporal Phenomenon in Ultrashort Laser Pulses

Spatio-temporal distortion is the coupling between the space and time dependence of pulse field. Two of the most common such distortions are spatial chirp and pulse-front tilt. Many common used optical components, such as prism, grading, even a tilted window, can introduce such kind of distortions, as shown in Fig. 21 and 22.

Ultrashort laser pulses are especially vulnerable to these distortions. First, because of essentially broadband of ultrashort pulses, the influence of dispersive components (prism, grading,.etc) are considerable. Second, during the life time of any ultrashort pulses, it is inevitable to encounter the components described above. In generation of the ultrashort

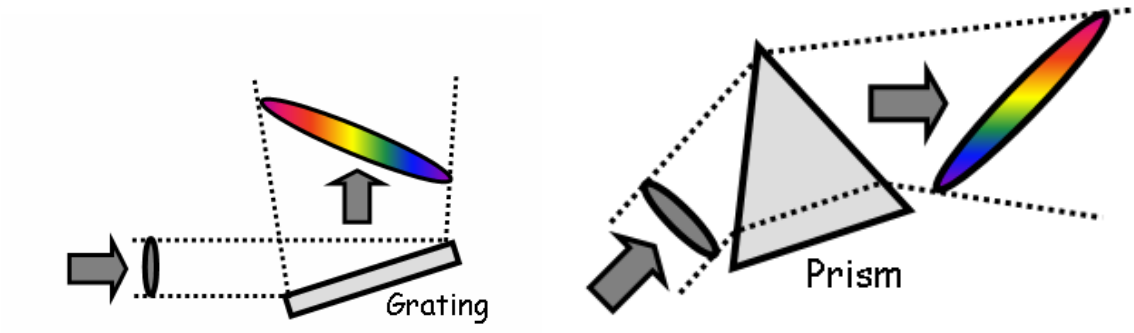

Figure 22: Gratings and prisms cause both spatial chirp and "pulse-front tilt."

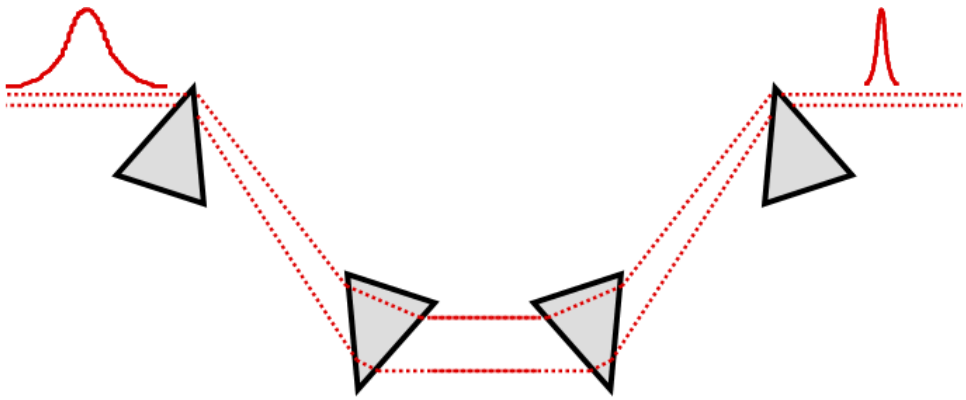

Figure 23: A prism compressor, which is consisted of four identical Brewster prisms.

pulses, a pulse compressor(see Fig. 23) is standard in most ultrafast laser apparatuses.

After the first prism pair, dramatic spatial chirp is introduced into the pulses. If the second prism pair is perfectly symmetric to the first pair, then the spatial chirp in pulses can be removed. But in practice, the minor misalignments are common, as a result the output pulses are often contaminated by the spatial chirp. Another improved design of compressor uses a mirror to replace the second pair of prism. The new design reduced the alignment dramatically. But because of the diffraction nature of propagation of electric waves, the laser beam may diverging or converging in the device, so there is no guarantee that certain color will travel back on the same route as it incident in. Plus that two prisms may have slight misalignments, even in such simple design spatial chirp may be caused in the output pulses. There are many other cases in which the ultrashort pulses are routinely introduced huge mount of spatio-temporal distortions then removed later, such as stretching

and compressing processes in pulse amplification. Any misalignments of these procedures will cause the resulting pulses contaminated by spatio-temporal distortions.

Experiments which used the spatio-temporal contaminated pulses, may get inappropriate data. So knowing the information of spatio-temporal coupling in ultrashort pulse will help people understand their experimental results correctly. GRENOUILLE, a compact version of FROG technique, can easily measure the spatio-temporal distortion in ultrashort pulses without a single modification on hardware.[2][3] But the information of spatio-temporal distortions is not directly revealed in the GRENOUILLE measurement. It is shown as distortions in the measured GRENOUILLE traces. How to understand these distortions in the GRENOUILLE traces and how to retrieve spatio-temporal information out of the distorted GRENOUILLE traces are the problems which will be discussed in this work.

4.3 Numerical Modelling

In case of the simple pulses, spatio-temporal coupling in ultrashort pulses influences the GRENOUILLE traces in a simple manner. Specifically, spatial chirp causes a shear, and pulse-front tilt causes a delay shift to a GRENOUILLE trace. But in case of the complex pulse fields, the distortions in GRENOUILLE traces cannot be simply described as a shear or a shift. Fig.24 shows that in cases of the complex pulses the behaviors of distortions in GRENOUILLE traces are complex.

So in order to retrieve the spatio-temporal information in the ultrashort pulses from the GRENOUILLE traces with complicated distortions, a new rigorous mathematical model is required to describe the new situation which includes a new model for ultrashort pulses and a new GRENOUILLE trace model.

4.3.1 A New Model for Spatio-temporal Distorted Ultrashort Pulses

The original mathematical description of ultrashort pulses is:

$$E(t) = \mathrm{Re}\left\{\sqrt{I(t)}\,\exp\left[i(\omega_0 t - \phi(t))\right]\right\} \tag{29}$$

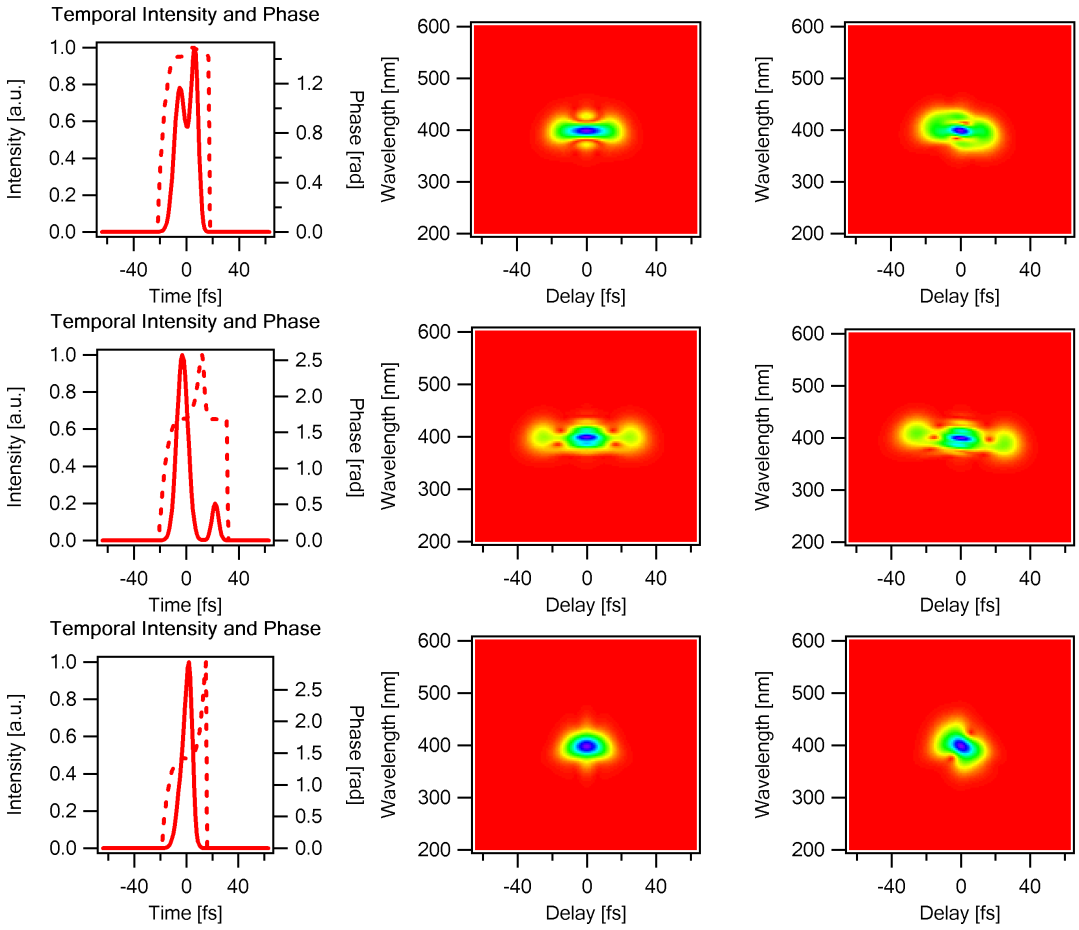

Figure 24: First column shows ultrashort pulses in different temporal profile; second column is the GRENOUILLE traces generated by pulses in first column; Third column contains GRENOUILLE traces of first column pulses under spatio-temporal distortions.

The model in Eq. 29 automatically assumes that the spatial profile of the pulse is constant. All the spatial information is eliminated from this model, doesn't even mention the coupling between the spatial and temporal characteristic of the pulse. Therefore the new model is essentially a 2D model which includes both time dimension, t, and space dimension, x.

$$E(t) \rightarrow E(t,x) \tag{30}$$

As discussed above, the sources of spatio-temporal distortions are some dispersive optical components, such as prism, grating, tilted window, etc. One common feature of the dispersive optical components is that they treat electric fields differently by their frequency. According to this observation, it is assumed that the spatial profile of each individual frequency component in the ultrashort pulse is invariant after the pulse went through optics mentioned above. Furthermore, if the pulse coming out of laser is assumed to be free of the spatio-temporal distortions, then each frequency component of the pulse will have same spatial profile. Therefore it is more intuitive to describe the new pulse model in the frequency domain instead of the time domain. In the frequency domain, the pulse front tilt is represented as the angular dispersion. Equation 31 is a general ultrafast beam with spatial dispersion and angular dispersion.

$$E(x,\omega) = E(\omega)\, f(x - x_0(\omega)) \exp(-\mathrm{i}k\beta\omega x) \tag{31}$$

where

$f(x)$ is the spatial profile of an individual frequency component.

$x_0(\omega) = \sum_{n=1}^{\infty} \frac{\zeta_n}{n!}\omega^n$is the beam center position of frequency ω.

β is the parameter for angular dispersion.

In this model, spatial chirp is parameterized as $\zeta_n, n = 1, 2, 3...$, and angular dispersion is parameterized as β.

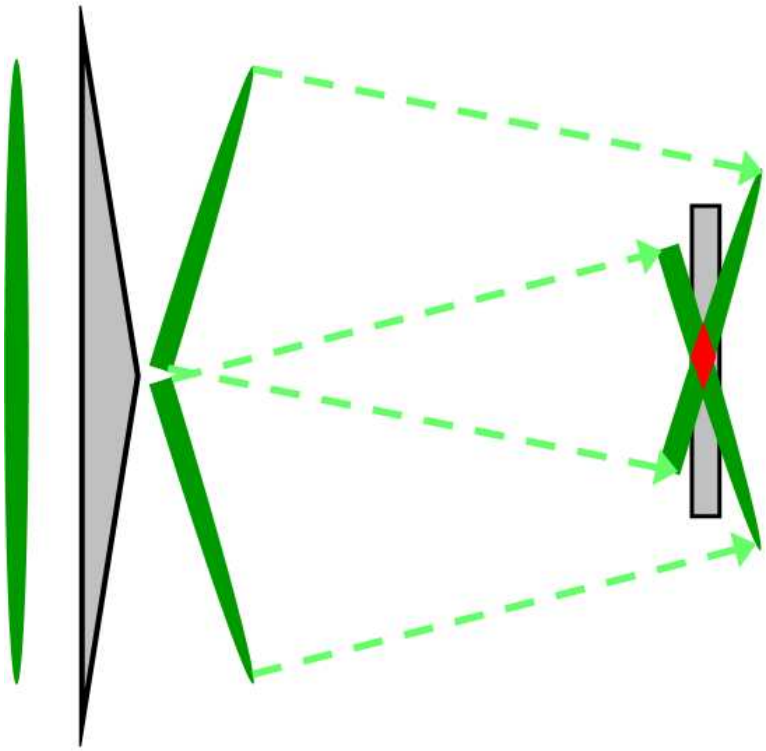

Figure 25: Two halves of the beam are crossed at the nonlinear crystal to generate second harmonic signal.

4.3.2 New Model for GRENOUILLE Trace

With the new pulse model, the standard way of calculating the GRENOUILLE trace from the pulse field $E(t)$ is not applicable for $E(x,\omega)$. Now a new GRENOUILLE trace model is needed to calculate the GRENOUILLE trace from the new ultrashort pulse model,$E(x,\omega)$.

In GRENOUILLE, an input beam is divided spatially into two half beamlets which are crossed by the biprism and then overlap at the nonlinear crystal to generate the second harmonic signal, as shown in Fig.25

As shown in Fig.25, after propagating a distance of L to the SHG crystal, the two beamlets will shift laterally by $L\theta$, in opposite directions. Therefore, by taking in the spatial parameters of GRENOUILLE device, L,θ, the GRENOUILLE field of spatio-temporal distorted pulses can be calculated in following way.

$$E_{GREN}(x,\omega) = \int E\left(x - L\theta, t - \frac{\theta x}{c}\right) E\left(x + L\theta, t + \frac{\theta x}{c}\right) \exp(-i\omega t)\, dt \qquad (32)$$

Where

L is separation between the biprism and crystal.

θ is one half of crossing angle of two pulse replicas generated by biprism.

c is speed of light.

If define $A(x,t;\theta) = E\left(x - L\theta, t - \frac{\theta x}{c}\right)$, then the GRENOUILLE trace in the frequency domain can be written as:

$$E_{GREN}(x,\omega) = \int A(x,t;\theta)\, A(x,t;-\theta) \exp(-i\omega t)\, dt = \tilde{A}(x,\omega;\theta) * \tilde{A}(x,\omega;-\theta) \tag{33}$$

Where

$\tilde{A}(x,\omega;\theta)$ is the Fourier transform of $A(x,t;\theta)$ on variable t.

$*$ is the convolution performed only on ω

4.4 New FROG Algorithm

With the new pulse and the trace model, we can numerically simulate the GRENOUILLE traces which are transformed by the spatio-temporal distortions. But to retrieve both the temporal field and the spatial parameters from the measured distorted GRENOUILLE traces, an new FROG algorithm need to be developed.

4.4.1 Problem Analyzing

With the new pulse model and the trace model, the FROG pulse retrieval problem shows some new features. Comparing to the minimization objective function in the regular SHG FROG:

$$G(E(t)) = \left| I_{FROG}(\omega,\tau) - \left| \int_{-\infty}^{-\infty} E(t)E(t-\tau)\exp(-i\omega t)\, dt \right|^2 \right|^2 \tag{34}$$

The minimization objective function for the new model is:

$$G(E(t), f(x), \zeta_n, \beta) = \left| \left| \tilde{A}(x,\omega;\theta) * \tilde{A}(x,\omega;-\theta) \right|^2 - I_{GREN}(x,\omega) \right|^2 \tag{35}$$

where

$$\tilde{A}(x,\omega;\theta) = E(\omega) f\left(x - \sum_{n=1}^{\infty} \frac{\zeta_n}{n!}\omega^n\right) \exp(-\mathrm{i}k\beta\omega x) \tag{36}$$

New features in the new object function are:

1. The number of parameters which need to be determined has increased. In the regular FROG, only the pulse's temporal field, $E(t)$, is required to be found out. Here, the spatial profile of the pulse $f(x)$ and the spatio-temporal parameters ζ_n, β are all undetermined variables. But the GRENOUILLE trace size does not change. Can GRENOUILLE trace, which is programmed for encoding only the temporal field of ultrashort pulses, determine all these new parameters? The answer is: it is possible. Because a GRENOUILLE trace is highly over determined the temporal field, the GRENOUILLE trace probably also contains the spatial information.

2. In the new objective function, the position x relates to the delay of the GRENOUILLE trace. As a result the translation between the hybrid time-frequency domain to frequency domain is no longer a Fourier transform. Although it is still a linear transform, the fast Fourier transform algorithm is not suitable anymore. This new feature may severely harm the performance of the new algorithm.

4.4.2 Simplification of the Model.

As all the physical problems, a complex model is closer to reality, but at same time it is harder to solve. What a physicist do is to make some reasonable assumptions to simplify the model, and specifying the model into the mode where only the most concerned problems remained.

In the previous sections, the discussion includes the new pulse model and trace model in general case, and how the algorithm may be influenced by the new models. Retrieving the pulse information directly from the complex model is difficult. So the model will be simplified by some specific assumptions. The spatial profile, $f(x)$, is hard to retrieve from the algorithm. But in practice, GRENOUILLE measures the collimated beam in the far field, so firstly it assumes that the spatial profile of each frequency components is Gaussian with known width, which is convenient to measure. Furthermore, because prisms, gradings

mainly introduce the first order spatial chirp, which dominates the spatio-temporal effects on the GRENOUILLE trace, it is of the greatest interest of researchers. As a result, secondly it assumes only the first order spatial chirp presents in the pulses.

With these assumptions, the pulse field is simplified as:

$$E(x,\omega) = E(\omega)\exp\left[-\frac{(x-\zeta\omega)^2}{w^2}\right]\exp\left(-\mathrm{i}k\beta\omega x\right) \tag{37}$$

The GRENOUILLE trace is then,

$$T_{\mathrm{GREN},\zeta}(x,\omega) = \exp\left(-\frac{4x^2}{w^2}\right)\left|E_{\mathrm{sig},\zeta}(x,\omega)\right|^2 \tag{38}$$

where,

$$E_{\mathrm{sig},\zeta}(x,\omega) = \int \left\{ \begin{array}{l} E(\omega')\,E(\omega-\omega')\exp\left[-\mathrm{i}\omega'\left(\frac{2\theta x}{c}-2k\beta L\theta\right)\right] \\ \times\exp\left\{-\frac{1}{w^2}\left[\zeta^2\left(\omega^2+2\omega'^2-2\omega\omega'\right)-2x\zeta\omega+2L\theta\zeta\left(2\omega'-\omega\right)\right]\right\} \end{array} \right\} \mathrm{d}\omega'$$

The difference between $T_{\mathrm{GREN},\zeta}(x,\omega)$ and an ideal trace $\left|E_{\mathrm{sig},\zeta}(x,\omega)\right|^2$ is the spatial exponential term $\exp\left(-\frac{4x^2}{w^2}\right)$, which may be factored out in data processing. The following discussion will be focused on how to retrieve the pulse information from the trace, $\left|E_{\mathrm{sig},\zeta}(x,\omega)\right|^2$.

One important observation of the field, $E_{\mathrm{sig},\zeta}(x,\omega)$, is by factoring out the term $\exp\left(-\frac{2x\zeta\omega}{w^2}\right)$ the remaining integral still is a Fourier transform. With this observation, it is possible to use fast Fourier transform in the new algorithm to speed up the program.

By defining,

$$S_\zeta(\omega,\omega') = \exp\left\{-\frac{1}{w^2}\left[\zeta^2\left(\omega^2+2\omega'^2-2\omega\omega'\right)+2L\theta\zeta\left(2\omega'-\omega\right)\right]\right\} \tag{39}$$

the trace can be rewritten into,

$$E_{\mathrm{sig},\zeta}(x,\omega) = \exp\left(-\frac{2x\zeta\omega}{w^2}\right)\int E(\omega')\,E(\omega-\omega')\,S_\zeta(\omega,\omega')\exp\left[-\mathrm{i}\omega'\left(\frac{2\theta x}{c}-2k\beta L\theta\right)\right]\mathrm{d}\omega' \tag{40}$$

From Eq.40, in the frequency domain the GRENOUILLE field has an extra term $S_\zeta(\omega, \omega')$, which is introduced by the spatial chirp. So in the new algorithm, we will focus on the effect introduced by the term $S_\zeta(\omega, \omega')$.

With this simplification, we have reduced the unknown variable from $f(x), \zeta_n, \beta$ to ζ_1, β, and maintained Fourier transform relation between GRENOUILLE field and some intermediate state.

4.4.3 Algorithm Design

With the simplification above, by factoring out the term $\exp\left(-\frac{2x\zeta\omega}{w^2}\right)$, the only differences between the new model and the old one are the extra term $S_\zeta(\omega, \omega')$ in frequency domain, and two extra variables, ζ, β.

So how to apply the iterative-Fourier-transform algorithm in the new situation and how to do minimization on new variables are two questions need to be answered. The reason for maintaining the iterative-Fourier-transform algorithm is that it is prove to be the most efficient in the FROG pulse retrieval. Fortunately, after simplification it becomes easy by introducing an intermediate state, which is the ideal field without $\exp\left(-\frac{2x\zeta\omega}{w^2}\right)$.

For the minimization of new variables ζ, β, there are two choices. First, treat ζ, β the same as other variables in the temporal field $E(t)$ and minimize $E(t), \zeta, \beta$ all together. Second, hold ζ, β as constant first, minimizing on $E(t)$ only, and then keep the improved $E(t)$ as constant, minimizing on ζ, β.

To make this decision, we need to take a closer look on the FROG minimization procedure. As discussed in chapter 1, minimization in FROG algorithm has a very attractive feature: along any chosen minimization direction, the objective function is a polynomial of degree four. Therefore the minimization on determined direction can be done in one step. If go with first choice, this nice feature is no longer applicable, the performance of new algorithm will reduce dramatically. So it has to minimize the $E(t)$ and ζ, β separately.

With all these considerations, a new algorithm is designed as in Fig.26.

As shown in Fig. 26, the new algorithm works in following way,

Step 1, Preprocessing the measured trace by factoring out $\exp\left(-\frac{4x^2}{w^2}\right)$, to get $|E_{sig,\zeta}(x, \omega)|^2$.

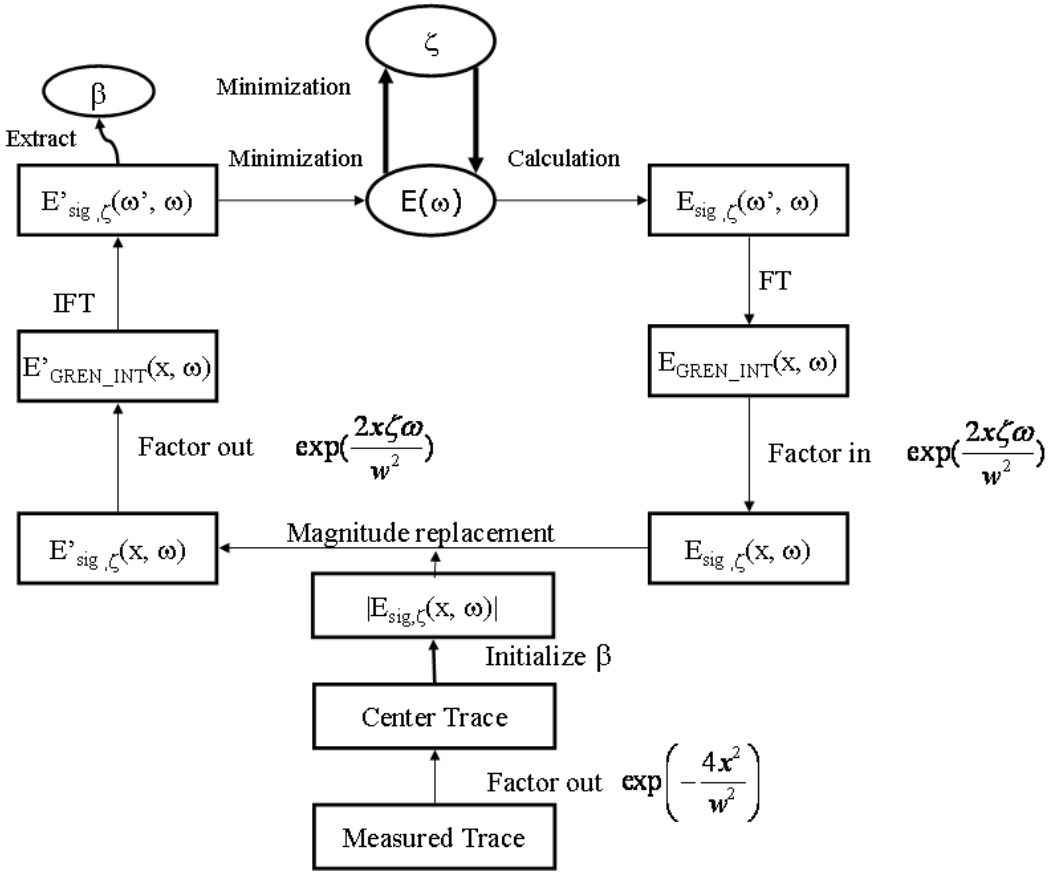

Figure 26: Schematic of the new FROG algorithm

Step 2, Centering the trace, $|E_{sig,\zeta}(x,\omega)|^2$, and estimating the base value of β

Step 3, Guessing the initial values of $E(t), \zeta$

Step 4, Calculating $E_{\mathrm{sig},\zeta}(\omega',\omega) = E(\omega')\,E(\omega-\omega')\,S_\zeta(\omega,\omega')$

Step 5, Fourier transforming $E_{\mathrm{sig},\zeta}(\omega',\omega)$ to the intermediate state $E_{GREN_INT}(x,\omega)$

Step 6, Multiplying $E_{GREN_INT}(x,\omega)$ by $\exp\left(-\frac{2x\zeta\omega}{w^2}\right)$ to get the GRENOUILLE field $E_{\mathrm{sig},\zeta}(x,\omega)$.

Step 7, Replacing the amplitude of $E_{\mathrm{sig},\zeta}(x,\omega)$ by $|E_{sig,\zeta}(x,\omega)|^2$, to get an improved $E'_{\mathrm{sig},\zeta}(x,\omega)$.

Step 8, Factoring out $\exp\left(-\frac{2x\zeta\omega}{w^2}\right)$ to get an improved intermediate state, $E'_{GREN_INT}(x,\omega)$.

Step 9, Inverse Fourier transforming $E'_{GREN_INT}(x,\omega)$ back to the frequency domain, $E'_{\mathrm{sig},\zeta}(\omega',\omega)$.

Step 10, Extracting asymmetric phase, get value of β at this iteration.

Step 11, Holding ζ, β as constant, minimizing on $E(t)$ to get a better guess of temporal field.

Step 12, Holding new $E(t)$ as constant, minimizing on ζ.

Step 13, Calculating the termination condition, if condition satisfied, the algorithm return, else go back to step 4 and continue.

4.4.4 Minimization of $E(t)$

As discussed in Chapter 1, the most important step in the FROG pulse retrieval is to apply the mathematical constrain to find out new $E(t)$ for the next iteration, which is the step 11 in the new algorithm. The new objective function is,

$$Z_\zeta = \sum_{i,j=1}^{N} \left| E(\omega'_i)\,E(\omega_j-\omega'_i)\,S_\zeta(\omega_j,\omega'_i) - E'_{sig,\zeta}(\omega_j,\omega'_i) \right|^2 \tag{41}$$

where $E'_{sig,\zeta}(\omega_j,\omega'_i)$ is the improved field from step 8.

$S_\zeta(\omega_j,\omega'_i,)$ is the new term introduced by the spatial chirp.

ζ is the spatial chirp parameter, in this step we just treat it as constant.

As shown in Appendix A, for this new multidimensional objective function, the algorithms for its minimization direction and its line minimization are required.

4.4.4.1 One Dimensional Minimization Procedure

Because the temporal field and the spatio-temporal parameters are minimized separately, in step 11 ζ and β are treated as constants. Under this condition, the objective function still holds the desirable property of being a polynomial along any direction. So the line minimization procedure in the earlier FROG algorithm can still work for the new objective function. The only thing changed is polynomial coefficients have some modification under the new objective function. New coefficient for line minimization is:

$$C_0 = \sum_{i,j=1}^{N} \left| E_{in}(\omega_i') E_{in}(\omega_j - \omega_i') S_\zeta(\omega_j, \omega_i') - E'_{sig,\zeta}(\omega_j, \omega_i') \right|^2$$

$$C_1 = \sum_{i,j=1}^{N} 2\mathrm{Re} \left\{ \begin{array}{l} \left[E_{in}(\omega_i') E_{in}(\omega_j - \omega_i') S_\zeta(\omega_j, \omega_i') - E'_{sig,\zeta}(\omega_j, \omega_i') \right]^* \\ \times \left[dE(\omega_i) E_{in}(\omega_j - \omega_i') + E_{in}(\omega_i') dE(\omega_j - \omega_i') \right] S_\zeta(\omega_j, \omega_i') \end{array} \right\}$$

$$C_2 = \sum_{i,j=1}^{N} \left\{ \begin{array}{l} \left| dE(\omega_i) E_{in}(\omega_j - \omega_i') + E_{in}(\omega_i') dE(\omega_j - \omega_i') \right|^2 \left| S_\zeta(\omega_j, \omega_i') \right|^2 \\ +2\mathrm{Re} \left\{ \begin{array}{l} \left[E_{in}(\omega_i') E_{in}(\omega_j - \omega_i') S_\zeta(\omega_j, \omega_i') - E'_{sig,\zeta}(\omega_j, \omega_i') \right]^* \\ \times dE(\omega_i') dE(\omega_j - \omega_i') S_\zeta(\omega_j, \omega_i') \end{array} \right\} \end{array} \right\}$$

$$C_3 = \sum_{i,j=1}^{N} 2\mathrm{Re} \left\{ \begin{array}{l} \left[dE(\omega_i) E_{in}(\omega_j - \omega_i') + E_{in}(\omega_i') dE(\omega_j - \omega_i') \right] \\ \times \left[dE(\omega_i') dE(\omega_j - \omega_i') \right]^* \left| S_\zeta(\omega_j, \omega_i') \right|^2 \end{array} \right\}$$

$$C_4 = \sum_{i,j=1}^{N} \left| dE(\omega_i') dE(\omega_j - \omega_i') \right|^2 \left| S_\zeta(\omega_j, \omega_i') \right|^2$$

with the calculation of new polynomial coefficients, the same procedure as in original algorithm can be followed to calculate the global minimum of the line directly.

4.4.4.2 Minimization Direction

As in the standard FROG algorithm, it first tries to use *steepest descent* in the new algorithm to determine the minimization direction. The gradient of the new objective function is calculated as,

$$\begin{array}{l} g(\omega_m) = \frac{2\partial Z}{\partial E^*(\omega_m)} \\ = \sum_{j=1}^{N} 2 \left\{ \begin{array}{l} \left| E(\omega_j - \omega_m') S_\zeta(\omega_j, \omega_m') \right|^2 E(\omega_m') \\ - \left[E(\omega_j - \omega_m') S_\zeta(\omega_j, \omega_m') \right]^* E'_{sig,\zeta}(\omega_j, \omega_m') \\ + \left| E(\omega_j - \omega_m') S_\zeta(\omega_j, \omega_j - \omega_m') \right|^2 E(\omega_m') \\ - \left[E(\omega_j - \omega_m') S_\zeta(\omega_j, \omega_j - \omega_m') \right]^* E'_{sig,\zeta}(\omega_j, \omega_j - \omega_m') \end{array} \right\} \end{array} \quad (42)$$

But during the coding for the new algorithm, we found that using negative gradient as the minimization direction, in most case, the algorithm don't converge at all. The reason for failure is the new term $S_\zeta(\omega, \omega')$ distorted the solution space, then the gradient no longer point to minimum direction after a short movement. So a minimization direction which can point to the minimum more accurately is needed. As discussed in Appendix A, *Newton's* method can determine a minimization direction better than *steepest descent*. To implement *Newton's* method, the second order partial derivatives, or Hessian, of Z_ζ, needs to be computed. From the discussion in Appendix B, the Hessian of Z_ζ is in the form of,

$$H = \begin{bmatrix} H^{RR} & H^{RI} \\ H^{IR} & H^{II} \end{bmatrix}$$

$H^{RR}, H^{RI}, H^{IR}, H^{II}$ are four sub-matrixes in H. If define,

$$T_{mn} = \begin{cases} n = m, & \left\{ \begin{array}{l} \sum\limits_{j=1, j-m\neq n}^{N} \left|E(\omega_j - \omega'_n)\right|^2 \left[\left|S_\zeta(\omega_j, \omega'_n)\right|^2 + \left|S_\zeta(\omega_j, \omega_j - \omega'_n)\right|^2\right] \\ +4\left|E(\omega'_n) S_\zeta(\omega_{2n}, \omega'_n)\right|^2 \end{array} \right\} \\ n \neq m, & E(\omega'_n)^* E(\omega'_m) \left[\left|S_\zeta(\omega_{m+n}, \omega'_m)\right|^2 + \left|S_\zeta(\omega_{m+n}, \omega'_n)\right|^2\right] \end{cases} \tag{43}$$

$$F_{mn} = \begin{cases} n = m, & 2S_\zeta(\omega_j, \omega'_n)^* \left[E(\omega'_n)^2 S_\zeta(\omega_{2n}, \omega'_n) - E'_{sig,\zeta}(\omega_{2n}, \omega'_n)\right] \\ n \neq m, & \left\{ \begin{array}{l} S_\zeta(\omega_{m+n}, \omega'_m)^* \\ \times \left[E(\omega'_m) E(\omega_n) S_\zeta(\omega_{m+n}, \omega'_m) - E'_{sig,\zeta}(\omega_{m+n}, \omega'_m)\right] \\ +S_\zeta(\omega_{m+n}, \omega'_n)^* \\ \times \left[E(\omega'_m) E(\omega_n) S_\zeta(\omega_{m+n}, \omega'_n) - E'_{sig,\zeta}(\omega_{m+n}, \omega'_n)\right] \end{array} \right\} \end{cases} \tag{44}$$

Then

$$
\begin{aligned}
H^{RR} &= 2\mathrm{Re}\left\{F+T\right\} \\
H^{RI} &= 2\mathrm{Re}\left\{-iF+iT\right\} \\
H^{IR} &= 2\mathrm{Re}\left\{-iF-iT\right\} \\
H^{II} &= 2\mathrm{Re}\left\{-F+T\right\}
\end{aligned}
\tag{45}
$$

With the calculation of H and gradient, *Newton's* method can be implemented as,

$$
\vec{dE}\left(\omega'\right) = -H_0^{-1}\cdot\vec{g}_0 \tag{46}
$$

where

H_0 are Hessian matrix as calculated during current iteration.

$\vec{g}_0$ is a vector with length 2N, the first half of it is the real part of the complex gradient vector. The second half of it is the image part of the complex gradient vector.

$\vec{dE}\left(\omega'\right)$ is the minimization direction, for next minimization step.

Now we completed the translation from *steepest descent* to *Newton's* method.

Practise coding proves that using *Newton's* method the algorithm can perfectly converge under the complex pulse and distortions.

4.4.5 Problems in Minimization of Spatio-Temporal Parameter,ζ.

Now move on to step 12 in the new algorithm. With the first look it is just a one dimensional minimization problem, with objective function,

$$
G(\zeta) = \sum \left| I_{GREN}\left(E\left(\omega\right),\zeta\right) - I_{data}\left(x,\omega\right)\right|^2 \tag{47}
$$

But with a closer check, it is a more complicated problem. Because in each iteration the pulse temporal field, $E^n(\omega)$, is usually quite different from the true field $E(\omega)$, the one dimensional function in each iteration, $G^n(\zeta)$, may have big discrepancy with $G(\zeta)$.

As shown in Fig. 27, doing regular minimization on $G^n(\zeta)$ may guide value of ζ away from the real minimum. In the coding practise, it was found this divergence was big enough to screw up the whole program.

Fortunately, an important observation is shown in coding practise: If ,

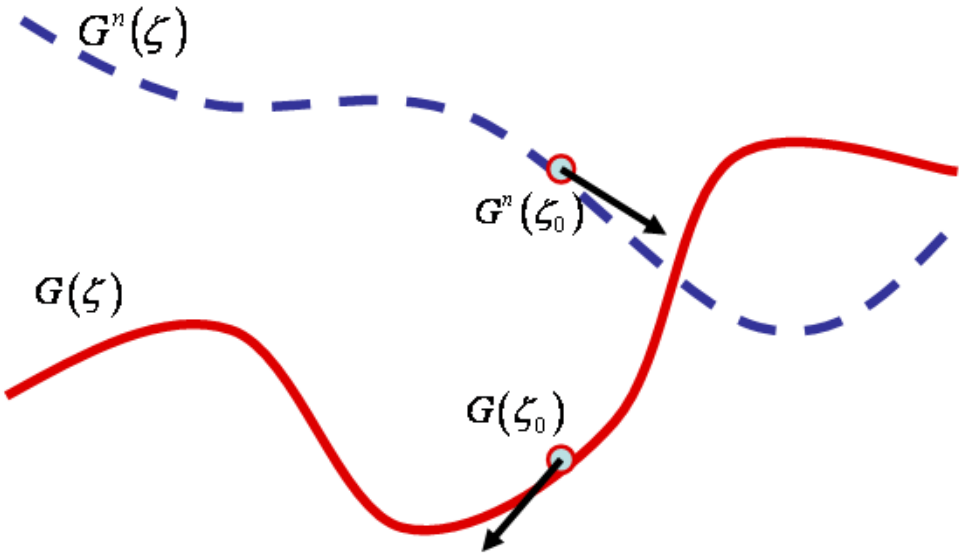

Figure 27: Red line shows the topology of $G(\zeta)$, blue dash line shows the topology of $G^n(\zeta)$.

$$\zeta_1 - \zeta_{real} < \zeta_2 - \zeta_{real} \tag{48}$$

then after minimization on step 9,

$$G(\zeta_1) < G(\zeta_2) \tag{49}$$

So the minimization procedure in step 9 can be treated as a function evaluation of $G(\zeta)$. Now the minimization of ζ turns into a one dimensional minimization problem with only function evaluation. Brent's method (parabolic interpolation) [49] is very efficient in minimizing the function with only evaluation. A modified parabolic interpolation is implemented in the code. Because $E(\omega)$ is improved in every iteration, the evaluation of $G(\zeta)$ with same ζ may be different in different iterations. The Brent's method is modified by re-evaluate the boundary points before the interpolation.

4.4.6 Retrieve Angular Dispersion, β

An intuitive understanding of the effect of the pulse front tilt on a GRENOUILLIE trace is that it shifts the trace off center on delay. Although it is not a rigorous description of the effect, but it is a good approximation of the value of β. In the code, it deliberates shifting

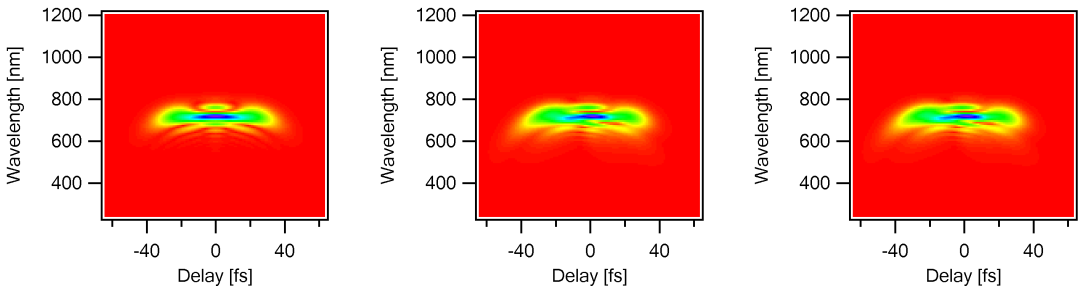

Figure 28: Left: GRENOUILLE trace of a spatio-temporal-distortion-free pulse. Middle: GRENOUILLE trace of the same pulse in the presence of spatial chirp (input spatial chirp: $dx/d\omega = 7.654321 \times 10^6 nmfs$). Right: Reconstructed GRENOUILLE trace using the algorithm described in the text, with the trace in the middle as the input. (retrieved spatial chirp $dx/d\omega = 7.654327 \times 10^6 nmfs$.)

the center of the mass of the trace back to the center of the trace, and uses the amount of shift to calculate the base value of the pulse front tilt parameter, β, as shown in step 2 of the algorithm. This base value is denoted as β_0. Final value of β is β_0 plus the fractional β retrieved in rest part of the algorithm.

There exist a subtlety introduced by centering the trace (separating β_0 from β). When factor in or out term $\exp\left(-\frac{2x\zeta\omega}{w^2}\right)$ in step 6 or 8, the original coordinate x is used to calculate the term, instead of the x' after shift.

To locate the value of β more accurately, it was found that $\exp\left[\mathrm{i}\omega'\left(2k\beta L\theta\right)\right]$ is the only term which introduces a constant gradient phase to the field of $E_{sig,\zeta}\left(\omega',\omega\right)$. By knowing this, the asymmetric phase term can be extracted from $E_{sig,\zeta}\left(\omega',\omega\right)$ in step 10 to estimate the fractional β in every iterations.

4.5 Tests of code

To test the performance of the new retrieval algorithm, it's theoretically generated a GRENOUILLE trace of a fairly complicated pulse under the spatial chirp distortion, as shown in Figs. 28 and 29. The distortion to the GRENOUILLE trace was quite severe. With the new algorithm, it's able to retrieve both the temporal pulse form and the spatial chirp value very accurately, which corresponded to a reconstructed trace in perfect agreement with the input distorted trace.

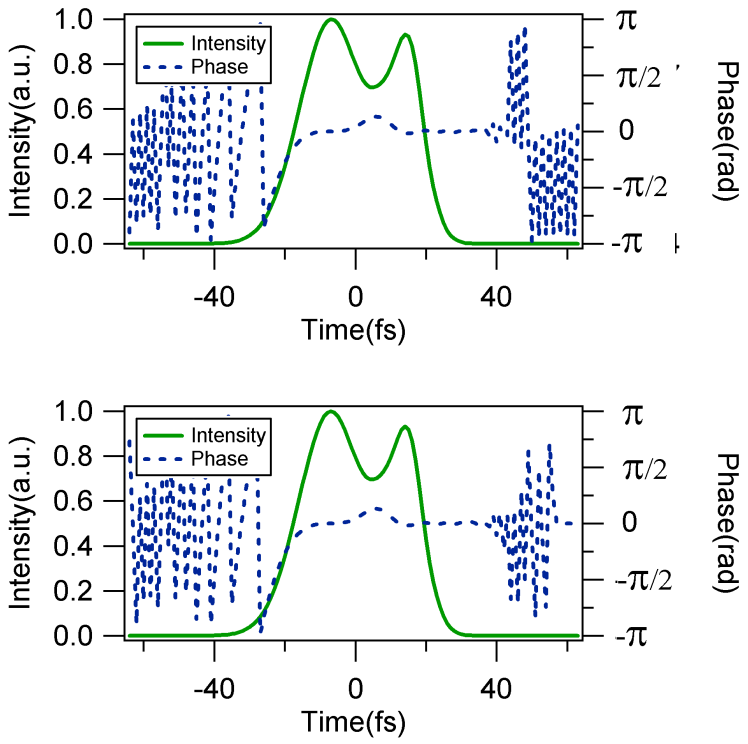

Figure 29: Simulated (upper) and retrieved (lower) electric field of the pulse that is used to generate traces in Fig. 28.

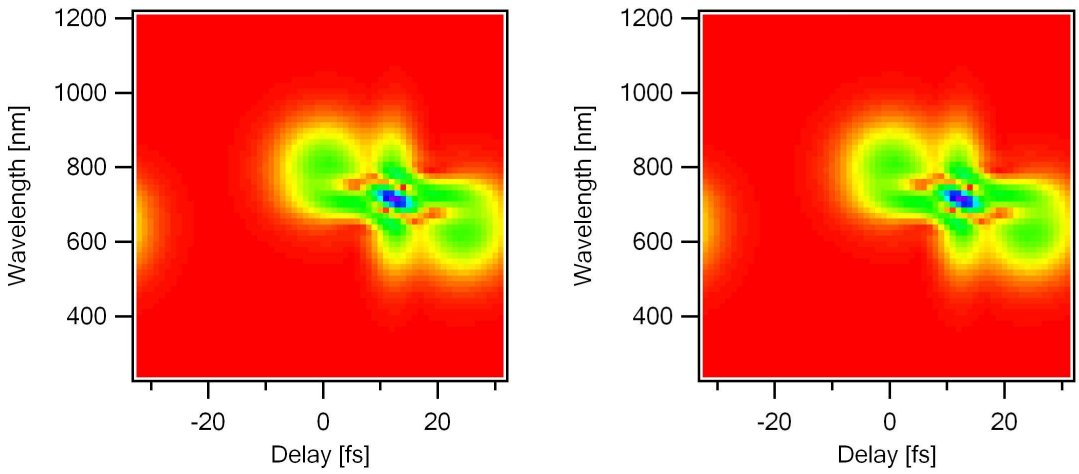

Figure 30: Left: GRENOUILLE trace in the presence of spatial chirp and angular dispersion (input spatial chirp: $dx/d\omega = 6.0 \times 10^6 nmfs$, input angular dispersion $beta = 1.9940 \times 10^{-5} fs$). Right: Reconstructed GRENOUILLE trace, with the trace in the left as the input. (retrieved spatial chirp $dx/d\omega = 6.0078 \times 10^6 nmfs$, retrieved angular dispersion $\beta = 2.0095 \times 10^{-5} fs$).

To test the overall performance of the new code, both spatial chirp and angular dispersion were added into test pulse. It was found the algorithm can still accurately find the value of the spatial chirp parameter. In retrieval of the parameter of angular dispersion, we have an error about $0.155 \times 10^6 fs$, which indicates about 1/10 pixels shift of the trace on delay in the test trace.

Overall, we achieved accurate retrieval of both the pulse profile and the spatio-temporal parameter from the distorted complicated GRENOUILLE trace.

4.6 Conclusions

In conclusion, a new ultrashort pulse electric field retrieval algorithm is developed, which retrieves not only the temporal evolution of the pulse, but also spatio-temporal distortion parameters of the input beam from the distorted GRENOUILLE trace. For the pulses with only spatial chirp, the pulse characteristic in both temporal and spatial domain can be perfectly retrieved. For the pulses with both spatial chirp and angular dispersion, the code can still get reasonably accurate retrieval, but the optimization of the angular dispersion parameter could be improved.

CHAPTER V

SPATIAL EFFECT ON GRENOUILLE

5.1 Introduction

Variations in the spatial profile of an ultrashort pulse are generally neglected when measuring its temporal profile. This assumption is not always justified even when the beam profile is an ideal Gaussian.

In *multi-shot* measurements of ultrashort pulses, the delay is typically scanned by moving a mirror,[50, 38, 9] and, as long as spatio-temporal distortions are absent (that is, the pulses' spatial and temporal field dependences separate), the space dependence of the field factors out of the expression for the pulse autocorrelation and FROG [53] trace. As a result, multi-shot autocorrelation and FROG measurements are essentially immune to poor spatial mode quality. However, multi-shot methods require scanning the delay, which can be slow and laborious. Multi-shot methods also suffer from geometrical distortions due to varying delay across or along the nonlinear medium. And they cannot measure spatio-temporal distortions.

In *single-shot* autocorrelation and FROG measurements, however, the delay is mapped onto transverse position by crossing the replicas of the pulse at a relatively large angle (see Fig.38).[57, 11, 52, 5, 14, 25, 32, 33, 36, 35, 40, 41] This class of methods is experimentally simpler than its multi-shot cousins, and they are typically immune to geometrical smearing effects. Also, they can indicate spatio-temporal distortions; single-shot FROG or GRENOUILLE accurately yield the pulse spatial chirp and pulse-front tilt. However, because the spatial coordinate is now used to obtain temporal information, it is necessary to assume nearly constant beam intensity vs. the transverse coordinate. It is well-known that this assumption is necessary, and, as a result, all such single-shot methods require essentially constant beam spatial profiles, which is usually achieved by using large Gaussian beam profiles. In GRENOUILLE measurements, especially of relatively long pulses (which

result in a relatively broad trace), a complex pulse spatial profile can distort the trace and the resulting retrieved pulse temporal profile. Indeed, even an ideal Gaussian beam, if not sufficiently expanded, can result in a measured trace and pulse that are too short in time.

GRENOUILLE is sensitive to the input beam spatial profile in another manner. It utilizes the signal beam angular deviation in the other direction (say, y) in conjunction with a thick crystal's small phase-matching bandwidth to spectrally resolve the signal pulse. Variations in the nonlinear-optical signal intensity vs. k_θ yield spectral structure in the trace and hence also indicate spectral structure in the pulse. But variations in the input beam's intensity vs. angle at the crystal can also yield such signal variations. Thus, the input beam intensity dependence on k_θ is also important to take into account.

The purpose of this chapter is to include the effects of the beam spatial profile on FROG, GRENOUILLE, and related measurements. We will take into account both the beam intensity vs. x, which distorts the trace along the delay axis and its intensity vs.k_θ (i.e., angle) which distorts the trace along the frequency axis.

While the error introduced by the assumption of a constant beam profile is usually very small in GRENOUILLE measurements, especially for unamplified pulses, this error can become significant for amplified pulses, which usually have poorer spatial profiles. Fortunately, amplified pulses usually have larger beams, and an averaging over one transverse coordinate both work to reduce any such errors. Nevertheless, it is important to consider this effect, and better, to remove it.

FROG is a spectrally resolved autocorrelation (spectrogram) with a corresponding iterative phase-retrieval algorithm to retrieve the pulse intensity and phase. GRENOUILLE is a highly simplified version of FROG, in which a Fresnel biprism splits the pulse in two and recombines them in a second-harmonic-generation (SHG) crystal, automatically aligning the device and mapping delay onto transverse position. The SHG crystal in GRENOUILLE is thick, and so it spectrally resolves the second harmonic that it produces. It is known for its low cost, compact size, automatic alignment, and simple operation. Because it incorporates a camera for measuring the spectrogram, GRENOUILLE typically also is used to measure the spatial profile of the beam. As a result, it is relatively convenient to take advantage of

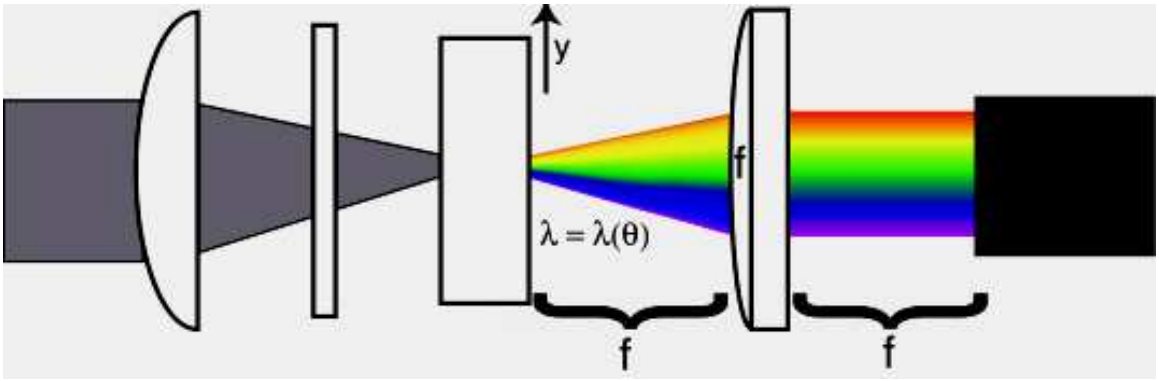

Figure 31: Sides view of GRENOUILLE

the spatial information to improve the temporal measurement.

In this work, we explore the effects of the spatial profile on the measured GRENOUILLE trace. We show that, in the absence of spatio-temporal distortions, the effect of the spatial profile on the measured GRENOUILLE trace simply an intensity mask. The mask can be calculated simply from the measured spatial profile of input beam(for one technique, it *is* spatial profile). Such distortions can be removed by simply dividing the measured trace by spatial mask.

Finally, because single-shot FROG and GRENOUILLE necessarily incorporate a camera for measuring the pulse spectrogram, they naturally also measure the spatial profile of the beam. As a result, it is relatively convenient to take advantage of the spatial information to improve the temporal measurement when necessary.

5.2 Spatial Manipulation in GRENOUILLE

In GRENOUILLE, an input beam is manipulated differently in two perpendicular dimensions, x and y. As shown in Fig. 31, in the y dimension, the beam focused by a cylindrical lens, then the SHG signal generated by the crystal is passed through a Fourier transform lens to reach detector.

As shown in Fig. 32, in the x dimension, two halves of the beam are crossed at the nonlinear crystal, then the SHG signal is imaged on the detector by a 2f imaging system.

As a result, the spatial profile of the beam will have different effects on the GRENOUILLE

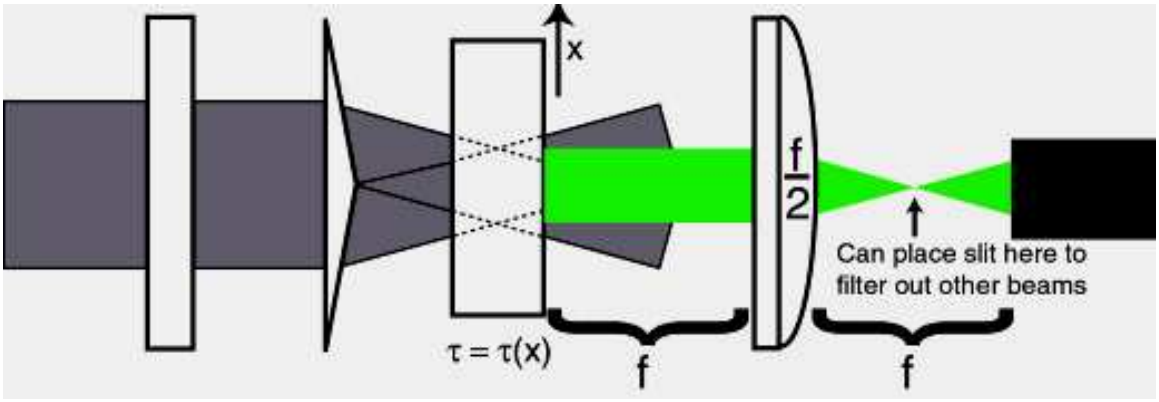

Figure 32: Top view of GRENOUILLE

trace in the two different dimensions. In coming sections, removing the effects in the two dimensions will be discussed respectively.

5.3 Spatial Profile Influence in y Dimension

In the y dimension, as shown in Fig. 33, the cylindrical lens (Lens 1) focuses the input beam onto the thick crystal. With this operation, the beam spatial profile $E_{in}(y)$ is converted into the angular profile $\tilde{E}_{in}(k_\theta)$. Because of small phase-matching bandwidth of the thick crystal, certain colors in SHG signal can only phase match on a specific output angle. Therefore the frequency of the SHG signal is resolved into different angles. We denote the output SHG signal field as $\tilde{E}_{out}(k'_\theta)$. Then the Fourier transform lens (Lens 2) will map the angular distribution of the SHG signal into the spatial distribution, $E_{out}(y')$, on the CCD camera.

With the description above, two lenses map the fields between the spatial and angular spaces, so the relation between $\tilde{E}_{in}(k_\theta)$ and $E_{out}(k'_\theta)$ can be assumed as $E_{in}(y) \propto \tilde{E}_{in}(k_\theta)$, similarly $\tilde{E}_{out}(k'_\theta)$ and $E_{out}(y')$. But the relation between $\tilde{E}_{in}(k_\theta)$ and $\tilde{E}_{out}(k'_\theta)$, involves complex SHG processes in the thick SHG crystal, therefore requires more detailed discussions.

Nonlinear process in GRENOUILLE pulse measurement is complex. The fundamental beam is input on the nonlinear crystal with a tight focus, therefore the fundamental beam has a great angular divergence. As a result, both the collinear and non-collinear phase

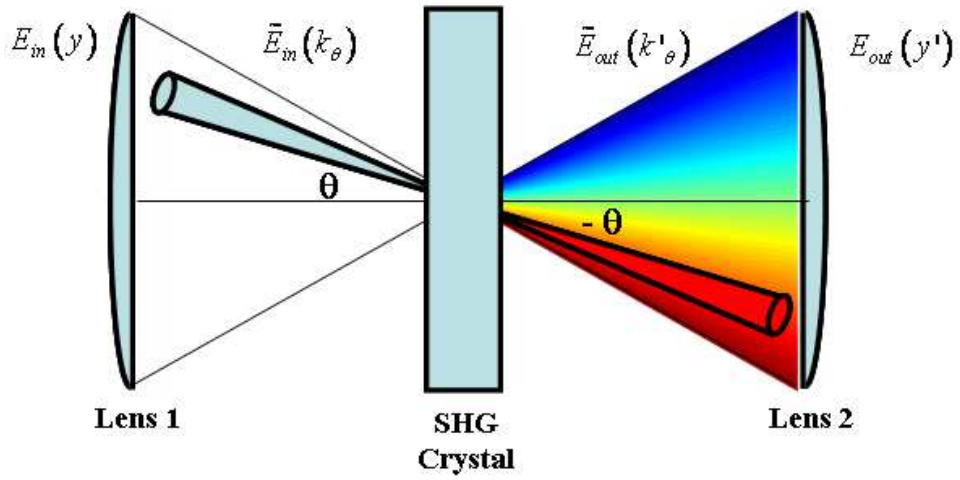

Figure 33: Field translation in y dimension.

matching could take place in the GRENOUILLE pulse measurement.

Another important feature of the GRENOUILLE technique is that the small phase-matching bandwidth of the thick crystal is utilized to resolve the frequency component of the SHG signal into different angles. According to the good agreements between the GRENOUILLE traces and the multi-shot FROG traces, an assumption is made in the following discussion: different colors in the SHG signal is perfectly resolved into different angles by the thick crystal in the GRENOUILLE.

As shown in Fig.33, in case of the collinear phase match, the fundamental beam on the "θ" direction will contribute to the SHG signal with the frequency ω on the "$-\theta$" direction.

Comparing collinear phase match and non-collinear phase match as in Figure 34, the SHG signal with the frequency ω generated by the non-collinear phase match will output with angles other than "$-\theta$". Therefore the contribution of non-collinear phase match to the frequency ω in the SHG signal is ignorable according to the assumption made above. There is another case of non-collinear process, which can generate the frequency on direction "$-\theta$" as shown in Fig.35.

This is the case where the phase match condition is not hold. As a result, the efficiency of the SHG process is low. The second harmonic generation efficiencies of the collinear and non-collinear process with different angles are compared in Fig.36.

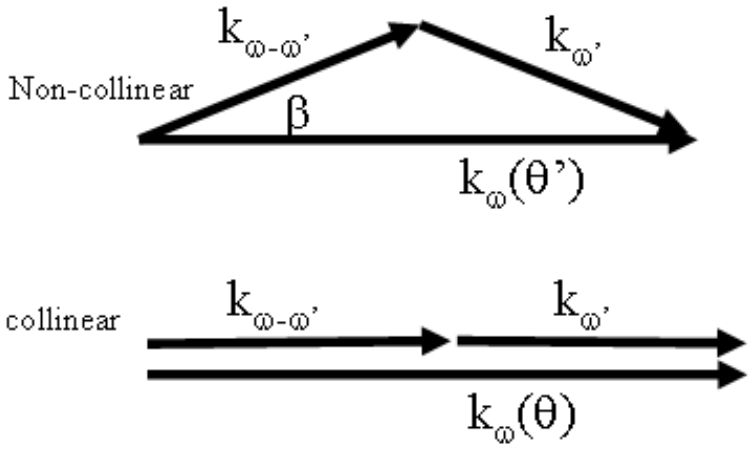

Figure 34: Upper: the non-collinear phase math with a non-collinear angle of β and output angle $-\theta'$; Lower: the collinear phase match with output angle $-\theta$.

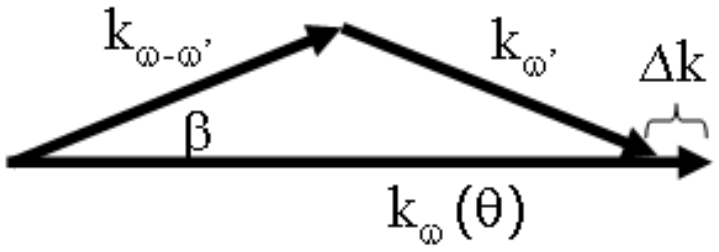

Figure 35: the non-collinear SHG process without phase match.

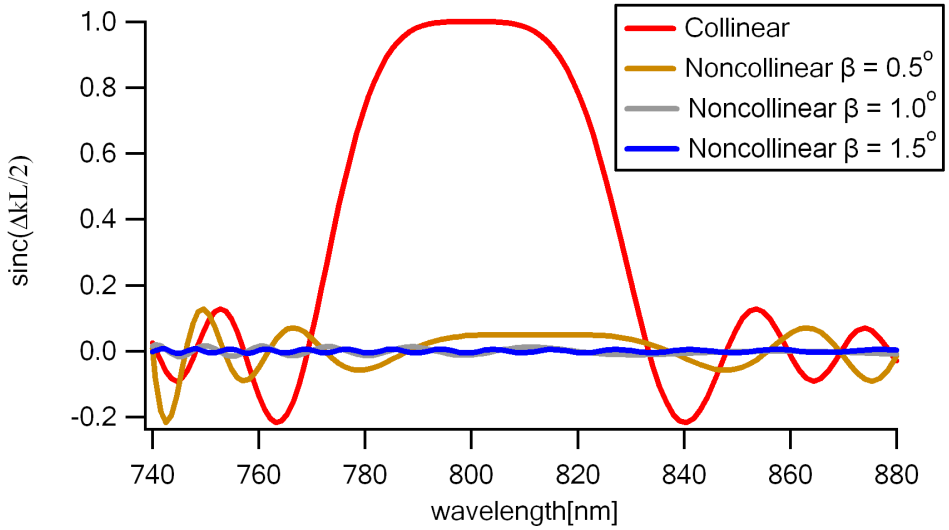

Figure 36: SHG efficiency comparison in the collinear and non-collinear process.

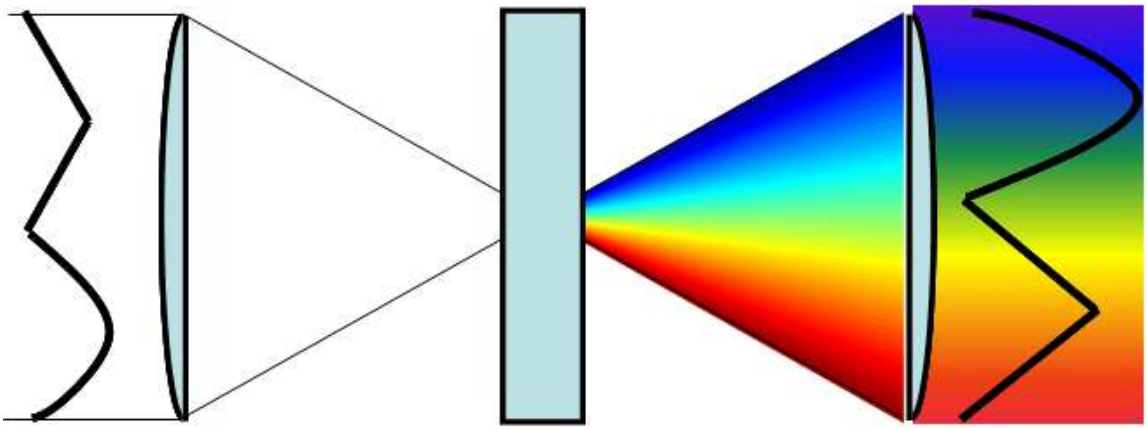

Figure 37: Intensity Mask introduced by spatial profile on the Y dimension

As shown in Fig. 36, the efficiencies reduced dramatically when the non-collinear angle has a tiny increase. So in practice, the collinear phase match process dominates in the nonlinear process in the GRENOUILLE pulse measurement. As a result, the angular distribution of the fundamental beam $\tilde{E}_{in}(k_\theta)$ and the angular distribution of the SHG signal $\tilde{E}_{out}(k'_\theta)$ have a simple relation as: $I_{out}(k_{-\theta}) \propto I_{in}^2(k_\theta) I_{SHG}(\omega_{-\theta})$.

By putting all the relations together, the input beam spatial profile $I_{in}(y)$ can be related to the output spatial profile $I_{out}(y')$ as $I_{out}(y') \propto I_{in}^2(-y) I_{SHG}(y')$.

In conclusion, the influence of the input beam spatial profile on the output GRENOUILLE trace in y dimension is mainly an intensity mask, which is the square of the input pulse intensity in y with a flip, as shown in Fig.37. Although this result is based on the assumption of the perfect crystal, it is still a good approximation to real cases as discussed above. Therefore it is appropriate to apply this conclusion to the real measured traces.

5.4 Spatial Profile Influence in x Dimension

In x dimension, GRENOUILLE involves crossing two halves of the beam at the nonlinear crystal to generate a second harmonic signal. Then the second harmonic signal is imaged on the CCD camera.

Imaging process in x dimension will not influence the profile of the trace, so the discussion

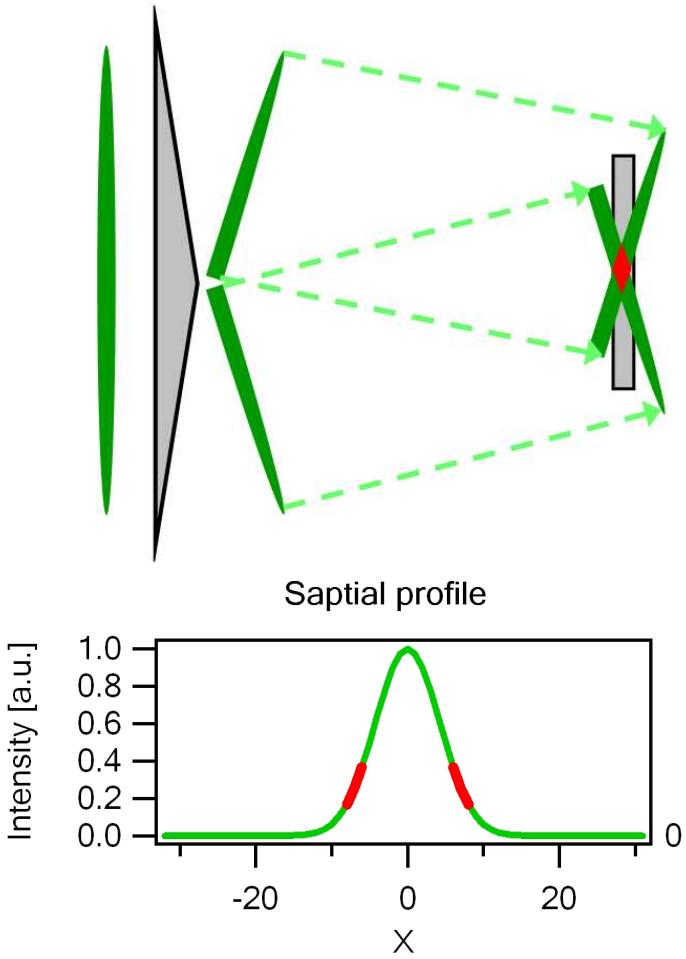

Figure 38: Above: shows two halves of the beam crossed by the biprism, and the overlapping zone on nonlinear crystal; Bottom: show the active spatial portion of the pulse, which takes part in the generation of second harmonic signal.

will be focused on the beam crossing effects. As shown in Fig.38, typically only a portion of each half beam (active zone) is engaged in signal generation.

The effect caused by the spatial profile of the pulse on the GRENOUILLE trace in x dimension is simply an intensity mask. The overall mask on the trace is a multiplication of the intensity of the left half beam and the intensity of the right half beam in the active zone, as shown in Fig. 39.

Fig. 39 also indicates that for a short pulse if its spatial profile is symmetric, and the active zones on each half beam happen to be symmetrically placed on the profile, the overall mask is close to the constant, the effect of the spatial profile is ignorable. But there still

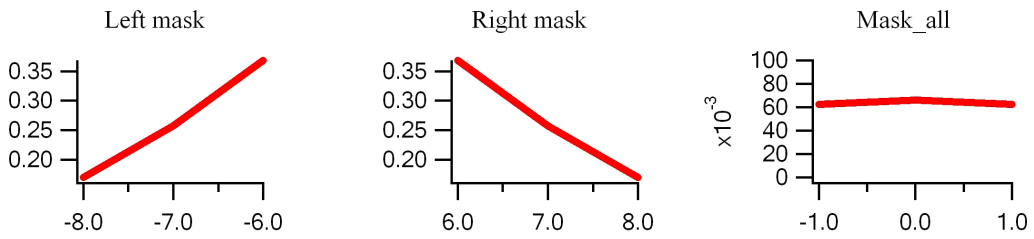

Figure 39: Left: linear intensity of the active zone on left half beam. Center: linear intensity of the active zone on right half beam. Right: constant over all intensity mask on the final trace.

are many cases that the overall mast cannot be neglected. For instance, when the pulse is long, then the active zone will spread over a big range of the spatial profile and no longer be approximated to a linear shape, the result mask will strongly depend on the topology of the spatial profile. In another case, if the spatial profile is not symmetric or the active zones are located on asymmetric places of the spatial profile (in case of a misaligned beam), the effects from left side and right side beam cannot cancel each other, the overall mask will modify the trace dramatically.

5.4.1 Interpolation in x Dimension

As discussed before, in x dimension only a portion of the pulse spatial profile is involved in generating the spatial mask. if the CCD camera measuring the beam spatial profile has same resolution as the CCD camera measuring the GRENOUILLE trace, the size of spatial mask in x dimension will be smaller than that of the trace. But in order to factor out the spatial mask from the measured trace, a spatial mask with same size of the trace is required.

There are two ways to achieve this. First, a high resolution camera can be utilized to measure the spatial profile of the beam. Second, the spatial mask in x dimension can be numerically interpolated to increase its size as that of the trace. The first approach is not applicable, because it requires an addition camera which is inconvenient and expensive. Furthermore, because pulses measured by GRENOUILLE vary in length, it is hard to predetermine the resolution of the additional camera. The second approach can be applied to the measurement of pulses with any pulse length. But the drawback of interpolation is

the fine structure of the spatial profile will be lost in this approach. Will this harm our method? The answer is no, as long as the SHG signal is generated on high energy region of the beam.

Because the spatial intensity mask is multiplied to the ideal trace to generate distortions, and the measured trace is routinely normalized in numerical processing, therefore the actual mask on the trace is the normalized spatial mask, $I_{mask}/I_{mask-min}$. $I_{mask-min}$ is the minimum intensity in the mask. The value of $I_{mask-min}$ is determined by the values of the intensity in the active zones of the left and right beamlets. When fine structures present in the intensity mask, the mask can be represented as $\left(I_{mask-rough} + \Delta I_{mask-fine}\right)/I_{mask-min}$. If the fundamental beam is managed to overlap at the high intensity parts, the value of $I_{mask}(min)$ is high. The $\Delta I_{mask-fine}/I_{mask-min}$ is ignorable from the overall mask.

Therefore, losing fine structure in the intensity mask will only slightly influence the final mask. As a result, interpolation on x dimension to match up the size of the spatial mask and the trace is a practical approach.

5.5 Spatial Profile Influence in x & y Dimension

Combining the discussions in last two sections, an overall 2D spatial mask can be written as,

$$Spatial_{mask}\left(x,y\right) = f\left(x - L\theta, -y\right) f\left(x + L\theta, -y\right) \tag{50}$$

Where

$f\left(x,y\right)$ is the spatial profile of the input beam. L is the distance from the biprism to the crystal. θ is the crossing angle of the beam.

By measuring the spatial intensity profile, $f\left(x,y\right)$, of the input beam, which is very convenient in GRENOUILLE, the 2D spatial mask of the GRENOUILLE trace can be calculated from the formula above.

For instance, suppose an input beam spatial profile is measured as shown in Fig. 40.

The corresponding second harmonic active zones and the overall spatial mask are shown in Fig. 41.

Under this mask the GRENOUILLE trace will be distorted as shown in Fig. 42.

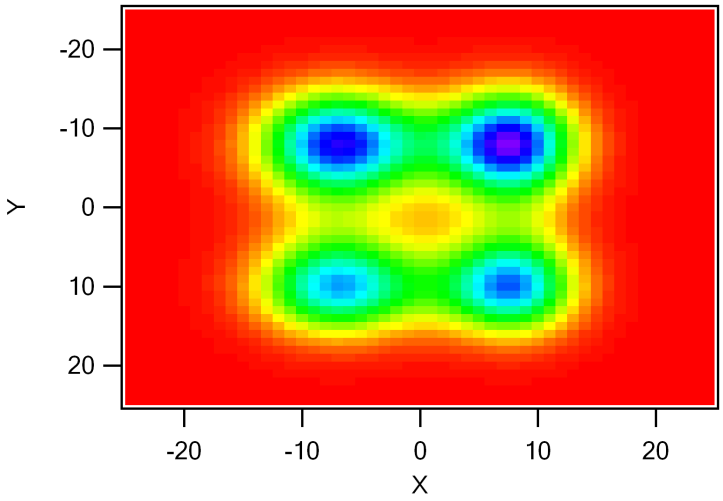

Figure 40: Spatial profile of input beam.

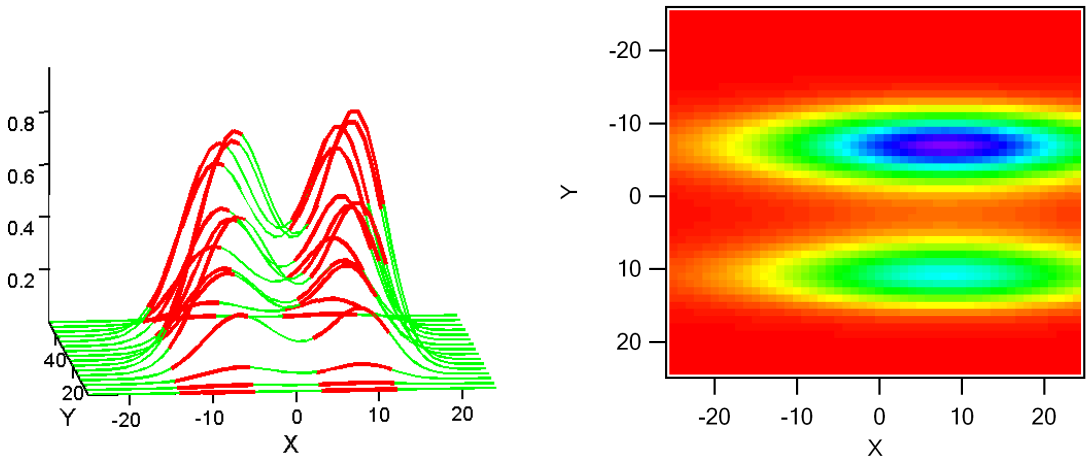

Figure 41: Left:active zone of the spatial mask in Fig.40;Right: Overall spatial mask

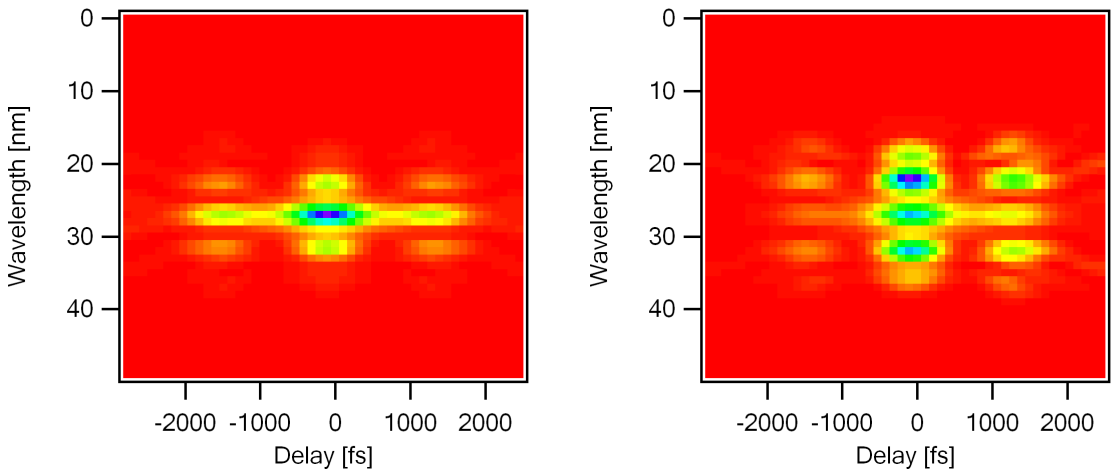

Figure 42: Left: the theoretical GRENOUILLE trace without spatial distortion, right: the measured GRENOUILLE trace under the spatial mask shown in Fig. 41

The simulated results show that the spatial distortions dramatically change the GRENOUILLE trace, therefore removing the spatial effect is a necessary and important step in processing a GRENOUILLE trace.

5.6 Conclusions

In this work, influence of the beam spatial profile on the GRENOUILLE trace is discussed. We concluded that the effects can be simply treated as an intensity mask. In y dimension, the intensity mask is simply the square of the input beam profile in y with a flip. In x dimension, the mask is the multiplication of the left and right intensity mask in the active zone. Therefore in x dimension, symmetry of the spatial profile, intensity of the pulse, width of the pulse in time domain, are all play roles in the final intensity mask. This spatial effect can be easily removed by dividing the spatial mask from the measured trace.

APPENDIX A

MULTIDIMENSIONAL OPTIMIZATION

Optimization is a very broad topic. It is no possible to cover every details of optimization in this discussion, so only a small portion of optimization which is related to the FROG algorithm is discussed to prepare readers for understanding of the works in this thesis.

The specific part of optimization problem involved in the FROG algorithm is the unconstrained multi-dimensional optimization with calculation of derivatives. In the rest part of this chapter, the one dimensional optimization will be discussed first, because almost all the multi-dimensional optimizations require a one dimensional optimization sub-algorithm. The scenario of the unconstrained multi-dimensional optimization is displayed to readers. Finally a general strategy for the multi-dimensional optimization is presented and how derivatives are used in multi-dimensional optimization is discussed.

A.1 One Dimensional Optimization

There are many algorithms for searching minima in one dimension. They can be divided into two major families, *with* or *without* the computation of derivatives. One dimension algorithms without computation of derivative, such as Golden Section Search,[31] Parabolic Interpolation,[10] are not of our interest. Discussion will focus on the one dimensional optimization family with the computation of derivatives.

Information of derivatives is very useful in determine the searching direction and the step length along the direction.

As shown in Fig.43, the negative sign of the first order derivative at point x_0, $g = \frac{df}{dx}\Big|_{x_0}$, tells us the minimization direction, the blue arrow. The magnitude of the first order derivative can not give us much useful information except for a rough estimation of the searching step length(first order derivative on the minima is zero, bigger magnitude should correspond to longer step length).

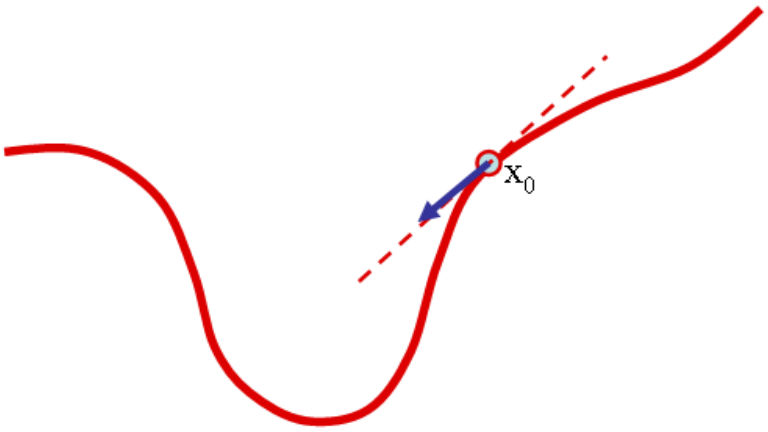

Figure 43: Minimum searching with computation of first order derivative. Dash line shows the first order derivative at point x_0. Blue arrow points to the negative sign direction of first order derivative, which is the minimization direction.

In general, the function is nicely parabolic near to the minimum. The function f can be expanded into a polynomial of degree two near the minimum.

$$f = c + bx + ax^2 + \cdots$$

where $a = \frac{d^2 f}{dx^2}\Big|_{x_0}$ is second order derivative of function on point x_0, $b = \frac{df}{dx}\Big|_{x_0}$ is first order derivative of function on point x_0. $c = f(x_0)$

The polynomial defined by a, b, c will match up with the function closely in the region near to the minimum. Then a single leap with length $-\frac{b}{2a}$, can be made from x_0 to the minimum, as shown in Fig.44

So combining the information of the first and the second order derivatives, both the searching direction and a relative accurate step length can be determined.

Imagining of computing higher order derivatives, such as third, fourth order, a more accurate estimation of the step length can be found. The drawbacks of computing higher order derivatives are the influence of high order derivative on step length is usually small, and the computation consumes time itself, furthermore the higher order derivatives are not always able to be computed. In general, people only compute the first and second order derivatives.

But there is still a special case need be considered about. When the function is a

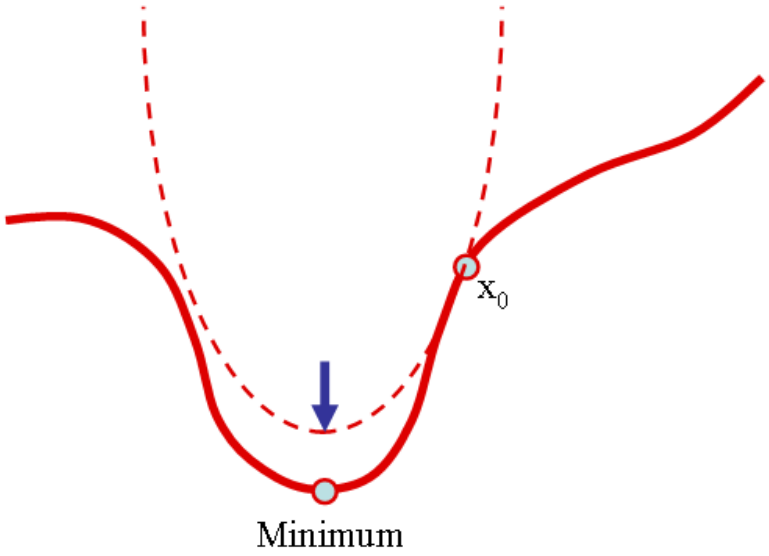

Figure 44: Minimum searching with computation of first and second order derivative. Dash line is the parabolic fitting line at x_0 with first and second derivative. Blue arrow shows the place for next leap in searching.

polynomial—only has finite orders of derivatives, by knowing the coefficient of the polynomial, the global minimum of the function can be easily calculated directly.

As shown in Fig.45, the extrema of the function are all located at the place where the first order derivative equal to zero. If the function is a polynomial of degree n, f_n, the first order derivative of f_n is a polynomial of degree n-1, f'_{n-1}. As shown in Fig., the extrema of f_n will locate at roots of f'_{n-1}. According to the *Fundamental Theorem of Algebra*, the number of roots of f'_{n-1} is n-1. By calculating all the roots of f'_{n-1}, and evaluating them in f_n, the point with minimum value of f_n is the minimum. This minimum is the global minimum of the polynomial. Now, the iterative minima searching procedure is reduced in to the roots calculation of f'_{n-1} and n-1 evaluations of f_n. In practise, only the unique and real roots need be evaluated, the number of evaluations may much less than n-1.

A.2 Multi-Dimensional Optimization Scenario

Multidimensional minimization is finding the minimum of a function of more than one independent variables. The mainstream strategy for the multidimensional minimization came form following scenario.

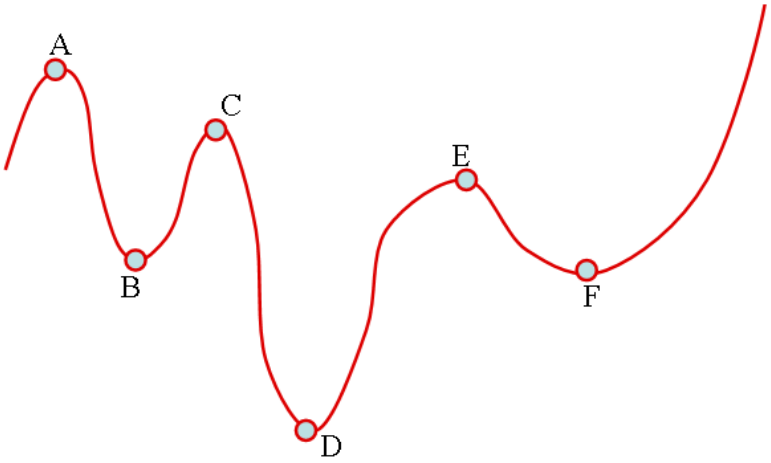

Figure 45: Extrema of a function in an interval.

Suppose a blind man is trying to find treasure in a hilly region. The only clue he knew about the treasure is it located at the lowest point of the region. Because the man is blind, he can not SEE where the treasures is. A simple strategy for him is starting from where he stood, choosing a downhill direction, moving along that direction until the latitude start to increase, then choosing another downhill direction and repeating the procedure above. This strategy can guarantee he always go to a lower place, if there is no local minimum in the region, he can always find the treasures finally.

This strategy is also applicable in the minimum searching in N-dimensional space. Searching can start from a random point $\mathbf{P}$ in N-dimensional space, proceed from there in some vector direction $\mathbf{n}$, then the multi-variable function f can be minimized along the direction $\mathbf{n}$ by a one dimensional minimization program as discussed in last section. Then repeating the procedure, the minimum in N-dimensional space can be reached after sequences of the line minimization. Under this strategy, different minimization methods will differ only by how they choose the next direction $\mathbf{n}$ at each stage.

Although this is not the only strategy in the multidimensional optimization—method like *simplex*[46] don't use one dimensional minimization at all, it is the most popular one used today. Especially when the derivatives of the function is computable, it is the most efficient strategy.

A.2.1 Minimization Direction in Multidimensional Optimization

As discussed in last section, every iteration of the multidimensional minimization consists two steps. First step is determining the minimization direction. Second step is minimizing along the chosen direction. The major different between different methods is their way of choosing the direction.

If the derivatives of the function is not able to be computed, the minimization direction must be guessed from experience like Direction Set(Powell's) method.[1] But this not the case of our interest, because the derivatives of the objective function of FROG algorithm are calculable.

If the first order partial derivative of the function can be calculated, then the minimization direction can be the negative gradient of the function,

$$\begin{aligned} \vec{n} &= -\vec{b} \\ b_i &= \frac{\partial f}{\partial x_i} \end{aligned} \tag{51}$$

The direction $-\vec{b}$ is the one in which the objective function decrease most rapidly, at least initially. Hence this method is called *steepest descent*.

If the second order derivative of the function can also be calculated, then alike in one dimension minimization, the multidimensional function can be expanded at x_0.

$$\begin{aligned} & f(x) = f(x_0) + \sum_i \frac{\partial f}{\partial x_i}(x_i - x_{0i}) + \frac{1}{2}\sum_{i,j} \frac{\partial^2 f}{\partial x_i \partial x_j}(x_i - x_{0i})(x_j - x_{0j}) + \cdots \\ & \approx c + b \cdot (x - x_0) + \frac{1}{2}(x - x_0) \cdot H \cdot (x - x_0) \end{aligned} \tag{52}$$

where

$c \equiv f(x_0)$ $b_i \equiv \frac{\partial f}{\partial x_i}\Big|_{x_0}$ $H_{ij} \equiv \frac{\partial^2 f}{\partial x_i \partial x_j}\Big|_{x_0}$

At the minimum of $f(x)$, the first order derivative is zero. Substituting this condition into Eq. 52,

$$0 = b + H \cdot (x - x_0) \tag{53}$$

By solving it,

$$x = x_0 - H^{-1} \cdot b \tag{54}$$

So the minimum x can be reached by one leap $-H^{-1} \cdot b$ from x_0. Same as in one dimensional minimization, both minimization direction and step length can be determined in multidimensional optimization, if the first and second order derivatives are calculated. This method is call Newton's method, it is much more efficient than steepest descent method. In common case, it could be 25,000 times more efficient than the steepest descent.[8]

A.3 Conclusion

The unconstrained multidimensional optimization mainly contains two steps in each iteration. First step is choosing the minimization direction, methods for this step could be Powell's method, steepest descent, Newton's method, depending on which order's derivatives is calculated. Second step is line minimization along the chosen direction, again the information of derivatives can be utilized in minimization, specifically if the function is a polynomial, the line minimization can be simplified into a direct calculation.

APPENDIX B

HESSIAN OF FROG OBJECTIVE FUNCTION

In the new FROG algorithm, the Hessian of objective function need be computed:

$$Z_\zeta = \sum_{i,j=1}^{N} \left| E\left(\omega_i'\right) E\left(\omega_j - \omega_i'\right) S\left(\omega_j, \omega_i', \zeta\right) - E'_{sig,\zeta}\left(\omega_j, \omega_i'\right) \right|^2$$

By definition, Hessian of a function f is:

$$H_{mn} = \frac{\partial^2 f}{\partial x_m \partial x_n}$$

where f is a function of N variables. x_m, x_n are any two independent variables in f.

In this case, Z_ζ is the function with 2N variables. The variables in Z_ζ is $E\left(\omega_i\right), i = 1, 2, \cdots N.$. Because for every $E\left(\omega_i\right)$, its real part and image part are two independent variables, Z_ζ has totally 2N independent variables. In order to clearly denote the variables in function Z_ζ, the vector x is defined as,

$$x_i = \begin{cases} 1 \le i \le N, & \mathrm{Re}\left\{E\left(\omega_i\right)\right\} \\ N+1 \le i \le 2N, & \mathrm{Im}\left\{E\left(\omega_{i-N}\right)\right\} \end{cases}$$

The the Hessian of Z_ζ is,

$$H_{mn} = \frac{\partial^2 Z_\zeta}{\partial x_m \partial x_n}, \{m, n = 1, 2, \cdots, 2N.\}$$

The Hessian of Z_ζ can be separated into four N by N sub-matrix as,

$$H = \begin{bmatrix} H^{RR} & H^{RI} \\ H^{IR} & H^{II} \end{bmatrix}$$

The superscript of the sub-matrixes represents the partial derivative are conducted on the real or the image part of the $E(\omega_i)$. The subscript is the index of the $E(\omega_i)$. For example,

$$H_{mn}^{RI} = \frac{\partial^2 Z_\zeta}{\partial \mathrm{Re}\left\{E\left(\omega_m\right)\right\} \partial \mathrm{Im}\left\{E\left(\omega_n\right)\right\}}, \{m, n = 1, 2, \cdots, N.\}$$

The later discussion shows that the value of four sub-matrixes are related to each other, the calculation of one matrix can derived others.

The first order partial derivatives of Z_ζ is

$$
\begin{aligned}
&g\left(\omega_m\right) = \tfrac{2\partial Z}{\partial E^*(\omega_m)} \\
&= \sum_{j=1}^{N} 2 \left\{ \begin{array}{l}
\left|E\left(\omega_j - \omega'_m\right) S_\zeta\left(\omega_j, \omega'_m\right)\right|^2 E\left(\omega'_m\right) \\
-\left[E\left(\omega_j - \omega'_m\right) S_\zeta\left(\omega_j, \omega'_m\right)\right]^* E'_{sig,\zeta}\left(\omega_j, \omega'_m\right) \\
+\left|E\left(\omega_j - \omega'_m\right) S_\zeta\left(\omega_j, \omega_j - \omega'_m\right)\right|^2 E\left(\omega'_m\right) \\
-\left[E\left(\omega_j - \omega'_m\right) S_\zeta\left(\omega_j, \omega_j - \omega'_m\right)\right]^* E'_{sig,\zeta}\left(\omega_j, \omega_j - \omega'_m\right)
\end{array} \right\}
\end{aligned}
$$

Which means

$$
\begin{aligned}
&\tfrac{\partial Z}{\partial \mathrm{Re}\{E(\omega_m)\}} \\
&= \sum_{j=1}^{N} 2\mathrm{Re} \left\{ \begin{array}{l}
\left|E\left(\omega_j - \omega'_m\right) S_\zeta\left(\omega_j, \omega'_m\right)\right|^2 E\left(\omega'_m\right) \\
-\left[E\left(\omega_j - \omega'_m\right) S_\zeta\left(\omega_j, \omega'_m\right)\right]^* E'_{sig,\zeta}\left(\omega_j, \omega'_m\right) \\
+\left|E\left(\omega_j - \omega'_m\right) S_\zeta\left(\omega_j, \omega_j - \omega'_m\right)\right|^2 E\left(\omega'_m\right) \\
-\left[E\left(\omega_j - \omega'_m\right) S_\zeta\left(\omega_j, \omega_j - \omega'_m\right)\right]^* E'_{sig,\zeta}\left(\omega_j, \omega_j - \omega'_m\right)
\end{array} \right\}
\end{aligned}
$$

$$
\begin{aligned}
&\tfrac{\partial Z}{\partial \mathrm{Im}\{E(\omega_m)\}} \\
&= \sum_{j=1}^{N} 2\mathrm{Im} \left\{ \begin{array}{l}
\left|E\left(\omega_j - \omega'_m\right) S_\zeta\left(\omega_j, \omega'_m\right)\right|^2 E\left(\omega'_m\right) \\
-\left[E\left(\omega_j - \omega'_m\right) S_\zeta\left(\omega_j, \omega'_m\right)\right]^* E'_{sig,\zeta}\left(\omega_j, \omega'_m\right) \\
+\left|E\left(\omega_j - \omega'_m\right) S_\zeta\left(\omega_j, \omega_j - \omega'_m\right)\right|^2 E\left(\omega'_m\right) \\
-\left[E\left(\omega_j - \omega'_m\right) S_\zeta\left(\omega_j, \omega_j - \omega'_m\right)\right]^* E'_{sig,\zeta}\left(\omega_j, \omega_j - \omega'_m\right)
\end{array} \right\}
\end{aligned}
$$

As for any complex number A,

$$\mathrm{Im}\left\{A\right\} \equiv \mathrm{Re}\left\{-iA\right\}$$

So $\frac{\partial Z}{\partial \mathrm{Im}\{E(\omega_m)\}}$ can be rewritten as

$$
\begin{aligned}
&\tfrac{\partial Z}{\partial \mathrm{Im}\{E(\omega_m)\}} \\
&= \sum_{j=1}^{N} 2\mathrm{Re} \left\{ \begin{array}{l}
-i\left|E\left(\omega_j - \omega'_m\right) S_\zeta\left(\omega_j, \omega'_m\right)\right|^2 E\left(\omega'_m\right) \\
+i\left[E\left(\omega_j - \omega'_m\right) S_\zeta\left(\omega_j, \omega'_m\right)\right]^* E'_{sig,\zeta}\left(\omega_j, \omega'_m\right) \\
-i\left|E\left(\omega_j - \omega'_m\right) S_\zeta\left(\omega_j, \omega_j - \omega'_m\right)\right|^2 E\left(\omega'_m\right) \\
+i\left[E\left(\omega_j - \omega'_m\right) S_\zeta\left(\omega_j, \omega_j - \omega'_m\right)\right]^* E'_{sig,\zeta}\left(\omega_j, \omega_j - \omega'_m\right)
\end{array} \right\}
\end{aligned}
$$

Starting from here, the Hessian for the objective function Z_ζ is

$$H_{mn}^{RR} = \left\{ \begin{array}{ll} n=m, & 2\mathrm{Re}\left\{ \begin{array}{l} \sum\limits_{j=1,j-m\neq n}^{N} \left\{ \begin{array}{l} |E(\omega_j-\omega'_n)|^2 \\ \times\left[|S_\zeta(\omega_j,\omega'_n)|^2+|S_\zeta(\omega_j,\omega_j-\omega'_n)|^2\right] \end{array} \right\} \\ +2S_\zeta(\omega_{2n},\omega'_n)^* \\ \times\left[E(\omega'_n)^2 S_\zeta(\omega_{2n},\omega'_n)-E'_{sig,\zeta}(\omega_{2n},\omega'_n)\right] \\ +4\left|E(\omega'_n)S_\zeta(\omega_{2n},\omega'_n)\right|^2 \end{array} \right\} \\ n\neq m, & 2\mathrm{Re}\left\{ \begin{array}{l} S_\zeta(\omega_{m+n},\omega'_m)^* \\ \times\left[E(\omega'_m)E(\omega_n)S_\zeta(\omega_{m+n},\omega'_m)-E'_{sig,\zeta}(\omega_{m+n},\omega'_m)\right] \\ +E(\omega_{m+n}-\omega'_m)^*\left|S_\zeta(\omega_{m+n},\omega'_m)\right|^2 E(\omega'_m) \\ +S_\zeta(\omega_{m+n},\omega'_n)^* \\ \times\left[E(\omega'_m)E(\omega_n)S_\zeta(\omega_{m+n},\omega'_n)-E'_{sig,\zeta}(\omega_{m+n},\omega'_n)\right] \\ +E(\omega'_n)^*\left|S_\zeta(\omega_{m+n},\omega'_n)\right|^2 E(\omega'_m) \end{array} \right\} \end{array} \right.$$

$$H_{mn}^{RI} = \left\{ \begin{array}{ll} n=m, & 2\mathrm{Re}\left\{ \begin{array}{l} i\times\sum\limits_{j=1,j-m\neq n}^{N} \left\{ \begin{array}{l} |E(\omega_j-\omega'_n)|^2 \\ \times\left[|S_\zeta(\omega_j,\omega'_n)|^2+|S_\zeta(\omega_j,\omega_j-\omega'_n)|^2\right] \end{array} \right\} \\ -i\times 2S_\zeta(\omega_{2n},\omega'_n)^* \\ \times\left[E(\omega'_n)^2 S_\zeta(\omega_{2n},\omega'_n)-E'_{sig,\zeta}(\omega_{2n},\omega'_n)\right] \\ +i\times 4\left|E(\omega'_n)S_\zeta(\omega_{2n},\omega'_n)\right|^2 \end{array} \right\} \\ n\neq m, & 2\mathrm{Re}\left\{ \begin{array}{l} -i\times S_\zeta(\omega_{m+n},\omega'_m)^* \\ \times\left[E(\omega'_m)E(\omega_n)S_\zeta(\omega_{m+n},\omega'_m)-E'_{sig,\zeta}(\omega_{m+n},\omega'_m)\right] \\ +i\times E(\omega_{m+n}-\omega'_m)^*\left|S_\zeta(\omega_{m+n},\omega'_m)\right|^2 E(\omega'_m) \\ -i\times S_\zeta(\omega_{m+n},\omega'_n)^* \\ \times\left[E(\omega'_m)E(\omega_n)S_\zeta(\omega_{m+n},\omega'_n)-E'_{sig,\zeta}(\omega_{m+n},\omega'_n)\right] \\ +i\times E(\omega'_n)^*\left|S_\zeta(\omega_{m+n},\omega'_n)\right|^2 E(\omega'_m) \end{array} \right\} \end{array} \right.$$

$$H_{mn}^{IR} = \begin{cases} n = m, \quad 2\mathrm{Re}\left\{ \begin{array}{l} -i \times \sum\limits_{j=1, j-m\neq n}^{N} \left\{ \begin{array}{l} \left|E\left(\omega_j - \omega_n'\right)\right|^2 \\ \times \left[\left|S_\zeta\left(\omega_j, \omega_n'\right)\right|^2 + \left|S_\zeta\left(\omega_j, \omega_j - \omega_n'\right)\right|^2\right] \end{array} \right\} \\ -i \times 2 S_\zeta\left(\omega_{2n}, \omega_n'\right)^* \\ \times \left[E\left(\omega_n'\right)^2 S_\zeta\left(\omega_{2n}, \omega_n'\right) - E'_{sig,\zeta}\left(\omega_{2n}, \omega_n'\right)\right] \\ -i \times 4 \left|E\left(\omega_n'\right) S_\zeta\left(\omega_{2n}, \omega_n'\right)\right|^2 \end{array} \right\} \\ n \neq m, \qquad 2\mathrm{Re}\left\{ \begin{array}{l} -i \times S_\zeta\left(\omega_{m+n}, \omega_m'\right)^* \\ \times \left[E\left(\omega_m'\right) E\left(\omega_n\right) S_\zeta\left(\omega_{m+n}, \omega_m'\right) - E'_{sig,\zeta}\left(\omega_{m+n}, \omega_m'\right)\right] \\ -i \times E\left(\omega_{m+n} - \omega_m'\right)^* \left|S_\zeta\left(\omega_{m+n}, \omega_m'\right)\right|^2 E\left(\omega_m'\right) \\ -i \times S_\zeta\left(\omega_{m+n}, \omega_n'\right)^* \\ \times \left[E\left(\omega_m'\right) E\left(\omega_n\right) S_\zeta\left(\omega_{m+n}, \omega_n'\right) - E'_{sig,\zeta}\left(\omega_{m+n}, \omega_n'\right)\right] \\ -i \times E\left(\omega_n'\right)^* \left|S_\zeta\left(\omega_{m+n}, \omega_n'\right)\right|^2 E\left(\omega_m'\right) \end{array} \right\} \end{cases}$$

$$H_{mn}^{II} = \begin{cases} n = m, \quad 2\mathrm{Re}\left\{ \begin{array}{l} \sum\limits_{j=1, j-m\neq n}^{N} \left\{ \begin{array}{l} \left|E\left(\omega_j - \omega_n'\right)\right|^2 \\ \times \left[\left|S_\zeta\left(\omega_j, \omega_n'\right)\right|^2 + \left|S_\zeta\left(\omega_j, \omega_j - \omega_n'\right)\right|^2\right] \end{array} \right\} \\ -2 S_\zeta\left(\omega_{2n}, \omega_n'\right)^* \\ \times \left[E\left(\omega_n'\right)^2 S_\zeta\left(\omega_{2n}, \omega_n'\right) - E'_{sig,\zeta}\left(\omega_{2n}, \omega_n'\right)\right] \\ +4 \left|E\left(\omega_n'\right) S_\zeta\left(\omega_{2n}, \omega_n'\right)\right|^2 \end{array} \right\} \\ n \neq m, \quad 2\mathrm{Re}\left\{ \begin{array}{l} -S_\zeta\left(\omega_{m+n}, \omega_m'\right)^* \\ \times \left[E\left(\omega_m'\right) E\left(\omega_n\right) S_\zeta\left(\omega_{m+n}, \omega_m'\right) - E'_{sig,\zeta}\left(\omega_{m+n}, \omega_m'\right)\right] \\ +E\left(\omega_{m+n} - \omega_m'\right)^* \left|S_\zeta\left(\omega_{m+n}, \omega_m'\right)\right|^2 E\left(\omega_m'\right) \\ -S_\zeta\left(\omega_{m+n}, \omega_n'\right)^* \\ \times \left[E\left(\omega_m'\right) E\left(\omega_n\right) S_\zeta\left(\omega_{m+n}, \omega_n'\right) - E'_{sig,\zeta}\left(\omega_{m+n}, \omega_n'\right)\right] \\ +E\left(\omega_n'\right)^* \left|S_\zeta\left(\omega_{m+n}, \omega_n'\right)\right|^2 E\left(\omega_m'\right) \end{array} \right\} \end{cases}$$

To simplify the expression we define,

$$T_{mn} = \begin{cases} n = m, & \left\{ \begin{array}{l} \sum\limits_{j=1, j-m\neq n}^{N} \left|E\left(\omega_j - \omega_n'\right)\right|^2 \left[\left|S_\zeta\left(\omega_j, \omega_n'\right)\right|^2 + \left|S_\zeta\left(\omega_j, \omega_j - \omega_n'\right)\right|^2\right] \\ +4 \left|E\left(\omega_n'\right) S_\zeta\left(\omega_{2n}, \omega_n'\right)\right|^2 \end{array} \right\} \\ n \neq m, & E\left(\omega_n'\right)^* E\left(\omega_m'\right) \left[\left|S_\zeta\left(\omega_{m+n}, \omega_m'\right)\right|^2 + \left|S_\zeta\left(\omega_{m+n}, \omega_n'\right)\right|^2\right] \end{cases}$$

$$F_{mn} = \begin{cases} n = m, & 2S_\zeta\left(\omega_j, \omega'_n\right)^* \left[E\left(\omega'_n\right)^2 S_\zeta\left(\omega_{2n}, \omega'_n\right) - E'_{sig,\zeta}\left(\omega_{2n}, \omega'_n\right)\right] \\ n \neq m, & \left\{ \begin{array}{l} S_\zeta\left(\omega_{m+n}, \omega'_m\right)^* \\ \times \left[E\left(\omega'_m\right) E\left(\omega_n\right) S_\zeta\left(\omega_{m+n}, \omega'_m\right) - E'_{sig,\zeta}\left(\omega_{m+n}, \omega'_m\right)\right] \\ + S_\zeta\left(\omega_{m+n}, \omega'_n\right)^* \\ \times \left[E\left(\omega'_m\right) E\left(\omega_n\right) S_\zeta\left(\omega_{m+n}, \omega'_n\right) - E'_{sig,\zeta}\left(\omega_{m+n}, \omega'_n\right)\right] \end{array} \right\} \end{cases}$$

Then

$$\begin{aligned} H^{RR} &= 2\mathrm{Re}\left\{F + T\right\} \\ H^{RI} &= 2\mathrm{Re}\left\{-iF + iT\right\} \\ H^{IR} &= 2\mathrm{Re}\left\{-iF - iT\right\} \\ H^{II} &= 2\mathrm{Re}\left\{-F + T\right\} \end{aligned}$$

Now we can calculate the 2N by 2N Hessian of Z_ζ, only using N by N computing time.

REFERENCES

[1] Acton, F., *Numerical Methods That Work*. Washington: Mathematical Association of America, 1990.

[2] Akturk, S.and Kimmel, M., O'Shea, P., and Trebino, R., "Measuring pulse-front tilt in ultrashort pulses using grenouille," *Optics Express*, vol. 11, no. 5, pp. 491–501, 2003.

[3] Akturk, S.and Kimmel, M., O'Shea, P., and Trebino, R., "Measuring spatial chirp in ultrashort pulses using single-shot frequency-resolved optical gating," *Optics Express*, vol. 11, no. 1, pp. 68–78, 2003.

[4] Altes, R., "Detection, estimation, and classification with spectrograms," *J. Acoust. Soc. Amer.*, vol. 67, no. 4, pp. 1232–1246, 1980.

[5] Arakelian, S., Gyuzalian, R., and Sogomonian, S., "Comments on the picosecond pulse width measurment by the single-shot second harmonic beam technique," *Optics Communications*, vol. 44, no. 1, pp. 67–72, 1982.

[6] Baltuska, A., Pugzlys, A., Pshenichnikov, M., and Wiersma, D., "Rapid amplitude-phase reconstruction of femtosecond pulses from intensity autocorrelation and spectrum," in *Conference on Laser and Eletro-Optics (CLEO)*, (Baltimore, MD), 1999.

[7] Baltuska, A., Wei, Z., Pshenichnikov, M., Wiersma, D., and Szipocs, R., "All-solid-state cavity-dumped sub-5-fs laser," *Apply Physics B*, vol. 65, pp. 175–188, 1997.

[8] Bard, Y., *Nonlinear Parameter Estimation.* New York, San Francisco, London: Academic Press, 1974.

[9] Bourne, O. and Alcock, A., "Ultraviolet and visible single-shot autocorrelator based on multiphoton ionization," *Review of Scientific Instruments*, vol. 57, no. 12, pp. 2979–2982, 1986.

[10] Brent, R., *Algorithms for Minimization without Derivatives.* Englewood Cliffs, NJ: Prentice Hall, 1973.

[11] Brun, A., "Single-shot characterization of ultrashort light pulses.," *J. Phys. D.*, vol. 24, pp. 1225–1233, 1991.

[12] Buvat, I., "A non-paramteric bootstrap approach for analysing the statistical properties of spect and pet images," *PHYSICS IN MEDICINE AND BIOLOGY*, vol. 47, no. 10, pp. 1761–1775, 2002.

[13] Chung, J.-H. and Weiner, A. M., "On the determination of the phase of a fourier integral, ii," *Ambiguity of ultrashort pulse shapes retrieved from the intensty autocorrelation and power spectrum,*, vol. 7, no. 4, pp. 656–666, 2001.

[14] Clement, T. S., Taylor, A. J., and Kane, D. J., "Single-shot measurement of the amplitude and phase of ultrashort laser pulses in the violet," *Optics Letters*, vol. 20, no. 1, pp. 70–72, 1995.

[15] Cohen, L., "Time-frequency distributions –a review," *Proceeding of the IEEE*, vol. 77, no. 7, pp. 941–981, 1989.

[16] Cohen, L., *Time-Frequency Analysis.* Englewood Cliffs: NJ:Prentice-Hall, 1995.

[17] Davison, A. and Hinkley, D., *Bootstrap Methods and their Application.* Cambridge: Cambridge University Press, 1997.

[18] Dudley, J. M., Gu, X., Xu, L., Kimmel, M., Zeek, E., O'Shea, P., Trebino, R., Coen, S., and Windeler, R. S., "Cross-correlation frequency resolved optical gating analysis of broadband continuum generation in photonic crystal fiber: simulations and experiments," *Optics Express*, vol. 10, no. 21, pp. 1215–1221, 2002.

[19] Efron, B. and Tibshirani, R. J., *An Introduction to the Bootstrap.* Boca Raton, London, New York, Washington D.C.: CHAPMAN & HALL/CRC, 1993.

[20] Fienup, J., "Reconstruction of an object from the modulus of its fourier transform.," *Optics Letters*, vol. 3, no. 1, pp. 27–29, 1978.

[21] Fienup, J., "Phase retrieval algorithms: A comparison.," *Applied Optics*, vol. 21, no. 15, pp. 2758–2769, 1982.

[22] Fienup, J., "Reconstruction of an complex-valued object from the modulus of its fourier transform using a support constraint.," *JOURNAL OF THE OPTICAL SOCIETY OF AMERICA A-OPTICS IMAGE SCIENCE AND VISION*, vol. 4, no. 1, pp. 118–123, 1987.

[23] Fienup, J. and Kowalczyk, A., "Phase retrieval for an complex-valued object by using a low-resolutions image.," *JOURNAL OF THE OPTICAL SOCIETY OF AMERICA A-OPTICS IMAGE SCIENCE AND VISION*, vol. 7, no. 3, pp. 450–458, 1990.

[24] Fienup, J. and Wackerman, C., "Phase-retrieval stagnation problems and solutions.," *JOURNAL OF THE OPTICAL SOCIETY OF AMERICA A-OPTICS IMAGE SCIENCE AND VISION*, vol. 3, pp. 1897–1907, 1986.

[25] Fourkas, J., "Spatially-encoded, single-shot ultrafast spectroscopies.," *J. Opt. Soc. of Amer. B*, vol. 12, no. 1, pp. 155–165, 1995.

[26] Freedman, D. and Peters, S., "Bootstrapping a regression equation: some empirical results.," *Journal of the American Statistical Association*, vol. 79, pp. 97–106, 1984a.

[27] Freedman, D. and Peters, S., "Bootstrapping a econometric model: some empirical results.," *Journal of Business & Economic Statistics*, vol. 2, pp. 150–158, 1984b.

[28] Gross, S., "Median estimation in sample surveys.," in *Proceeding of the section on Surevey Research Methods*, (Alexandria, Virginia), pp. 181–184, 1980.

[29] Gu, X., Xu, L., Kimmel, M., Zeek, E., O'Shea, P., Shreenath, A. P., Trebino, R., and Windeler, R. S., "Frequency-resolved optical gating and single-shot spectral measurements reveal fine structure in microstructure-fiber continuum," *Optics Letters*, vol. 27, no. 13, pp. 1174–1176, 2002.

[30] Hall, P. and Owen, A., "Empirical likelihood confidence bands in density estimation.," *Journal of Computational and Graphical Statistics*, vol. 2, pp. 273–289, 1993.

[31] Heath, M. T., *Scientific Computing, An Introductory Survey.* New York: McGraw-Hill, 2002.

[32] Jansky, J. and Corradi, G., "Full intensity profile analysis of ultrashort laser pulses using four-wave mixing or third harmonic generation.," *Optics Communications*, vol. 60, no. 4, pp. 251–256, 1986.

[33] Kabelka, V. and Masalov, A., "Angularly resolved autocorrelation for single shot time-frequency imaging of ultrashort light pulse.," *Optics Communications*, vol. 121, no. 4-6, pp. 141–148, 1995.

[34] Kane, D. J., Omenetto, F. G., and Taylor, A. J., "Convergence test for inversion of frequency-resolved optical gating spectrograms," *Optics Letters*, vol. 25, no. 16, pp. 1216–1218, 2000.

[35] Kane, D., "Simultanous measurement of two ultrashort laser pulses from a single spectrogram in a single shot.," *Optics Letters*, vol. 18, no. 10, pp. 823–825, 1993.

[36] Kane, D. and Trebino, R., "Single-shot measurement of the intensity and phase of an arbitrary ultrashort pulse by using frequency-resolved optical gating.," *Optics Letters*, vol. 18, no. 10, pp. 823–825, 1993.

[37] Keusters, D., Tan, H., O'Shea, P., Zeek, E., Trebino, R., and Warren, W. S., "Relative-phase ambiguities in measurements of ultrashort pulses with well-separated multiple frequency components," *JOURNAL OF THE OPTICAL SOCIETY OF AMERICA B-OPTICAL PHYSICS*, vol. 20, no. 10, pp. 2226–2237, 2003.

[38] Kintzer, E. and Rempel, C., "Near-surface second-harmonic generation for autocorrelation measurements in the uv," *Applied Physics B*, vol. 42, pp. 91–95, 1987.

[39] K.Naganuma, K.Mogi, J., "General method for ultrashort light pulse chirp measurement," *IEEE J. Quantum Electron*, vol. 25, pp. 1225–1233, 1989.

[40] Le Blanc, S., Szabo, G., and Sauerbrey, R., "Femtosecond single-shot phase-sensitive autocorrelator for the ultraviolet.," *Optics Letters*, vol. 16, no. 19, pp. 1508–1510, 1991.

[41] Mehendale, M., "Method for single-shot measurement of the carrier envelope phase of a few-cycle laser pulse.," *Optics Letters*, vol. 25, no. 22, pp. 1672–1674, 2000.

[42] Millane, R. P., "Phase retrieval in crystallography and optics," *JOURNAL OF THE OPTICAL SOCIETY OF AMERICA A-OPTICS IMAGE SCIENCE AND VISION*, vol. 7, no. 3, pp. 394–411, 1990.

[43] Millane, R., "Phase retrieval in crystallgraphy and optics," *JOURNAL OF THE OPTICAL SOCIETY OF AMERICA A-OPTICS IMAGE SCIENCE AND VISION*, vol. 7, no. 3, pp. 394–411, 1990.

[44] Naganuma, K., Mogi, K., and Yamada, J., "Temporal decorrelation of short laser pulses," *JOURNAL OF THE OPTICAL SOCIETY OF AMERICA B-OPTICAL PHYSICS*, vol. 15, pp. 216–222, 1998.

[45] Nawab, S., Quatieri, T., and Lim, J., "Signal reconstruction from short-time fourier transform magnitude," *IEEE Transaction on Acoustics, Speech, and Signal Processing*, vol. ASSP-31, no. 4, pp. 986–988, 1983.

[46] Nelder, J. and Mead, R. *Computer Journal*, vol. 7, pp. 308–313, 1965.

[47] O'Shea, P., Kimmel, M., Gu, X., and Trebino, R., "Highly simplified ultrashort pulse measurement," *Optics Letters*, vol. 26, pp. 932–934, 2001.

[48] Peri, D., "Optical implementation of a phase retrieval algorithm.," *Applied Optics*, vol. 26, no. 9, pp. 1782–1785, 1987.

[49] Press, W. H., Teukolsky, S. A., and Vettering, W. T.and Flannery, B. P., *Numerical Recipes in C: The Art of Scientific Computing*. Cambridge: Cambridge University Press, 1995.

[50] Rayner, D., Hackett, P., and Willis, C., "Short pulse-width measurment by multiphoton ionization autocorrelation," *Review of Scientific Instruments*, vol. 53, no. 4, pp. 537–538, 1982.

[51] Stark, H., *Image Recovery: Theory and Application*. Orlando: Academic Press, 1987.

[52] Szatmari, S., Schafer, F., and Jethwa, J., "A single-shot autocorrelation for the ultraviolet with a variable time window," *Review of Scientific Instruments*, vol. 61, no. 3, pp. 998–1003, 1990.

[53] Trenbino, R., *Frequency-Resolved Optical Gating: The Measurement of Ultrashort Laser Pulses*. Boston, Dordrecht, London: KLUWER ACADAMIC, 2002.

[54] Walther, A., "The question of phase retrieval in optics," *Optics Acta*, vol. 10, pp. 41–49, 1963.

[55] Wang, Z., Zeek, E., Trebino, R., and Kvam, P., "Beyond error bars: Understanding uncertainty in ultrashort-pulse frequency-resolved-optical-gating measurements in the presence of ambiguity.," *Optics Letters*, vol. 11, no. 26, pp. 3518–3527, 2003.

[56] Wang, Z., Zeek, E., Trebino, R., and Kvam, P., "Determining error bars in measurements of ultrashort laser pulses.," *JOSA B*, vol. 20, no. 11, pp. 2400–2405, 2003.

[57] Wyatt, R. and Marinero, E., "Versatile single-shot background-free pulse duration measurement technique for pulses of subnanosecond to picosecond duration," *Applied Physics*, vol. 25, pp. 297–301, 1981.

[58] Zhang, J., Shreenath, A., and M, K., "Measurement of the intensity and phase of attojoule femtosecond light pulses using optical-parametric-amplification cross-correlation frequency-resolved optical gating," *Optics Express*, vol. 11, no. 6, pp. 601–609, 2003.

VITA

Ziyang Wang was born in SiChuan, China. He received the degrees of Bachelor of Science in Physics and Master of Science in Optics from Tsinghua University, Beijing, China, in 1997 and 2000 respectively. Since then, he has been working in the School of Physics, Georgia Tech, where he conducts graduate research in the Ultrafast Optics Lab under the guidance of Professor Rick Trebino.